IMPROVEMENT OF GEOPHYSICAL MODEL FUNCTIONS FOR RADAR-BASED OCEAN SURFACE CURRENTS MEASUREMENTS

Shadi Aslebagh

A dissertation

submitted in partial fulfillment of the

requirements for the degree of

Doctor of Philosophy

University of Washington

2018

Reading Committee:

John D. Sahr, Chair

Yasuo Kuga

Lih Lin

Program Authorized to Offer Degree:

Electrical Engineering

University of Washington

Abstract

IMPROVEMENT OF GEOPHYSICAL MODEL FUNCTIONS FOR RADAR-BASED OCEAN SURFACE CURRENTS MEASUREMENTS

Shadi Aslebagh

Chair of the Supervisory Committee:
John D. Sahr
Department of Electrical and Computer Engineering

My objective in this research work is to improve the quality of ocean surface current measurements using synthetic aperture radars. I will do this by including an improved, physics-based model in the algorithm that inverts the radar data to estimate ocean currents. Although the ocean winds geophysical model functions used by scatterometers are mature, there is significant deficiency in knowledge of the ocean surface current geophysical model function; my research addresses this deficiency.

In the first chapter of this thesis, I discuss the importance of ocean surface currents, and various techniques to measure them. Following that introduction, in chapter 2, I introduce the microwave radar system, which I used to collect microwave data for this research work. The corresponding flight experiments for microwave data collection are also described in this chapter.

In chapter 3, the surface current estimation method is discussed and few samples of retrieved surface current components are presented. Chapter 4 introduces a physics-based Doppler model, M4S, which is used to improve the surface current geophysical model function. First, I run the model for different cases and compare the model's outputs with radar measurements to evaluate the existing model. In chapter 5, in order to improve surface current geophysical model function, I incorporate model's output to the geophysical retrieval algorithm and present the output of the retrieval algorithm. Eventually, in chapter 6, I will implement improvement to the model, which ultimately results in improvement of surface current geophysical model functions. Chapter 6 includes the results, discussions and suggestions for future work.

TABLE OF CONTENTS

LIST OF FIGURES

LIST OF TABLES

ACKNOWLEDGEMENTS

First, I would like to truly thank Dr. John D. Sahr for giving me the great opportunity to purse my PhD degree with him. It has been a great pleasure for me to work under his supervision and I will be grateful to him forever. I would also like to thank my former advisor Dr. Gordon Farquharson for his great support while he was at University of Washington during the first four years of my PhD.

My appreciation goes to my committee members, Dr. Lih Lin, Dr. Yasuo Kuga and Dr. Dale Winebrenner for their valuable comments and guidance.

I had the great opportunity to work with the team members at Air-Sea Interaction & Remote Sensing (AIRS) department at Applied Physics Laboratory (APL), UW and I would like to thank each and everyone of them. I would like to name Dr. Andrew T. Jessup, Dr. Chris Chickadel, Dr. Melissa Moulton and Dr. Jim Thompson at AIRS for their support throughout my research work and field experiments during my PhD. They were great supporters and openly provided their best help at my hard times, for which I am and will remain thankful.

I appreciate all the support form Dr. Roland Romeiser. While he provided me with the model he developed and let me use his model for my research, he was always responding my questions and helping me out making the best of his model.

I would like to thank my family. I am so much blessed to have wonderful parents who have given me the love that has been inspiring me every day of my life. I want to thank my lovely sisters, who have been by my side throughout my life. I am also thankful to true friends of mine who were by my side whenever I needed them. Last but not the least; I thank my husband for the unlimited love and great support he has brought into my life.

Chapter 1. INTRODUCTION

Ocean surface currents play a significant role in global transport of heat and nutrients. Within the Arctic Ocean, the near-surface current determines the distribution and pathways of fresh water. In addition, knowledge of ocean surface currents helps us track marine debris and pollutants, in marine search and rescue operations. Furthermore, because of ocean and atmosphere coupling, the ability to measure ocean surface currents improves our understanding of weather and climate.

Ocean surface currents are important for life on earth. They transport heat, surface momentum and gas fluxes, and therefore are critical in modulating weather and climate. They also affect ocean productivity and marine biological communities, which in turn affects marine life and fishing.

Over the past few decades, dominant surface current anomalies have generally resulted in sea surface temperature anomalies. As depicted in Figure 1.1 surface current (SC) anomalies tend to lead sea surface temperatures (SST) by 2.5-3 months [1]. Figure 1.1 also shows that a rapid surface current anomaly reversal has coincided with the peak sea surface temperature of warm events [1]. The green dotted line in Figure 1.1 shows one good example of these anomalies, which happened in late 1997.

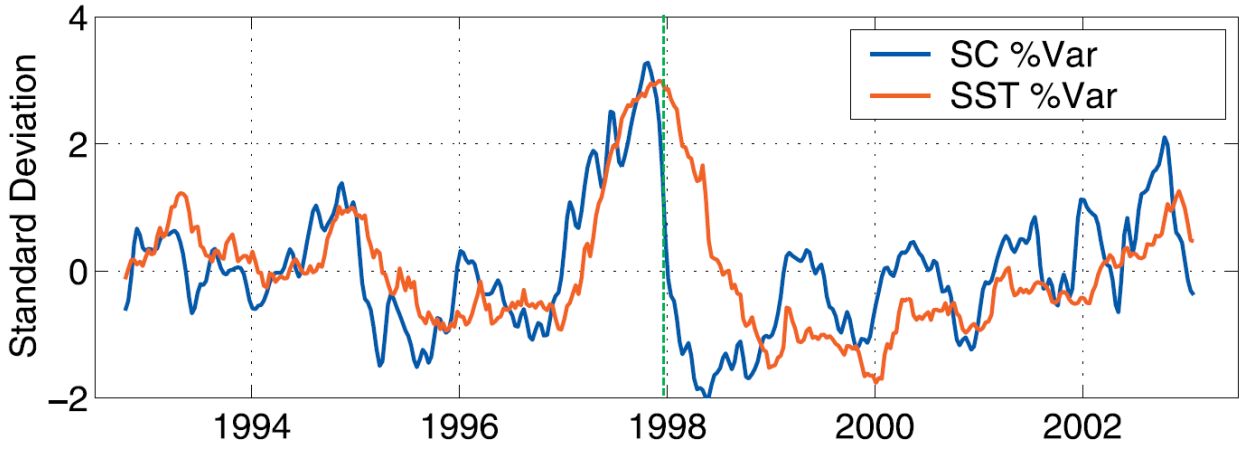

Figure 1.1. Surface current and sea surface temperature anomalies [1]. In this figure, the x-axis is time in years and y-axis represents relative standard deviation of surface current and sea surface temperature.

For the reasons outlined above, it is crucial to make accurate measurements of ocean surface currents. Although large-scale surface current measurements have been available for decades with radar altimeters, there is no practical sensor technology that has yet been developed to make small-scale surface current measurement available over a wide area. As the ability to model weather and climate at higher resolutions becomes better through advances in computational technology, the lack of highly spatially resolved measurements limits the ability to model these processes accurately.

Therefore, the science community needs to constantly invest in improving observational capability. Altimeters and drifters do a good job at measuring large-scale (> 10 km) ocean surface currents by measuring sea level and wind stress fields. The large-scale ocean surface currents transport warm water from the equator towards the poles and cold water from the poles back to the tropics [2]. Among other things, the oceans have about 500 times the heat capacity of the atmosphere.

There are two methods for estimating ocean surface currents: *in-situ* measurements and remote sensing based measurements. Each method has its own strengths and weaknesses. It is very challenging to deploy *in-situ* sensors in the oceans. *In-situ* sensors require constant maintenance for recovery and redeployment for continuous operation. On the other hand, remote sensing methods give us more freedom to measure ocean surface currents in a wide variety of environmental conditions. It also makes it possible to measure ocean surface currents over larger areas compared with *in-situ* measurements.

In order to model weather more accurately, it is crucial to measure small-scale surface currents at resolutions as fine as 1 km [3]. Numerical weather models are now able to model atmospheric-ocean process at these resolutions, but require instruments with capability of measuring these small-scale ocean surface currents. For these reasons, remote sensing techniques capable of measuring high-resolution (small-scale) ocean surface currents have become critically important.

Different radar techniques to measure small-scale ocean currents have been tried, with the most popular being Along Track Interferometry (ATI) and direct Doppler analysis measurements [4]. Both techniques make a Doppler measurement, and rely on a Geophysical Model Function (GMF) to estimate the ocean surface current from the measurement. A GMF is a function, which relates the remotely observed variable (backscattered microwaves from a water surface with waves in this case) to the variable of interest (ocean surface current in this case). However, there is a significant deficiency in ocean surface current GMFs.

My main objective in this research is to improve radar geophysical model functions that map ocean Doppler radar measurements into surface currents. In order to do that, I used a surface scattering model developed by Dr. Roland Romeiser [5] [6]. I ran the model for different cases

corresponding to the conditions in which radar data was collected during field experiments. Then I used the outputs of the model to improve the surface current GMF. I also implemented a modification to the model by inserting actual local ocean wave measurements into the model and showed how the surface current retrieval improves after applying this modification.

Chapter 2. RADAR INSTRUMENT AND FIELD EXPERIMENTS

In this chapter, I introduce the Along Track Interferometry Synthetic Aperture Radar (ATI-SAR) system. In SAR systems, very high spatial resolution is achieved by the radar antenna flying on a platform and synthesizing large antenna aperture. In other words, the azimuth resolution improves as antenna gets smaller and less directive [7].

The interferometry term comes from the idea of having two receiver antennas in order to capture the surface at slightly different time and forming the interferometric phase between the two measurements, which permits estimation of the target radial (Doppler) velocity. In along-track interferometry systems, antennas are placed along the platform flight direction.

The data I present in this thesis is collected by an ATI-SAR system during several flight experiments. This system was operated by the Applied Physics Lab (APL) at University of Washington, and has been used in several projects to collect microwave data from land and water surfaces.

2.1 INTRODUCTION TO ALONG-TRACK INTERFEROMETRY SYNTHETIC APERTURE RADAR

The interferometric SAR technique is the combination of conventional SAR technique and interferometry. Along-Track Interferometry SAR technique is based on the acquisition of two SAR images taken under identical geometries separated by a short time interval. When the surface is in motion, then a Doppler shift is observed according to the velocity of moving surface. The ATI technique has proven valuable to sense the earth-surface motion such as ocean surface current, where the speed accuracies are on the order of a few centimeters per second at high spatial resolution [8].

ATI-SAR comprises two receiving antennas that are physically separated by a baseline distance *B* along the aircraft flight path direction. Figure 2.1 shows the schematic geometry of receiving antennas in an ATI-SAR. Since these two antennas capture the backscatter field from the same spot on the surface, there is a short time lag τ between these two measurements. The interferometric phase can be extracted from combining these two measurements by multiplying one by the complex conjugate of the other. The measurements have complex value because they represent both magnitude and phase of the back scattered filed.

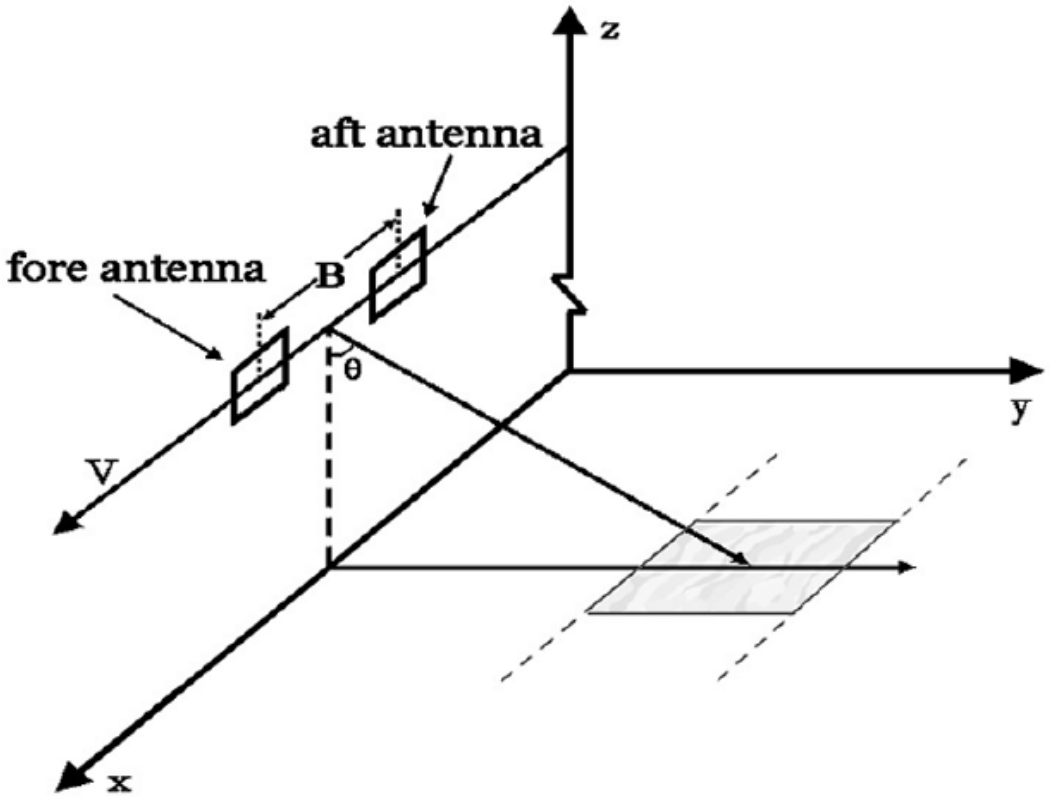

Figure 2.1. Schematic geometry of receiving antennas with a baseline distance B in an ATI-SAR [9].

In the ATI technique, the two receiving antennas measure the back scattered field from the same spot on the surface. The receiving antennas capture the surface at slightly different times

with separation τ, which is proportional to the antenna displacement B as is shown in equation (2.1). V_{AC} is the ATI-SAR platform (aircraft) velocity. Depending upon the ATI-SAR system configuration, τ can have different values. A typical value for τ in an airborne ATI-SAR system is few milliseconds.

$$\tau = \frac{B}{V_{AC}} \tag{2.1}$$

The phase difference between these two measurements is known as interferometric phase, which is proportional to the radial velocity of the scatterer. Equation (2.2) expresses the relation between the interferometric phase ($\Delta\varphi$) measured by ATI-SAR and the radial velocity of the scatterer (v_r), where λ_i is the wavelength of the radar incident wave.

$$\Delta\varphi = \omega_D \tau = \left(\frac{2\pi}{\lambda_i}\ v_r\right)\left(\frac{B}{V_{AC}}\right) \tag{2.2}$$

In a C-band ATI-SAR system with a radar incident wavelength around 6 cm, a baseline of 40 cm and a platform velocity around 50 m/s, the maximum variation range for $\Delta\varphi$ is $\pm\pi$ radians, corresponding to a ±4 m/s range for the radial velocity (v_r), which is a reasonable range for ocean surface currents velocity. These numbers are similar to the specifications of the ATI-SAR system used in this research. The APL-UW ATI-SAR system is introduced in next section.

2.2 APL-UW C-BAND ATI-SAR INSTRUMENT

The APL-UW radar is a dual-beam Frequency Modulated Continuous Wave (FMCW) radar and provides both forward-squinted and aft-squinted looks with the same squint angle forward and backward. This capability permits the radar able to measure the full surface current vector in a

single flight pass. The two look directions provide two radial components of the velocity from which the velocity vector can be determined [10]. Figure 2.2 shows a conceptual diagram of a dual-beam ATI-SAR with the squint angle of θ_s, where u_r^+ and u_r^- are the forward-looking and aft-looking radial velocity of the scatterer, respectively and v represent the velocity vector of the scatterer.

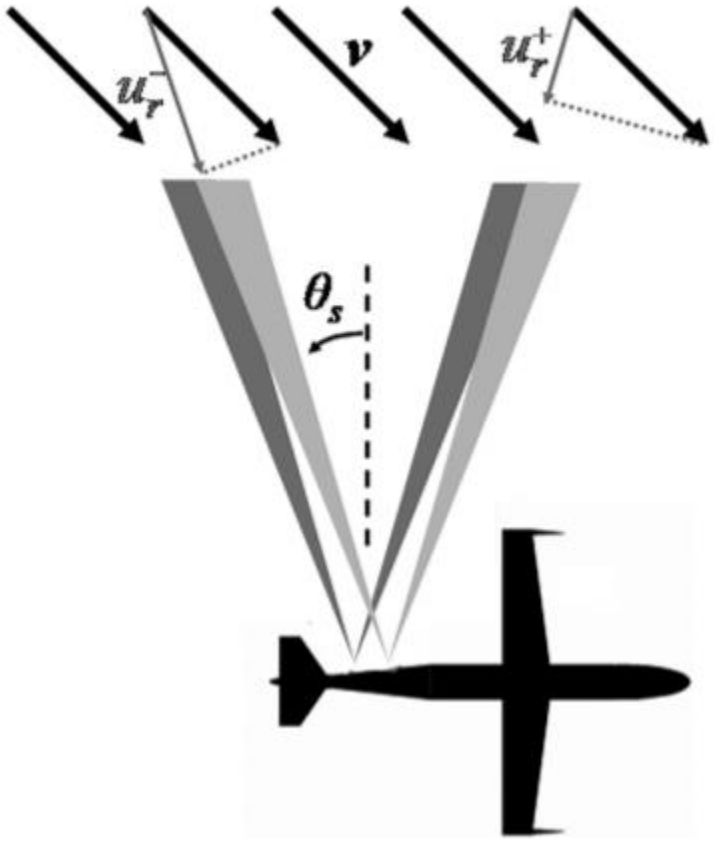

Figure 2.2. Conceptual diagram of the dual-beam ATI-SAR [10]. Two radar beams (forward- and aft-looking) provide different radial Doppler measurements from which the vector surface velocity can be deduced.

APL-UW in collaboration with Artemis Inc. has developed a miniaturized dual-receiver ATI-SAR operates at C-band frequency [11]. Table 2.1 shows the technical specifications of this

system. One can notice that there is a slight difference between the specifications of forward-squinted and aft-squinted antennas. These antennas meant to design identical. However, considering the fact that their operating frequencies are slightly different, there are small differences between some of their specifications such as antenna gain and 3-dB beam width.

Table 2.1. Dual-beam ATI-SAR operating parameters [12].

	Foreward-squinted SAR	**Aft-squinted SAR**	
Signals and timing			
Modulation type	LFM-CW	LFM-CW	
Frequency range	5448.76 – 5528.76	5328.76 – 5408.76	MHz
Center frequency	5488.76	5368.76	MHz
Bandwidth	80	80	MHz
Transmitted power	1	1	W
Pulse repetition frequency	749.969	749.969	Hz
Antennas			
Polarization	VV	VV	
Antenna gain	18.9	18.7	dBi
3 dB beam width (E-plane)	28	30	deg.
10 dB beam width (E-plane)	51	55	deg.
3 dB beam width (H-plane)	7.2	7.3	deg.
10 dB beam width (H-plane)	12.6	12.7	deg.
Nominal squint angle	+30	−30	deg.
Nominal incidence angle	60	60	deg.
Inertial Navigation System			
Horizontal velocity accuracy	0.02		$m\ s^{-1}$ rms
Vertical velocity accuracy	0.01		$m\ s^{-1}$ rms
Pitch accuracy	0.013		deg. rms
Roll accuracy	0.010		deg. rms
Yaw accuracy	0.024		deg. rms
Resolution and Coverage			
Operating altitude	762	762	m
Slant range resolution	1.875	1.875	m
Maximum slant range	3.8	3.8	km
Maximum cross-track range	3.1	3.1	km

The radar antennas have vertical polarization (VV) while their incidence angle varies between 40 to 75 degrees. The transmitted signal has a bandwidth of 80 MHz for each radar, so the slant range resolution is 1.875 m. Further details about this system can be found in [13][14]. These SAR data are processed with a time-domain back-projection algorithm similar to the one described in [15].

The previous generation of SAR systems had large physical size in order to provide high transmitting power. Therefore, they had to be installed on large aircraft or spacecraft, which resulted in costly systems to operate due to their large physical sizes. However, the APL ATI-SAR system uses a low power transmitter that results in significant reduction in physical size, and it can be installed on a small aircraft. This causes a significant reduction in operational cost in order to fly over the nearshore environment to collect data. The low power transmitter requires it to fly nearer the target to overcome path loss.

The APL ATI-SAR was operated from a Cessna 172/182 aircraft flying at an altitude of ~900 m. Figure 2.3 shows the platform and the antennas attached to the belly of the aircraft on the left panel. The right panel also shows the electronics of the radar units, which sit inside the aircraft.

Figure 2.3. APL ATI-SAR and its platform. Pictures Courtesy of Gordon Farquharson.

The APL ATI-SAR system provides dual-beam capability. The dual-beam ATI-SAR includes both forward-squinted radar and aft-squinted radars. The dual-beam property of the ATI-SAR enables it to measure both x- and y-components of the scatterer velocity from forward-squinted and aft-squinted radial velocities in a single flight pass of the radar platform over the moving scatterer.

Each radar has three vertically-polarized broadside-beam flat-panel antennas: one as transmitter antenna and the other two as receiving antennas. The forward-squinted antennas and the aft-squinted antennas are installed on the starboard side of the aircraft and port side of the aircraft respectively. In the forward-squinted antennas set, the one closest to the aircraft nose is the transmitter antenna and the other two are the receiver antennas. In aft-squinted antennas' set the closest antenna to the aircraft tail is the transmitter antenna and the other two are the receiver one. This configuration minimizes the interference from the transmitter antenna to the receiver antennas. As presented in Figure 2.4 starboard and port side of the aircraft refer to the right and left side of the aircraft respectively. The antennas are not covered by a radome to minimize cost, weight and installation complexity.

Figure 2.4. Forward- and aft-squinted antennas on the starboard and port side of the aircraft [16].

There is also an inertial navigation system (INS) to measure aircraft position, velocity and altitude. The INS also records roll, pitch and yaw of the flying aircraft, which will be used for aircraft motion compensation in the SAR processing algorithm.

2.2.1 *Interferometric phase*

For the data used in this research, ATI-SAR data sets are processed in matrix format and each cell consists of a complex (real and imaginary part) value. Each complex value is a backscattered field from one specific pixel on the earth surface. Since the location of the scatterer inside each pixel is random, so the distance from the scatterer point to the SAR antenna is also random. Thus, the phase of these single look complex numbers is also random and looks noisy as presented in Figure 2.5.

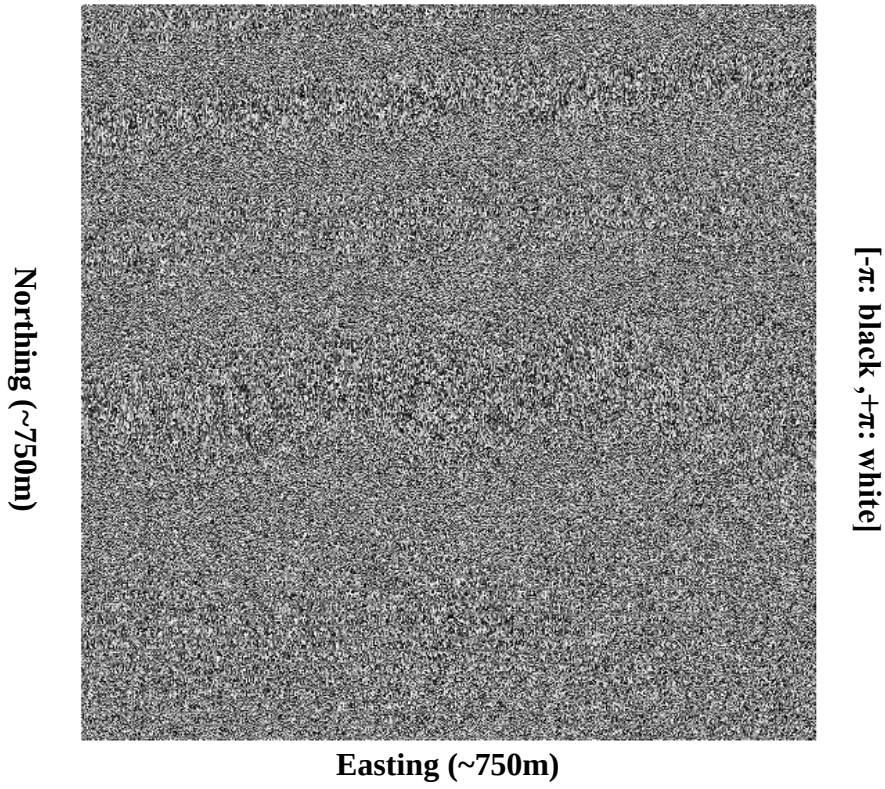

Figure 2.5. Noisy phase of the backscattered field from a scattering point on the surface, measured by one receiving antenna. Each pixel represents a region approximately 75 by 75 cm.

To reduce the level of noise, the interferometric phase should be considered instead. Since the second measurement by the second receiving antenna is performed at a slightly different time (τ in equation (2.1)), then the equivalent scatterer point moves slightly and the distance between the antenna and scatterer point differs by a small value, which causes different phases. The difference between these two phases is the interferometric phase and is shown in Figure 2.6 for the same case as presented in Figure 2.5.

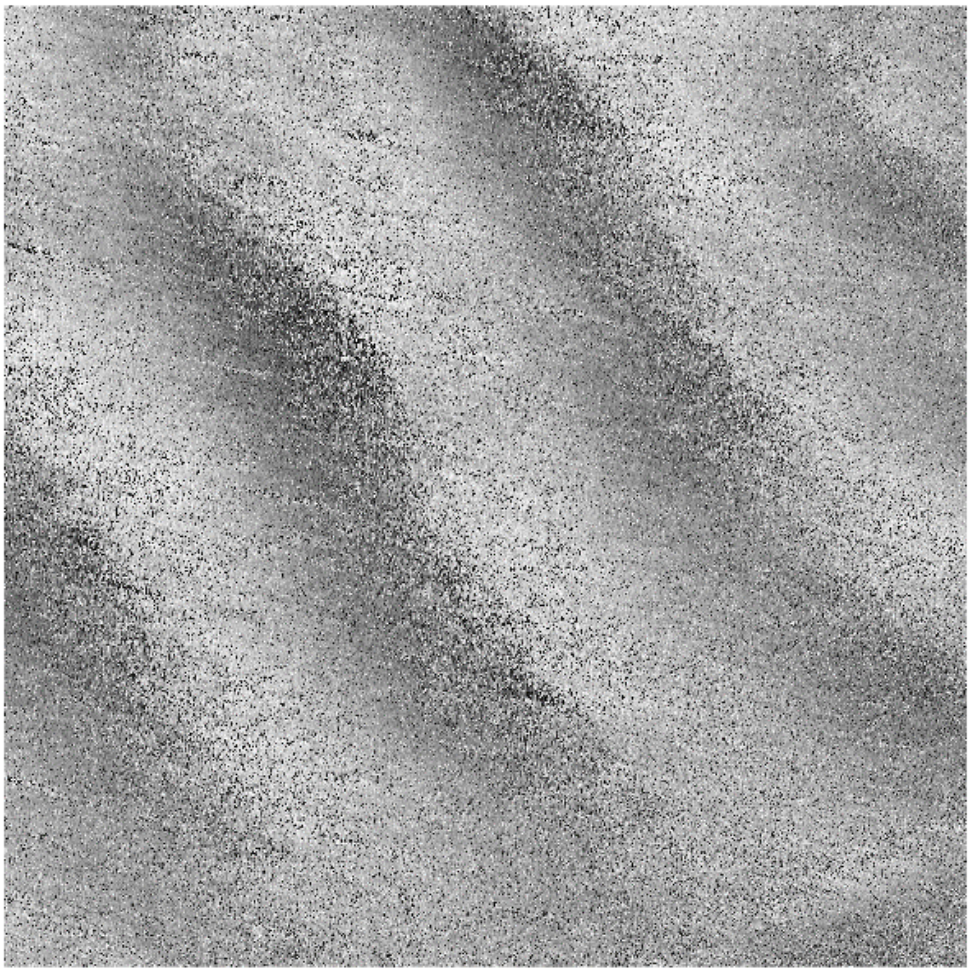

Figure 2.6. Interferometric phase: the result of multiplying one measurement form the first receiving antenna by the complex conjugate of the other measurement from the second receiving antenna.

2.3 FIELD EXPERIMENTS AND DATA COLLECTIONS

In this section, I introduce the different flight experiments that have been performed to collect the data used in this thesis. I was actively part of these flight experiments and I was able to fly onboard the ATI-SAR platform during data collection.

2.3.1 *Mouth of Columbia River, Oregon, USA: September 2016*

This flight experiment was a joint experiment by Jet Propulsion Laboratory (JPL), NASA and APL-UW. The joint JPL-APL experiment was performed in over a weeklong deployment in September 2016 off the Oregon coast over Columbia River mouth and Newport, OR. Table 2.2 lists the dates and active flight hours for this field experiment. The first three rows correspond to the Columbia River mouth experiment and the last row shows the information for the Newport experiment. Only data collected over Columbia River mouth are presented in this thesis. The average wind speed values during flights' hours in the area are also presented in Table 2.2.

Table 2.2. Data collection periods.

Flight Number	**Date**	**Measurement Period (PT)**	**Wind speed (m/s)**
1	2016-09-13	07:00 – 11:00	2.9
2	2016-09-14	14:00 – 17:30	7.1
3	2016-09-15	15:00 – 18:00	3.1
4	2016-09-16	13:00 – 15:00	-

The wind speed data were extracted from the SATURN-10 physical and biogeochemical observation station in the Columbia River estuary. Figure 2.7 shows the location of this station. This station is the closest station to the area under this study. SATURN-10 observation station's

wind speed values are available every ~20 minutes and they are accessible on Center for Coastal Margin Observation and Prediction (CMOP) website for public access [17].

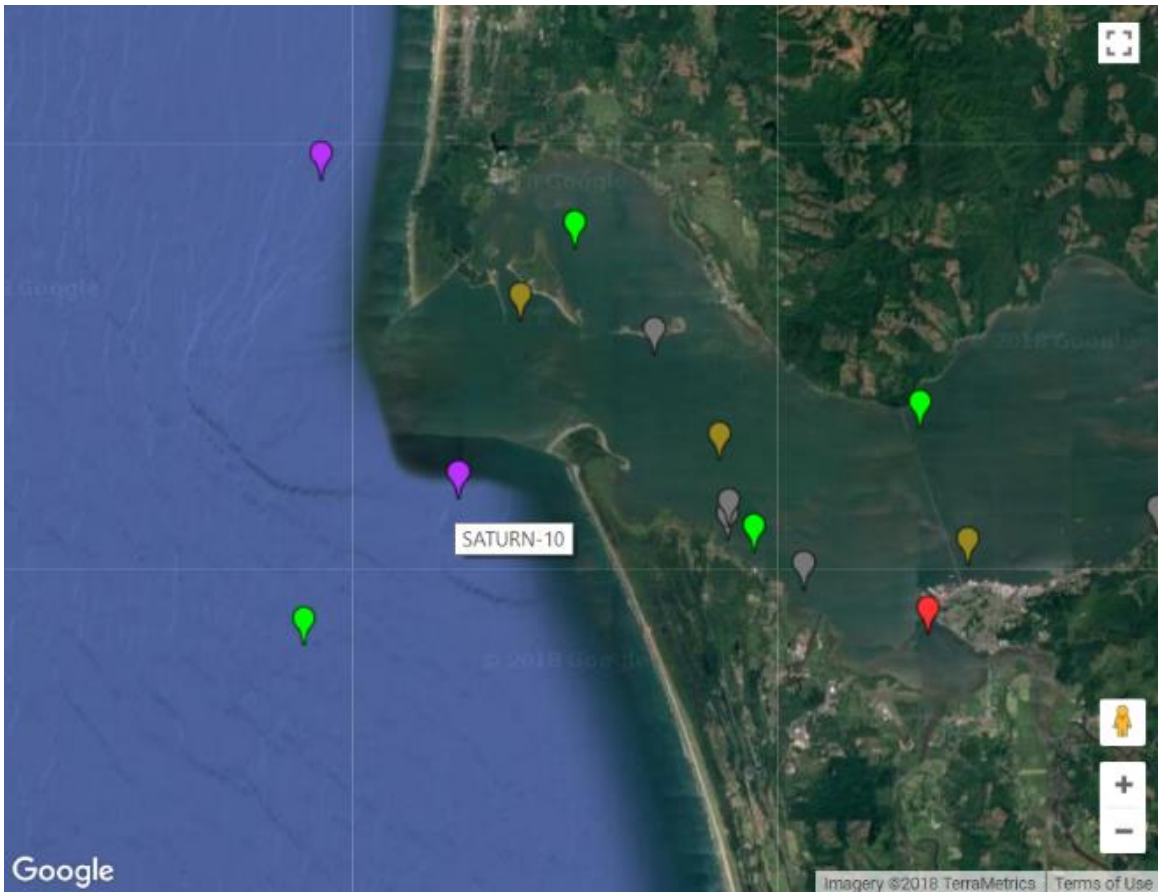

Figure 2.7. SATURN-10 station location near the Columbia River mouth [17].

Two collocation sites were selected based on a combination of interesting small-scale currents' features and a variety of available *in-situ* measurements and operational model products. The first site was at the Mouth of the Columbia River (MCR), where large (order m/s) tidally-driven currents create a plume in the Pacific Ocean during ebb tides.

The second site was close to Newport, OR, where sub-mesoscale (in the order of few tens of meters) structures are frequently visible in sea-surface temperature imagery.

Figure 2.8 depicts the flight paths for both APL-UW ATI-SAR platform and JPL's instrument during the experiment. The red lines are JPL's airplane flight paths and squares by the white and yellow lines present the flight paths for APL ATI-SAR. During the field experiment, the two radar instruments were flown on two different platforms in coordinated flight patterns. Both instruments measure the Doppler shift induced by the moving ocean surface currents.

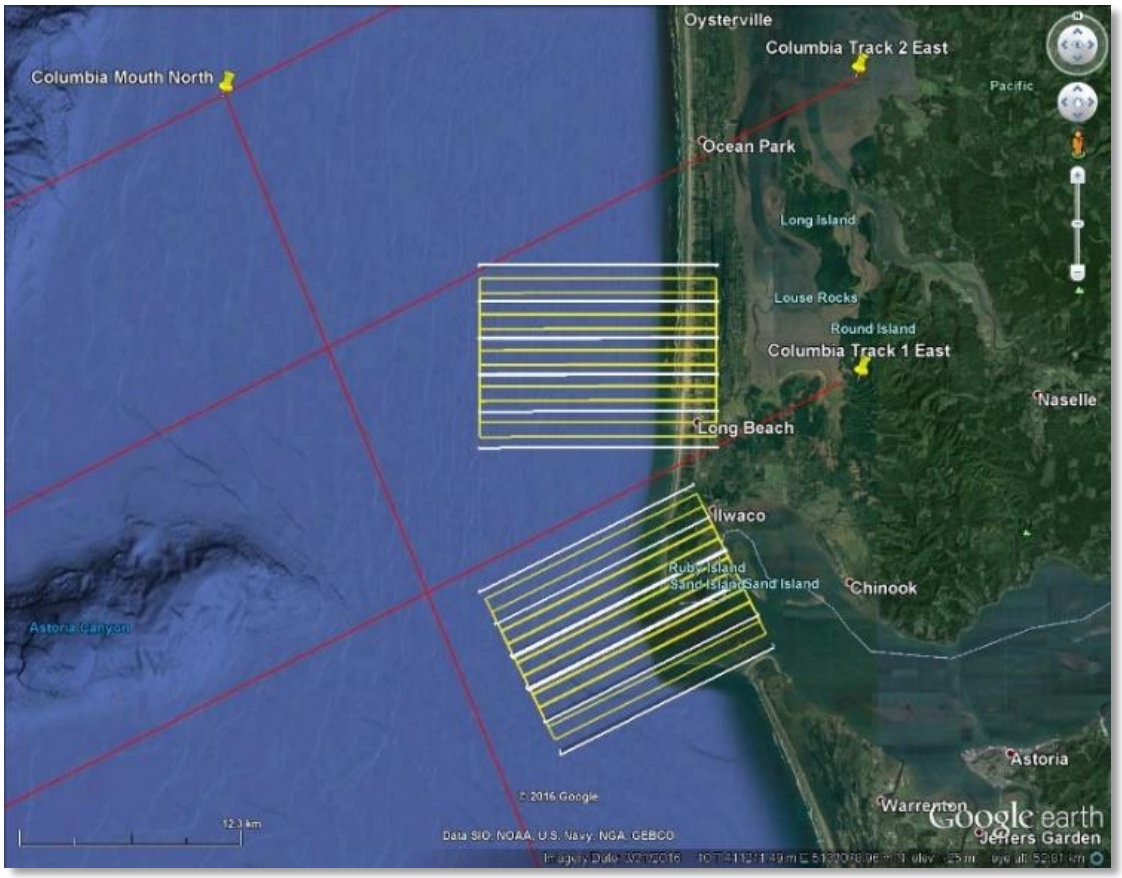

Figure 2.8. Flight patterns by APL ATI-SAR's platform at the Mouth of the Columbia River.

The JPL system is an airborne Ka-band Doppler scatterometer (DopplerScatt), designed to measure ocean surface currents and winds simultaneously. NASA Earth Science Technology Office (ESTO) funded DopplerScatt project through Research Opportunities in Earth and Space Science (ROSES) 2013 solicitations as an Instrument Incubator Program (IIP) [18]. To validate the DopplerScatt surface current measurements, surface velocity measurements are made with the APL-UW C-band ATI-SAR measurements. DopplerScatt was deployed on a King Air B200, at an altitude of around 10,000 m. The APL ATI-SAR was operated from a Cessna 172 at 3,000 ft altitude.

The JPL instrument is a spinning Ka-band pencil beam Doppler scatterometer (DopplerScatt). The term pencil beam refers to a relatively narrow antenna beam, illuminating an egg-shaped pattern on the surface. Based on the phase difference between pairs of pulses Doppler shift can be measured which infers the relative radial velocity of platform and surface motion. The average ground speed for the King Air was ~125 m/s during the field test, which was removed from the Doppler estimates using motion compensation algorithms to estimate the surface motion. The rotation of the antenna (~12.5 rpm) and nominal incidence angle (~56 degrees) enable wide swath coverage (~20 km) during the single pass of the aircraft [18].

Figure 2.9 shows the area covered by each instrument for a sample pass over the MCR. The gray-shaded area is an image of the DopplerScatt backscattered power for a single north-south pass, and the small tilted box over MCR depicts the area covered by APL-UW C-band ATI-SAR instrument [19].

The APL ATI-SAR coverage area is limited by its platform safety constraints of flying no more than ~15 km offshore. However, its measurement resolution is much finer than that of the JPL DopplerScatt instrument.

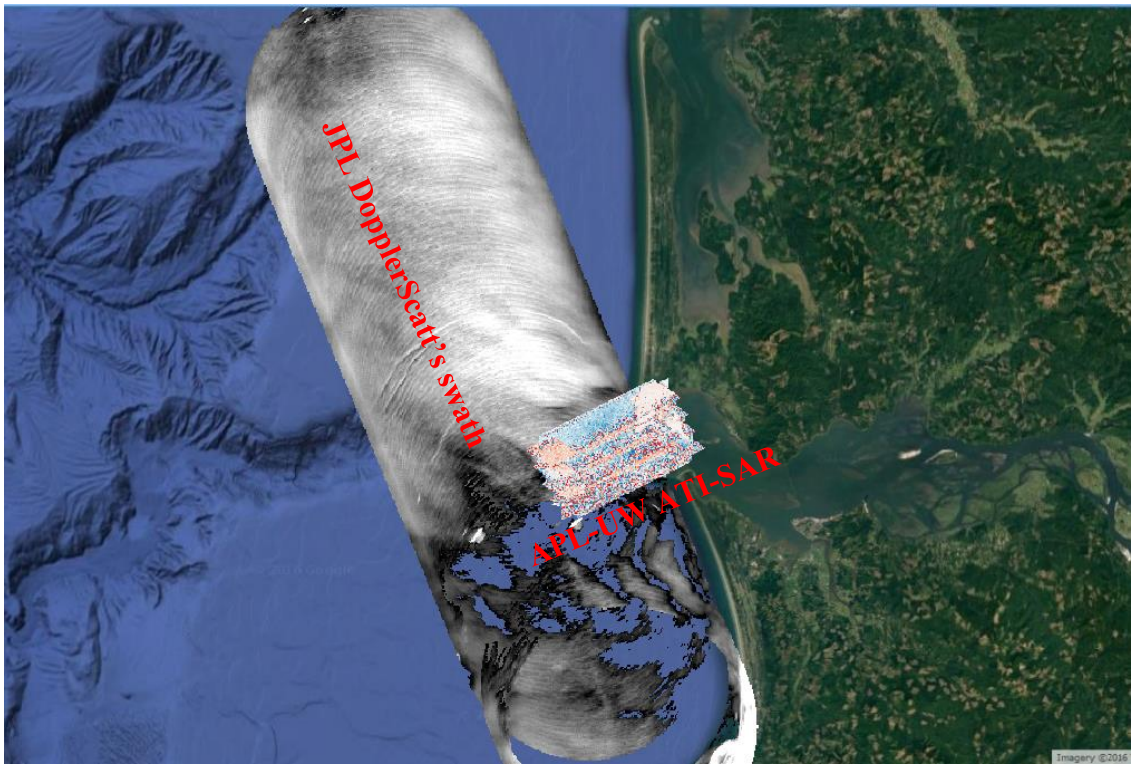

Figure 2.9. Covered area by APL ATI-SAR and JPL's DopplerScatt near the Mouth of the Columbia River [19].

2.3.2 *Point Sal, California, USA: September and October 2017*

Part of the airborne ATI-SAR data used in this research was collected during two campaigns in September and October 2017 over Point Sal, California, USA. These campaigns were part of the Innershelf Dynamics project supported by Office of Naval Research [20].

Table 2.3 and Table 2.4 list the flights of APL-UW airborne ATI-SAR onboard of the Cessna 182 aircraft and the time periods that microwave data was collected during the September and October 2017 campaigns, respectively.

The local average wind speed values during active flight hours are also displayed in Table 2.3 and Table 2.4. The wind speed values were measured by Scripps Institute of Oceanography's

mini met buoy, which was present at the scene at the time of the experiments [21]. The tables show that these data were collected in variety of wind and wave conditions.

Table 2.3. Data collection periods in September 2017.

Flight Number	Date	Measurement Period (UTC)	Average wind speed (m/s)
1	2017-09-10	20:35 – 21:35	3.0
2	2017-09-12	21:35 – 22:35	1.2
3	2017-09-13	20:10 – 00:40	3.8
4	2017-09-14	21:45 – 22:25	3.9
5	2017-09-15	18:40 – 00:00	8.0
6	2017-09-16	18:00 – 00:00	4.4
7	2017-09-17	19:30 – 21:15	3.8
8	2017-09-18	20:45 – 22:10	4.3

Table 2.4. Data collection periods in October 2017.

Flight Number	Date	Measurement Period (UTC)	Average wind speed (m/s)
1	2017-10-05	17:40 – 19:45	2.8
2	2017-10-06	16:20 – 17:20	1.4
3	2017-10-07	16:35 – 20:00	2.1
4	2017-10-11	20:35 – 23:00	2.5
5	2017-10-13	15:40 – 17:35	2.8
6	2017-10-14	15:35 – 21:00	0.7

Figure 2.10 - Figure 2.12 show three different flight patterns over Point Sal, CA. Figure 2.10 corresponds to the flight paths north of Point Sal and Figure 2.11 represents flight paths over Point Sal. Finally, Figure 2.12 shows flight pattern in the area south of Point Sal, CA.

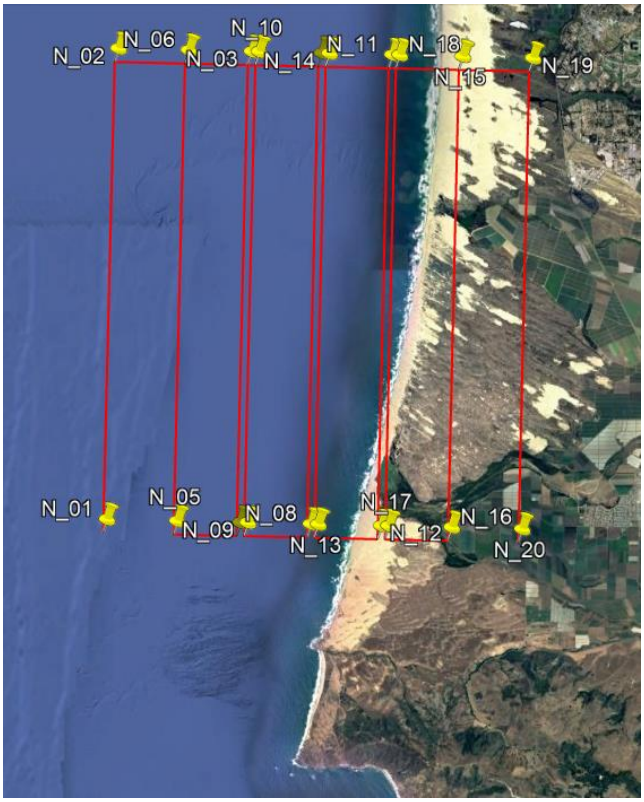

Northing (~20 km)

Easting (~17 km)

Figure 2.10. Flight pattern north of Point Sal, CA.

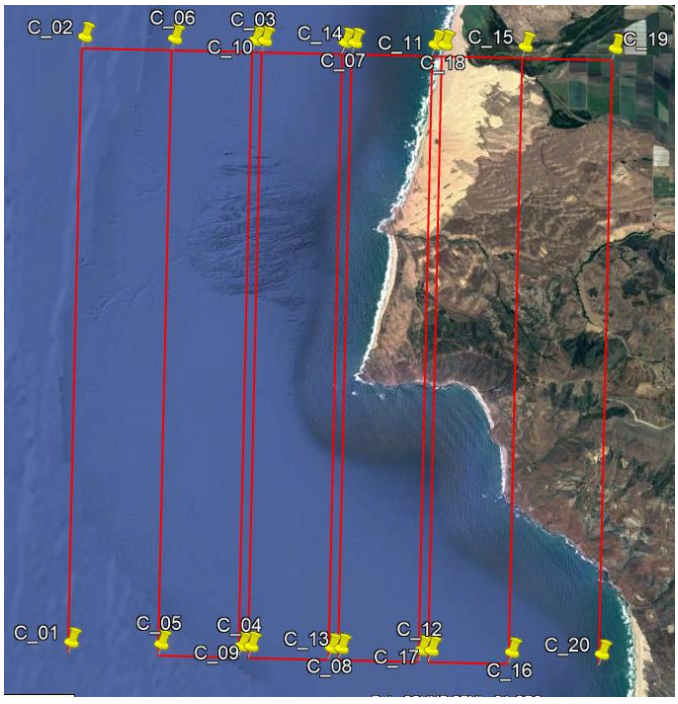

Northing (~15 km)

Easting (~15 km)

Figure 2.11. Flight pattern over Point Sal, CA.

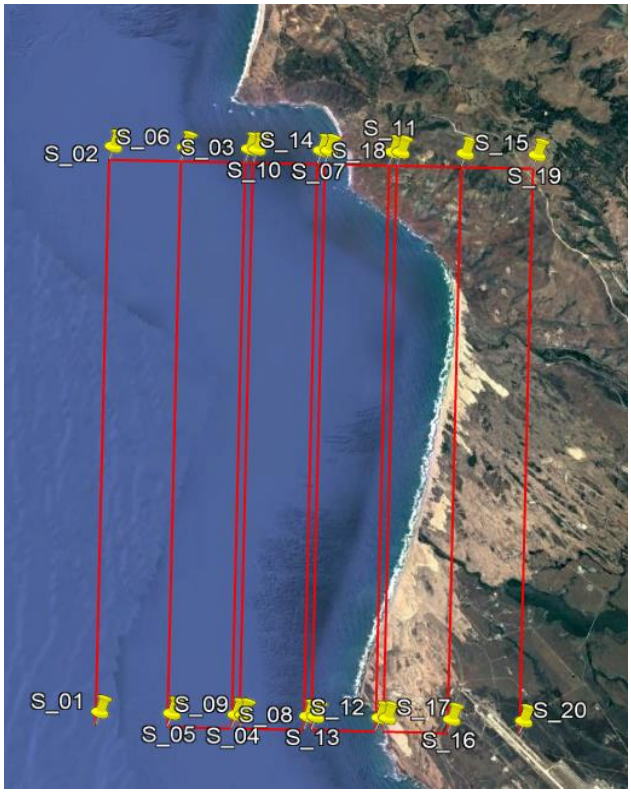

Northing (~17 km)

Easting (~17 km)

Figure 2.12. Flight pattern south of Point Sal, CA.

The data presented in this thesis was collected during the flight paths north of Point Sal, CA as shown in in Figure 2.10.

Figure 2.13 and Figure 2.14 show the covered area on the ground by the ATI-SAR north of Point Sal, CA during consecutive flight passes for northbound and southbound flights, respectively. Each parallelogram corresponds to one flight pass of data collection. In order to cover a larger area I have merged four different successive flight passes in each case. In Figure 2.13, the aircraft is flying from south to north and the radar antennas look at the starboard side of the aircraft (eastward).

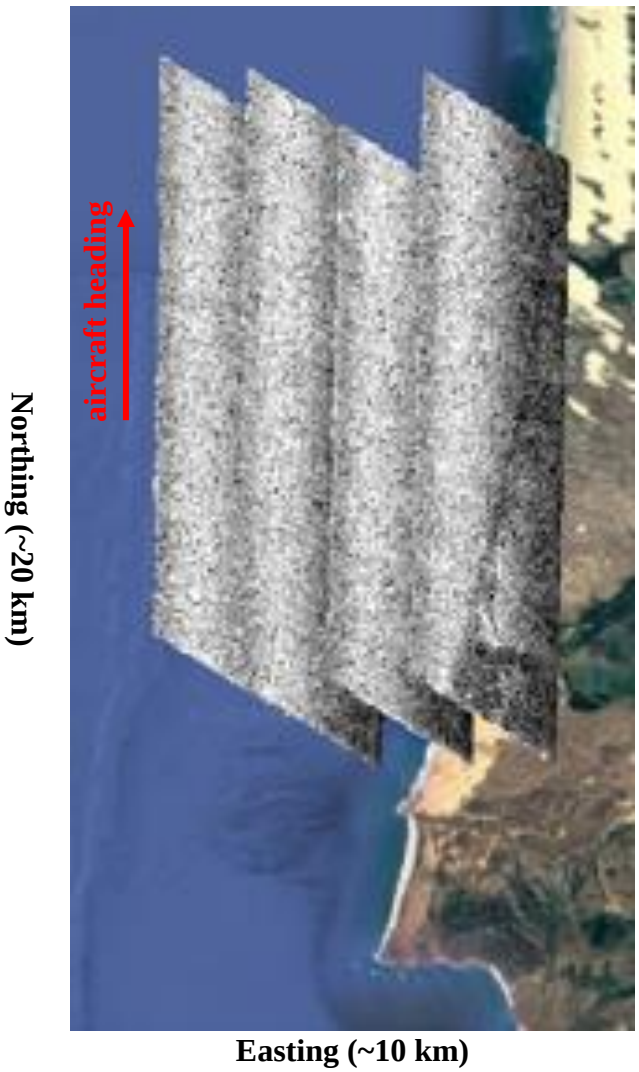

Figure 2.13. Area covered by the APL ATI-SAR north of Point Sal, CA during northbound flights [22]. The gray-shaded parallelograms represent relative signal to noise ratio captured by the ATI-SAR. White color corresponds to higher values of signal to noise ratios and black color corresponds to lower values of signal to noise ratio.

In Figure 2.14, the aircraft is flying from north to south and the ATI-SAR antennas still look towards the starboard side of the aircraft (westward). The gray-shaded parallelograms represent relative signal to noise ratio captured by the ATI-SAR. White represents higher values while black shows smaller values for the relative signal to noise ratio [22].

Figure 2.14. Covered area by APL ATI-SAR north of Point Sal, CA during southbound flights [22]. The gray-shaded parallelograms represent relative signal to noise ratio captured by the ATI-SAR. White color corresponds to higher values of signal to noise ratios and black color corresponds to lower values of signal to noise ratio.

The data collected during the flight experiments introduced in this chapter is used to retrieve nearshore surface current components using the algorithm, which will be explained in chapter 3.

Chapter 3. SURFACE CURRENT ESTIMATION

To retrieve ocean surface current at C-band using the data collected by APL ATI-SAR instrument, the technique presented in [14] is used. In the retrieval algorithm, first the Doppler velocity ($V_{Doppler}$) is calculated from the interferometric phase (equation (2.2)) measured by ATI-SAR. Doppler velocity represents the mean Doppler shift induced on the incident electromagnetic wave by ocean surface.

Since land is not moving, the interferometric phase over land should be zero. However, because of calibration issues of the system, variation in interferometric phase over land is observed. To remove the phase variation over land, mean phase offset over land is calculated and subtracted from the measured Doppler velocity in order to calculate radial component of surface velocity. More details about APL ATI-SAR phase calibration can be found in [23], [24] and [25].

As equation (3.3) shows there are other contributions to the measured Doppler velocity and it is not simply related to the radial velocity of surface current (V_{radial}). Under conditions in which composite surface scattering theory describes the microwave scattering (moderate incidence angle and no breaking waves) the Doppler velocity will be the sum of the velocity components presented in equation (3.3).

$$V_{Doppler} = V_{radial} + V_b + V_d + V_o \tag{3.3}$$

$V_{Doppler}$ is calculated on the surface after applying the required corrections for the radar platform (aircraft) motion compensation, such as roll, pitch and yaw variation. All the velocity contributions to the Doppler velocity in equation (3.3) have to be in the radial direction for each radar look direction (forward- and aft-squinted radar look directions).

The surface wind-drift current (V_d) and phase velocity of the Bragg-resonant scatterers (V_b) are subtracted from the Doppler velocity in order to make measurement of the radial component of surface current.

There is also another contribution (V_o) to the Doppler velocity, which is the orbital velocity of the gravity waves. In former publications, it was assumed that the wave orbital velocities average to zero over a number of wave periods [26]. However, recent publications [27][28] argue that there are wave-dependent biases in the ATI-SAR retrieved radial velocities. The ATI-SAR surface current retrieval algorithm in its present version does not attempt to remove V_o from the measured Doppler velocity [14] and all the surface current components which will be presented at the end of this chapter are calculated without removing the contribution of orbital velocity of the gravity waves (V_o) from the Doppler velocity. In chapter 5, I will introduce a modification to the retrieval algorithm, which tries to include the contribution of the orbital velocity of the gravity waves (V_o) in the ATI-SAR radial velocity calculations. After applying these modifications to the retrieval algorithm, the x- and y-components of surface current are computed from the forward- and aft-squinted radial velocity measurements.

In order to interpret the Doppler velocity, first I need to briefly describe the scattering mechanism what, in fact, is causing the scatter of the radar waves.

3.1 BRAGG SCATTER FROM WATER WAVES.

The dominant scattering mechanism for airborne microwave radar is due to resonant interaction of electromagnetic waves with the ocean surface, a process known as Bragg scattering. For microwave frequencies, Bragg waves are gravity capillary waves with wavelength of a few centimeters. They travel with a phase velocity that depends on their wavelength and induce a Doppler shift on the reflected electromagnetic wave.

In the surface current retrieval algorithm, the Bragg velocity (V_b) must be removed from the Doppler velocity in order to calculate ocean surface radial velocity. Since a direct measure of the Bragg resonant wave contribution is not available, I use a model and local wind measurements to estimate the Bragg contribution to the Doppler shift [14]. To remove the Bragg component of the velocity the magnitude of the Bragg velocity is calculated first. To calculate the phase speed of the Bragg-resonant capillary-gravity waves equation (3.4) is used:

$$|V_{Bragg}| = \sqrt{\frac{g}{k_{Bragg}} + \frac{surface\ tension}{water\ density}\ k_{Bragg}} \tag{3.4}$$

This is measured in the frame of reference in which the water is stationary. One can see that these waves are intermediate between deep buoyancy waves and pure capillary waves. Surface tension is the elastic tendency of a fluid surface, which tends to minimize the surface area. Surface tension is a significant restoring force for Bragg waves (see Table 3.5 below). The sea water surface tension value used in the surface current retrieval algorithm is 0.074 [N/m]. Sea water has also a density of 1025 [kg/m^3].

k_{Bragg} is the wave number of the Bragg waves; it is calculated from equation (3.5).

$$k_{Bragg} = \frac{2\pi}{\lambda_i}\ 2sin\theta_i \tag{3.5}$$

In equation (3.5), λ_i is the incident wavelength at C-band, which is near 6 cm for the APL ATI-SAR system, and θ_i is the radar incidence angle. Figure 3.1 shows the geometry under which the Bragg wavelength is calculated.

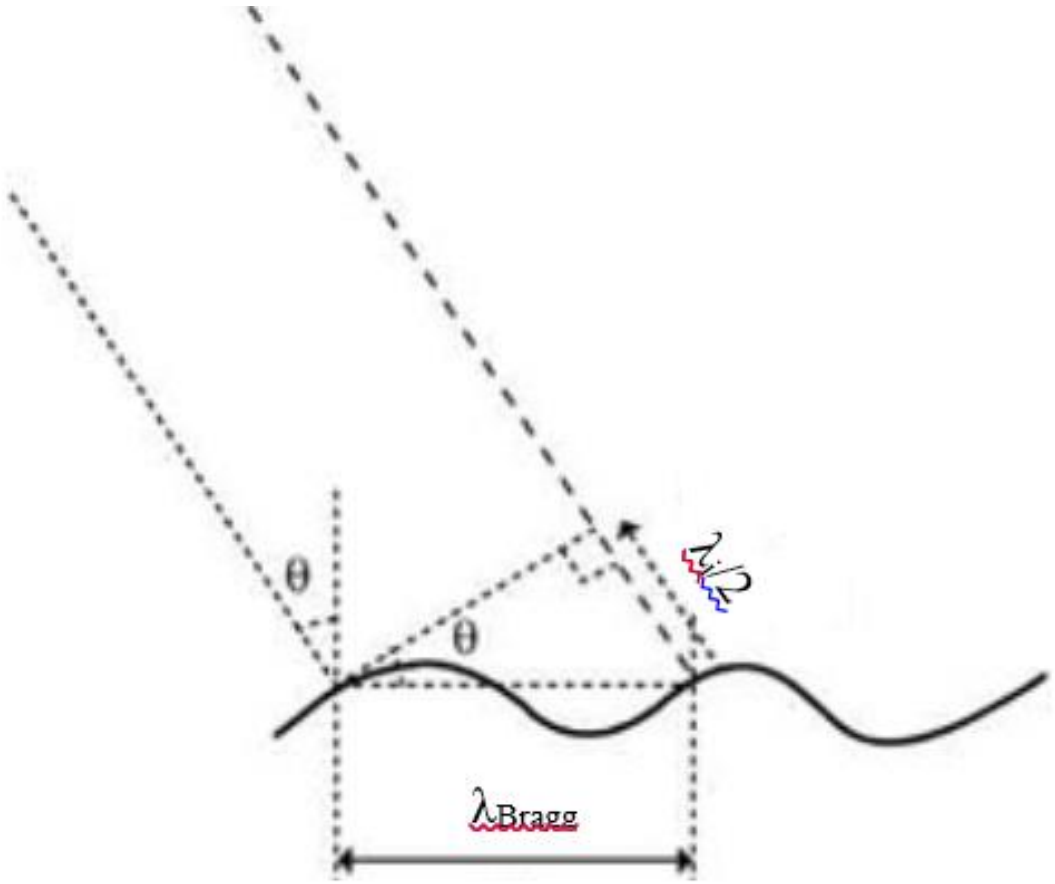

Figure 3.1. Geometry of Bragg wavelength [29].

The APL-UW ATI-SAR incidence angle varies in the range of 40-75 degrees and has a nominal value of 60 degrees during the experiments to collect data used in this research. Table 3.5 shows the calculated values for Bragg wavelength, Bragg wave number and contribution of the Bragg-resonant capillary waves and gravity waves to the magnitude of the Bragg velocity presented in equation (3.4) for different incidence angle. As presented for low incidence angles, gravity waves have larger contribution. As incidence angle increases, the contribution of capillary waves becomes comparable to that of the gravity waves, however.

Table 3.5. Bragg velocity calculations at different incidence angles.

θ_i [degrees]	λ_{Bragg} [m]	k_{Bragg} [m]	Capillary wave contribution $\left(\frac{surface\ tension}{water\ density}\ k_{Bragg}\right)$	Gravity waves contribution $\left(\frac{g}{k_{Bragg}}\right)$	$\lvert V_{Bragg}\rvert$ [m/s]
40	4.3×10^{-2}	145	0.010	0.068	0.279
60	3.2×10^{-2}	196	0.014	0.050	0.253
75	2.9×10^{-2}	218	0.016	0.045	0.246

There is an empirical model $G(\psi) = \cos^{2n}(\frac{\psi}{2})$ for the directional spreading of Bragg resonant waves [26]; the exponent *n* is taken to be equal to 1 in the retrieval algorithm used in this research [14]. In order to consider the direction of the Bragg velocity component, the parameter ψ should be introduced, which is the angle between the radar boresight and the wind direction with the convention of downwind being equal to zero degrees. Equation (3.6) gives the value of ψ for each incidence angle θ and azimuth angle φ.

$$\psi = \cos^{-1}\left(\frac{q_x * wind_x + q_y * wind_y}{\sqrt{wind_x^2 + wind_y^2}}\right) \tag{3.6}$$

Where q_x, q_y and q_z are three components of the unit vector $\boldsymbol{q}$ of the radar boresight direction and are given by a set of equations (3.7).

$$\begin{aligned} q_x &= \cos\phi * \sin\theta \\ q_y &= \sin\phi * \sin\theta \\ q_z &= -\cos\theta \end{aligned} \tag{3.7}$$

Also in equation (3.6) $wind_x$ and $wind_y$ are the x- and y-components of sea surface wind and are given by equation set (3.8).

$$wind_x = wind\ speed * \cos(wind\ direction)$$
$$wind_y = wind\ speed * \sin(wind\ direction) \quad (3.8)$$

Wind speed and wind direction are secondary geophysical parameters in the surface current retrieval algorithm and they need to be inserted to the algorithm from other sources. In this research, to run the retrieval algorithm with the data collected over MCR (introduced in section 2-2-1) wind speed and wind direction values are taken from the SATURN-10 station. In the case of running the surface current retrieval algorithm using the data collected over Point Sal, CAL (introduced in section 2-2-2) mini met buoy's measurements operated by Scripps Institute of Oceanography provide wind speed and wind direction values.

The relative spectral densities of approaching and receding waves are used to determine V_b from equation (3.9) [26].

$$V_b = \left|V_{Bragg}\right| \frac{G(\psi) - G(\psi+\pi)}{G(\psi) + G(\psi+\pi)} \quad (3.9)$$

Having the magnitude of the Bragg velocity from equation (3.4), equation (3.10) gives the value of radial component of the Bragg velocity, which should be removed from the Doppler radial velocity measured by ATI-SAR.

$$V_b = \left|V_{Bragg}\right| \frac{\cos^2\left(\frac{\psi}{2}\right) - \cos^2\left(\frac{\psi+\pi}{2}\right)}{\cos^2\left(\frac{\psi}{2}\right) + \cos^2\left(\frac{\psi+\pi}{2}\right)} \quad (3.10)$$

Using trigonometry, equation (3.10) can be simplified considerably. The simplified version of it is shown in equation (3.11).

$$V_b = \left|V_{Bragg}\right| \left(1 - 2\sin^2\frac{\psi}{2}\right) \quad (3.11)$$

Another velocity contribution, which should be removed from the retrieved radial velocity, is the radial component of the wind-drift velocity (V_d in equation (3.3)). This is the surface wind contribution to the Doppler measurement and it should be removed in order to measure the radial component of surface current. Because the surface is comprised of a fluid (water) that can move, the surface is dragged along by the wind. The wind-drift current relationship with wind speed has shown significant variability in the literature ranging between 2.6% and 5.5% of the ambient wind speed [30]. In this research, the wind drift is included as 3.5% of the wind speed. Therefore, the radial component of V_d is calculated from equation (3.12).

$$V_d = 0.035(\, wind_x * q_x + wind_y * q_y) \tag{3.12}$$

Eventually the radial velocity is retrieved after subtracting V_b and V_d from the Doppler velocity as presented in equation (3.3). One must recall that the contribution from the orbital velocity of gravity waves (V_o) either has been presumed zero mean [26] or is not removed from the measured Doppler velocity [14] in the present version of the surface current retrieval algorithm.

3.2 ATI- SAR RADIAL VELOCITY RETRIEVAL OVER MOUTH OF COLUMBIA RIVER

Since the ATI-SAR has both forward- and aft-squinted antennas, the algorithm is capable of calculating two radial velocity components for each flight pass of the ATI-SAR platform. Figure 3.2 and Figure 3.3 show forward- and aft-looking radial velocity estimated by APL ATI-SAR over the Columbia River mouth, respectively.

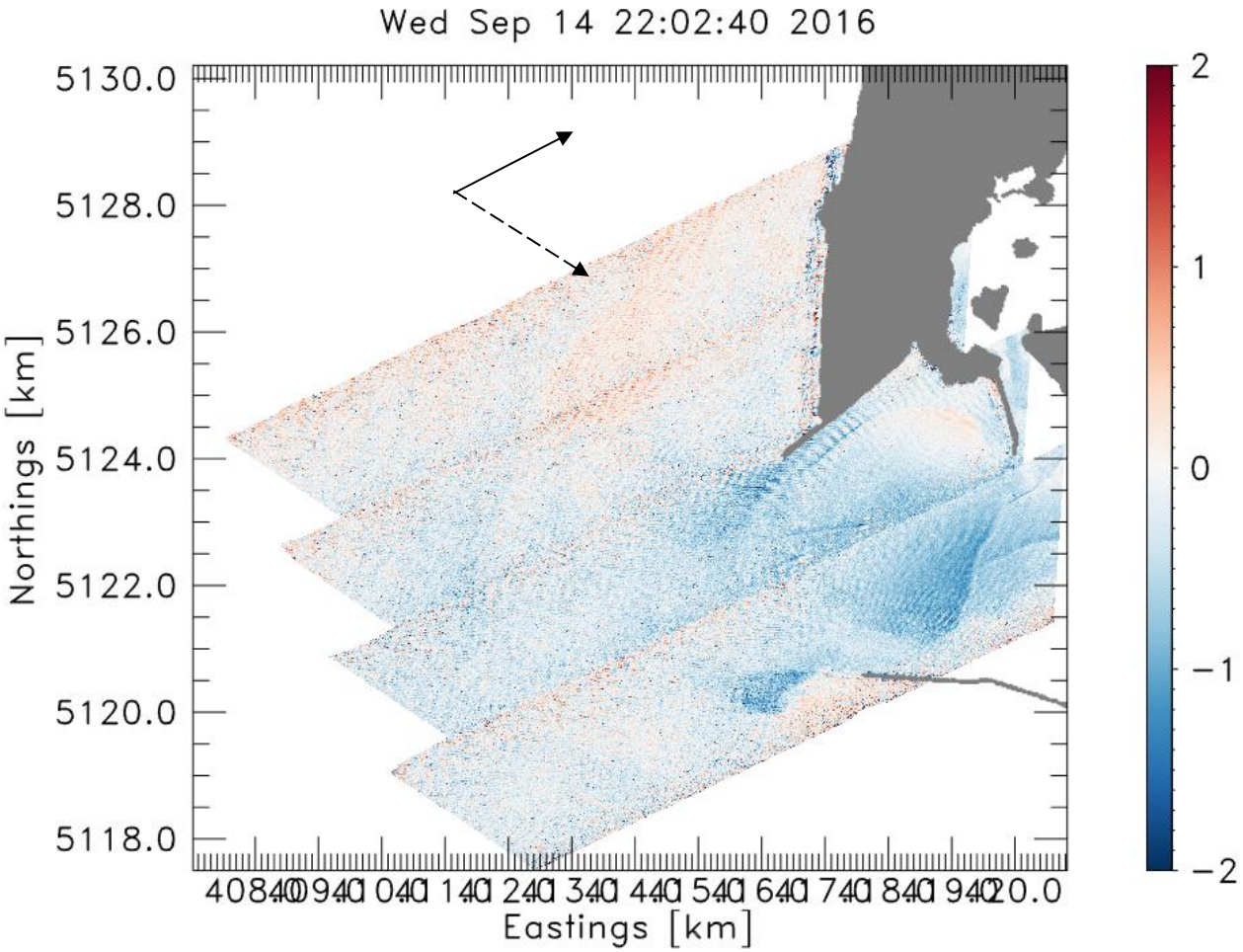

Figure 3.2. Forward-looking radial velocity [m/s] estimates by ATI-SAR over Columbia River Mouth. The solid arrow shows the aircraft heading direction and the dashed arrow shows the radar look direction [19].

The color shows radial velocity, which varies over a range of ±2 m/s. The times shown at top of the images are in GMT. In order to show the velocity fields over larger area four flight tracks were merged and the results are presented. As depicted in Figure 3.2 forward-looking radial velocities have negative values (in blue color). Also, one can see in Figure 3.3 that aft-looking radial velocities have positive values (red color) over MCR.

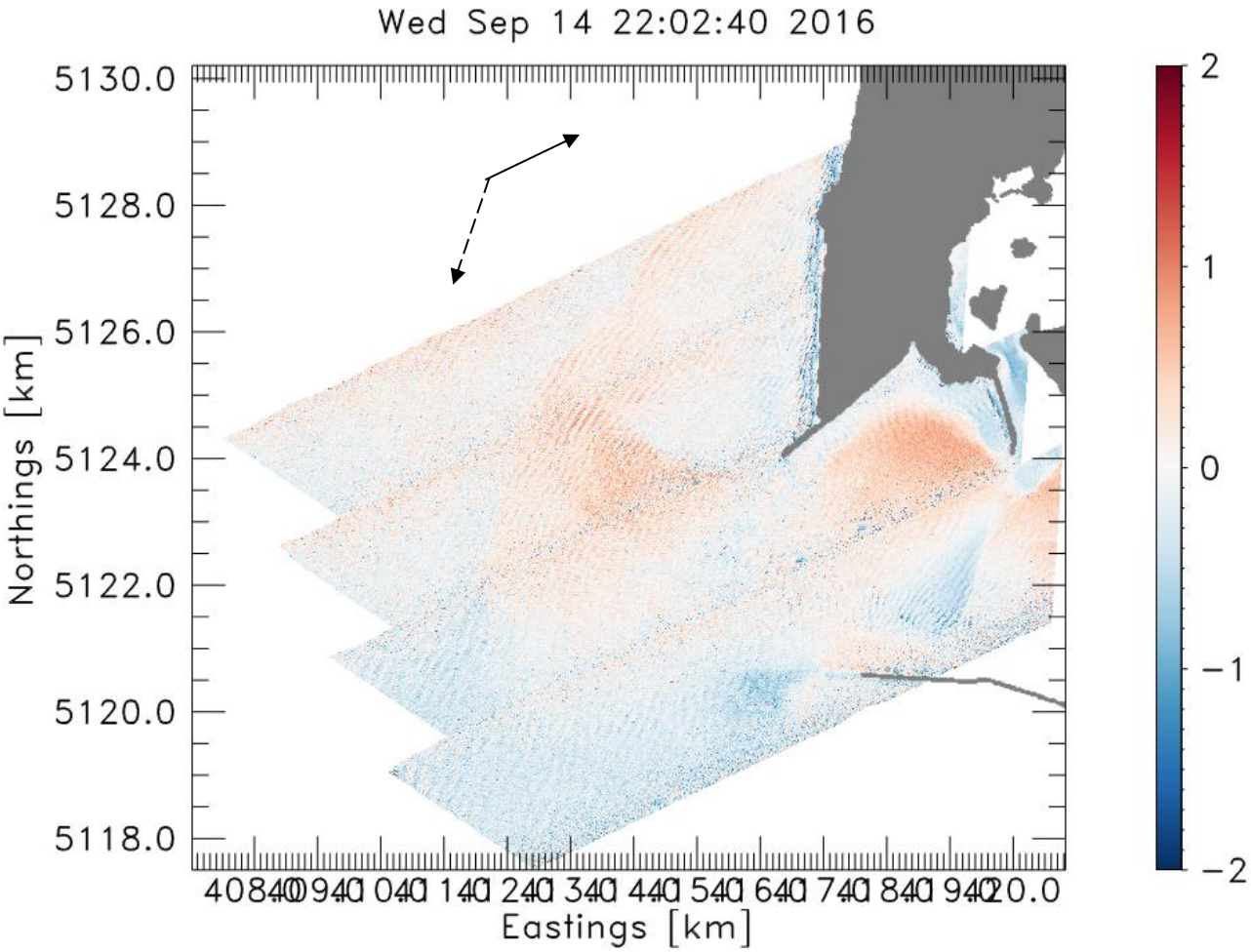

Figure 3.3. Aft-looking radial velocity [m/s] estimates by ATI-SAR over Columbia River Mouth. The solid arrow shows the aircraft heading direction and the dashed arrow shows the radar look direction [19].

Using trigonometry presented in Figure 3.4 and from forward-looking radial velocity (v_r^+) and aft-looking radial velocity (v_r^-), x- and y-components of surface current can be calculated (v_x and v_y respectively).

Equations (3.13) represents how x- and y-components of surface current can be calculated from forward- and aft-looking radial velocities.

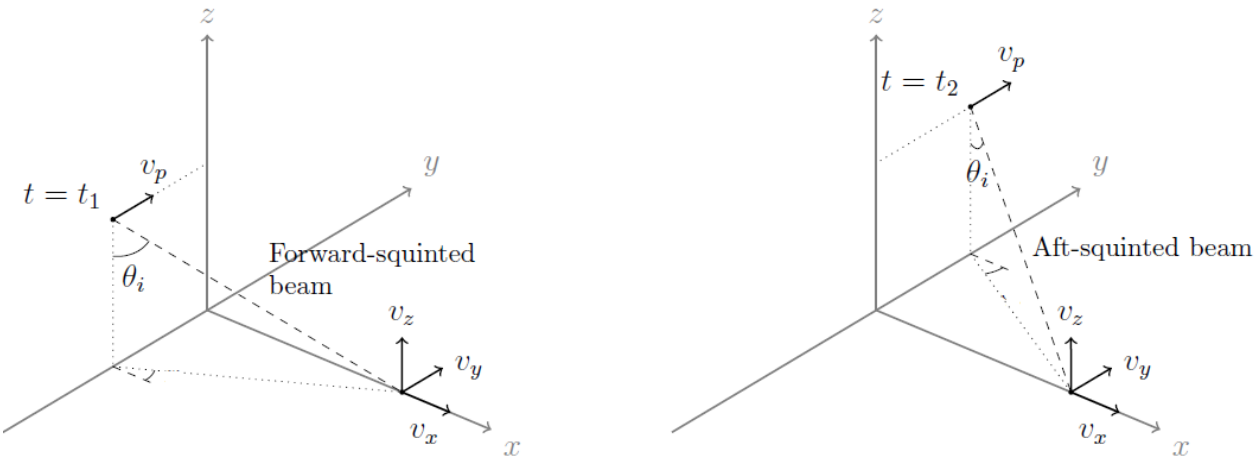

Figure 3.4. Dual-beam ATI-SAR measurement geometry. v_p is the platform velocity in y direction. Two Doppler measurements are recorded from the same scattering point on the surface: the first one at time t_1 with the forward-squinted antenna, and the second one at time t_2 with the aft-squinted antenna [12].

$$v_x = \frac{v_r^+ sin\theta_i^- sin\theta_s^- - v_r^- sin\theta_i^+ sin\theta_s^+}{sin\theta_i^+ sin\theta_i^- sin(\theta_s^- - \theta_s^+)}$$
$$v_y = \frac{-v_r^+ sin\theta_i^- cos\theta_s^- + v_r^- sin\theta_i^+ cos\theta_s^+}{sin\theta_i^+ sin\theta_i^- sin(\theta_s^- - \theta_s^+)} \quad (3.13)$$

Here θ_i is the incidence angle and θ_s is the squint angle. The superscript + and – refers to the forward-squinted and aft-squinted radar looks, respectively.

3.3 SURFACE CURRENT COMPONENTS RETRIEVAL OVER POINT SAL, CA

I used the algorithm introduced earlier this chapter to generate x-(east) and y-(north) components of surface current over Point Sal, CA from ATI-SAR data collected during the flight experiment introduced in section 2.3.2. In order to present surface current components over larger area data collected during four flight tracks merged for each case. To show the consistency of the APL ATI-SAR system operation, I present x- and y- components of surface current for different flight passes over a 4-hr flight period performed in September 15 2017 in Figure 3.5 – Figure 3.12. Amongst the different flight patterns presented in Figure 2.10 - Figure 2.12, during the September 15 flight experiment the focus was on the flight pattern north of Point Sal, CA presented in Figure 2.10.

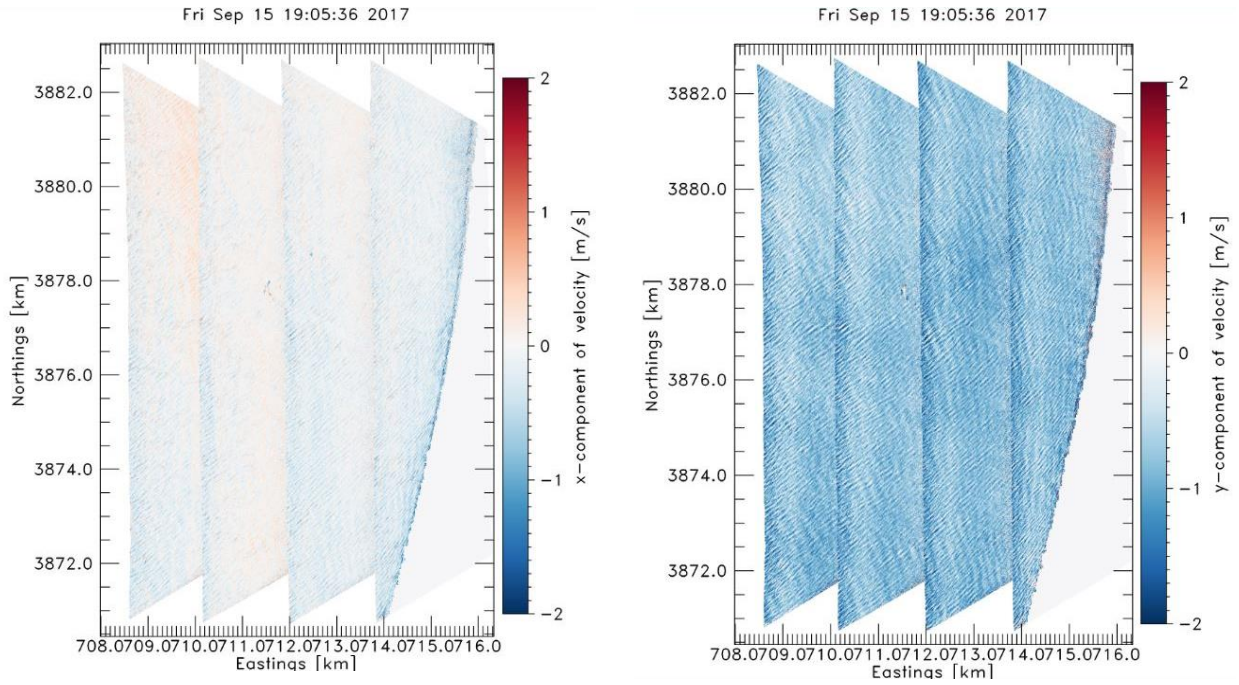

Figure 3.5. x- (left panel) and y- (right panel) components of surface current measured by ATI-SAR over Point Sal, CA during northbound flights for September 15 2017 19:05:36 GMT.

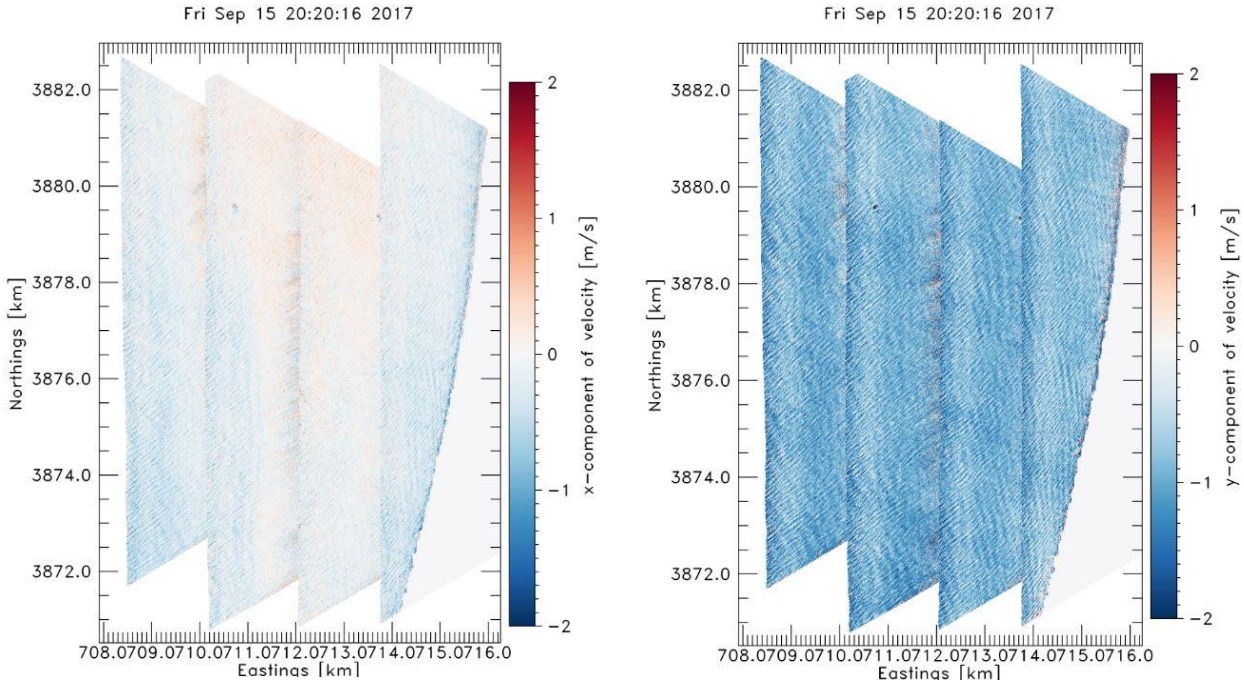

Figure 3.6. x- (left panel) and y- (right panel) components of surface current measured by ATI-SAR over Point Sal, CA during northbound flights for September 15 2017 20:20:16 GMT.

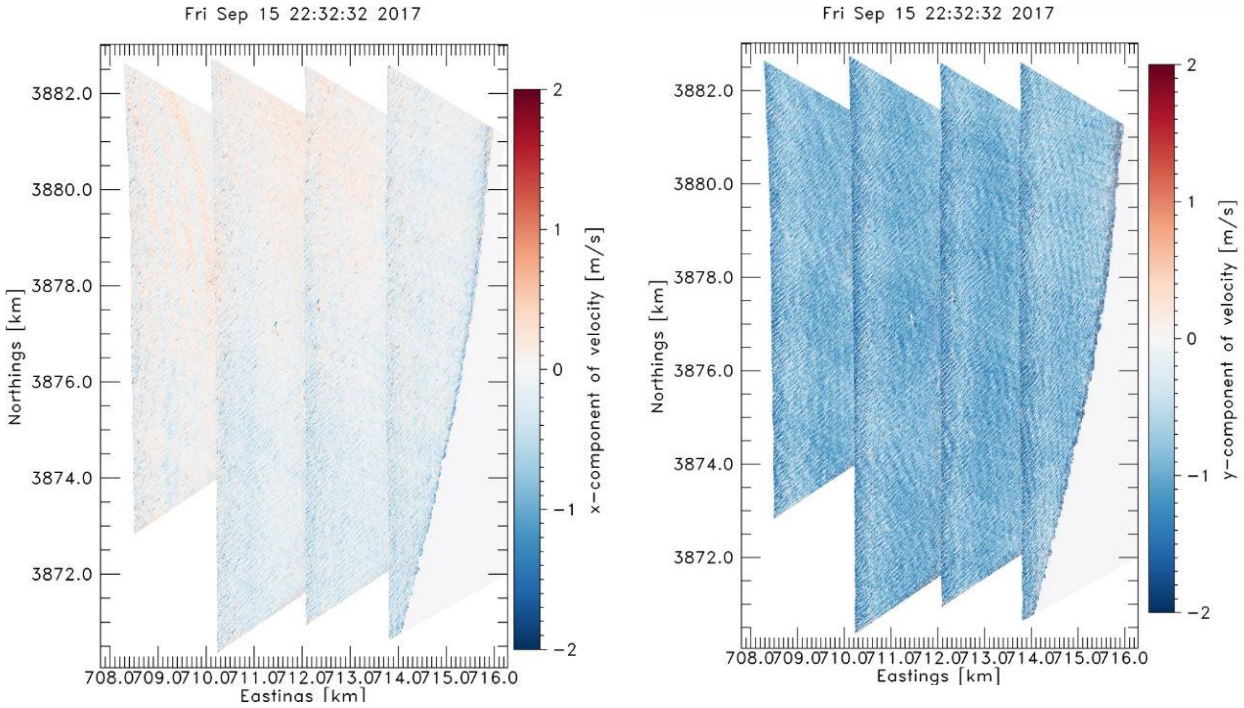

Figure 3.7. x- (left panel) and y- (right panel) components of surface current measured by ATI-SAR over Point Sal, CA during northbound flights for September 15 2017 22:32:32 GMT.

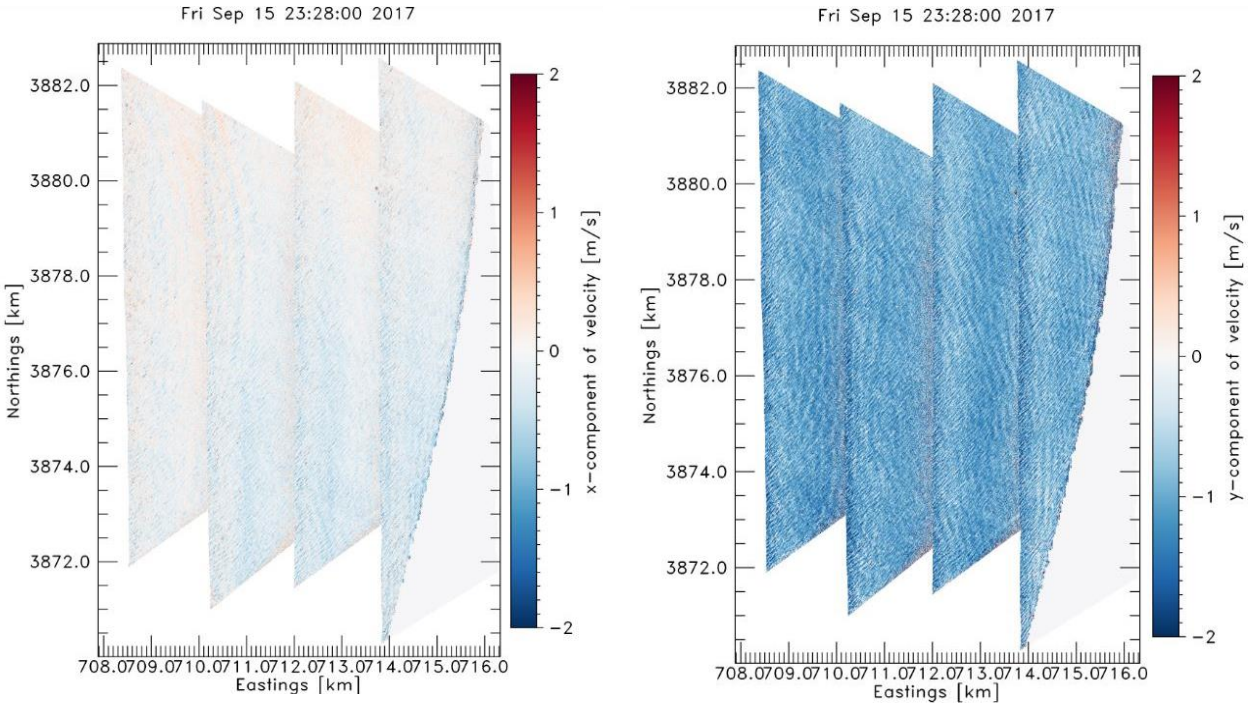

Figure 3.8. x- (left panel) and y- (right panel) components of surface current measured by ATI-SAR over Point Sal, CA during northbound flights for September 15 2017 23:28:00 GMT.

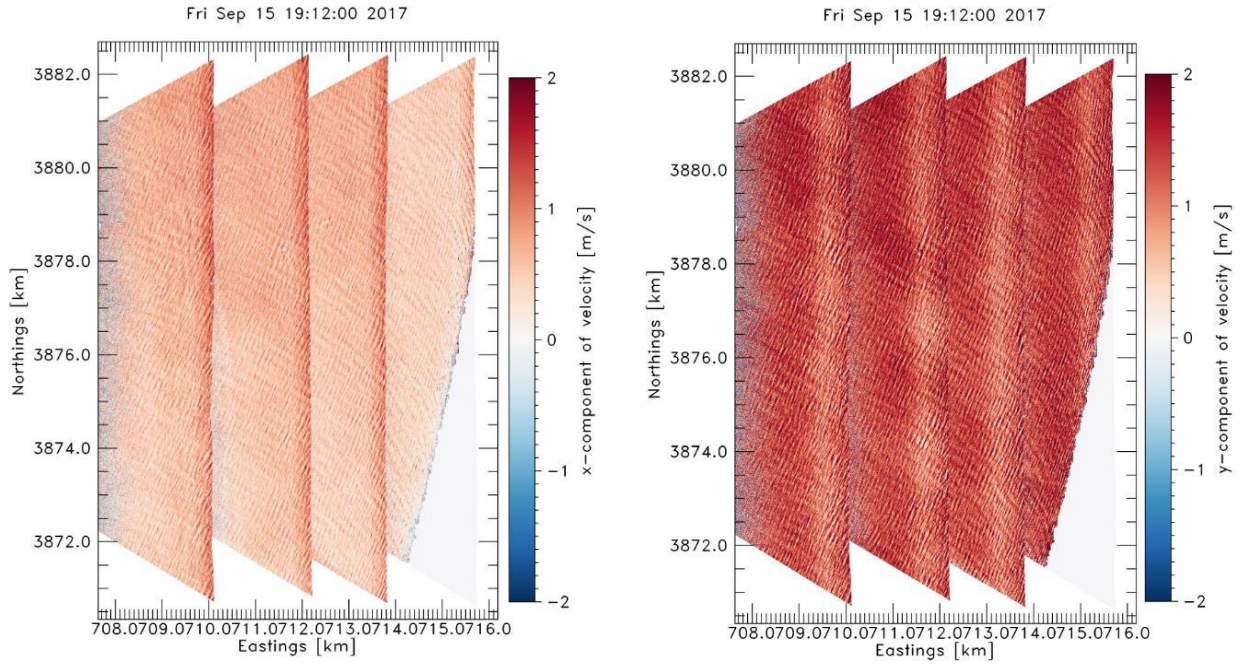

Figure 3.9. x- (left panel) and y- (right panel) components of surface current measured by ATI-SAR over Point Sal, CA during southbound flights for September 15 2017 19:12:00 GMT.

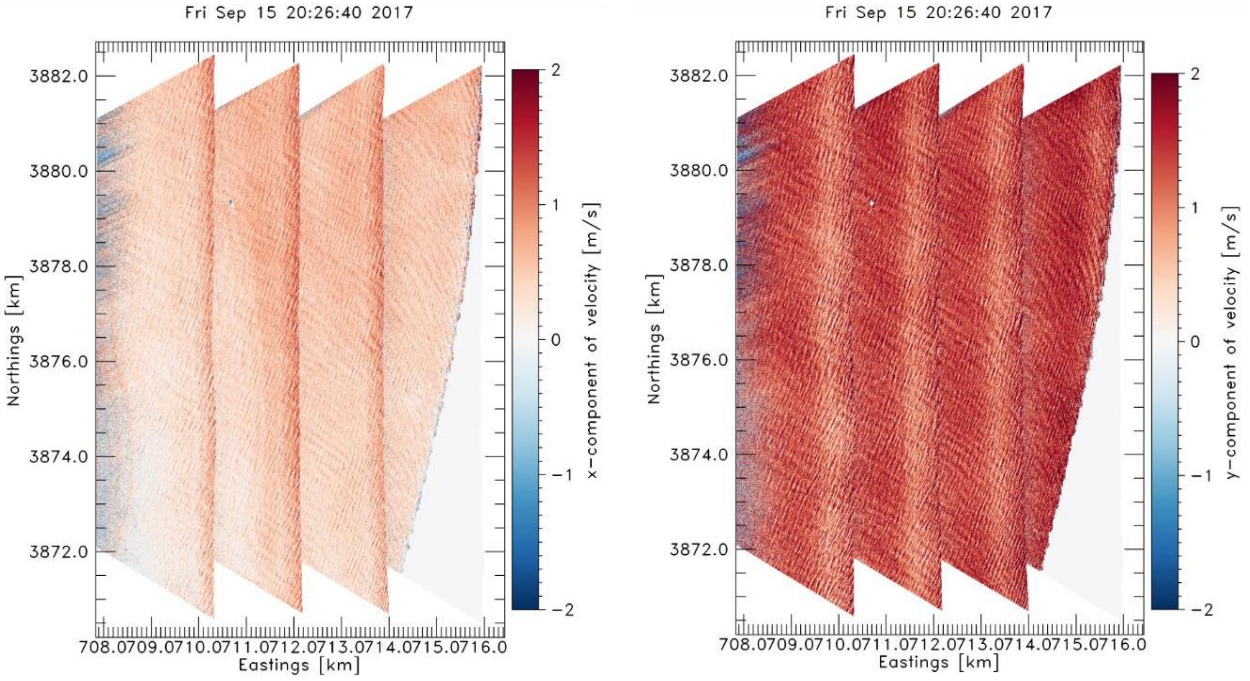

Figure 3.10. x- (left panel) and y- (right panel) components of surface current measured by ATI-SAR over Point Sal, CA during southbound flights for September 15 2017 20:26:40 GMT.

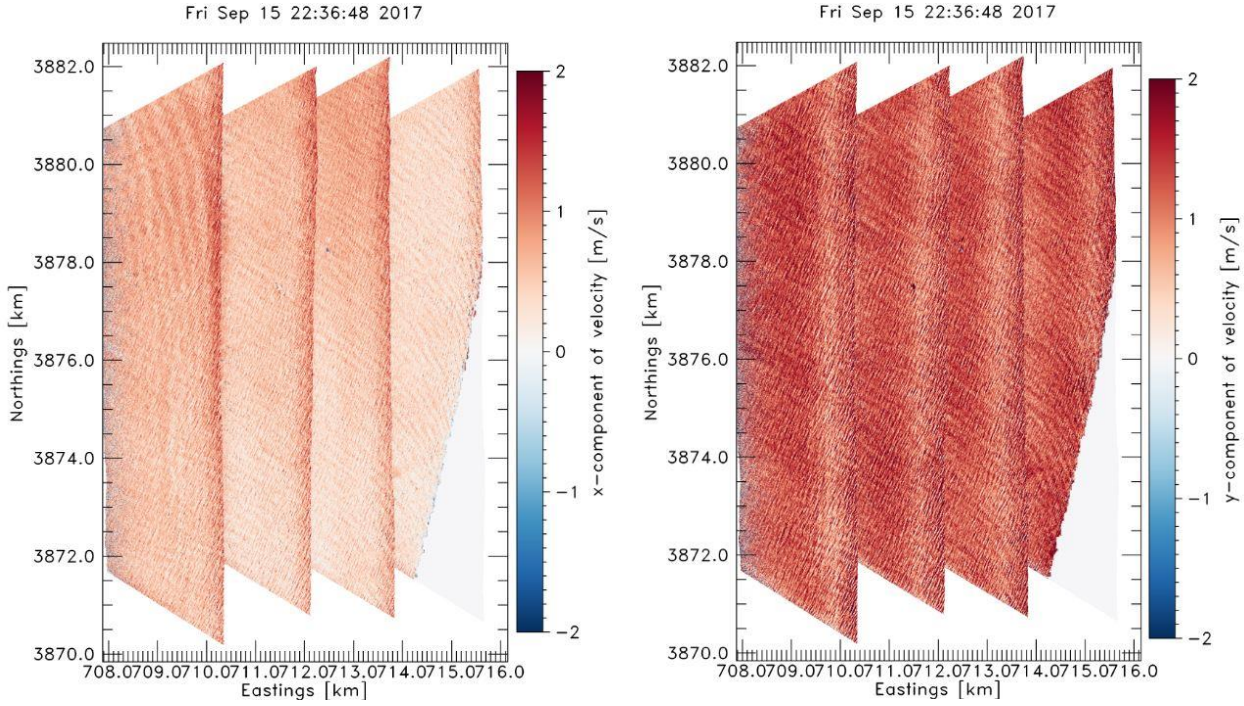

Figure 3.11. x- (left panel) and y- (right panel) components of surface current measured by ATI-SAR over Point Sal, CA during southbound flights for September 15 2017 22:36:48 GMT.

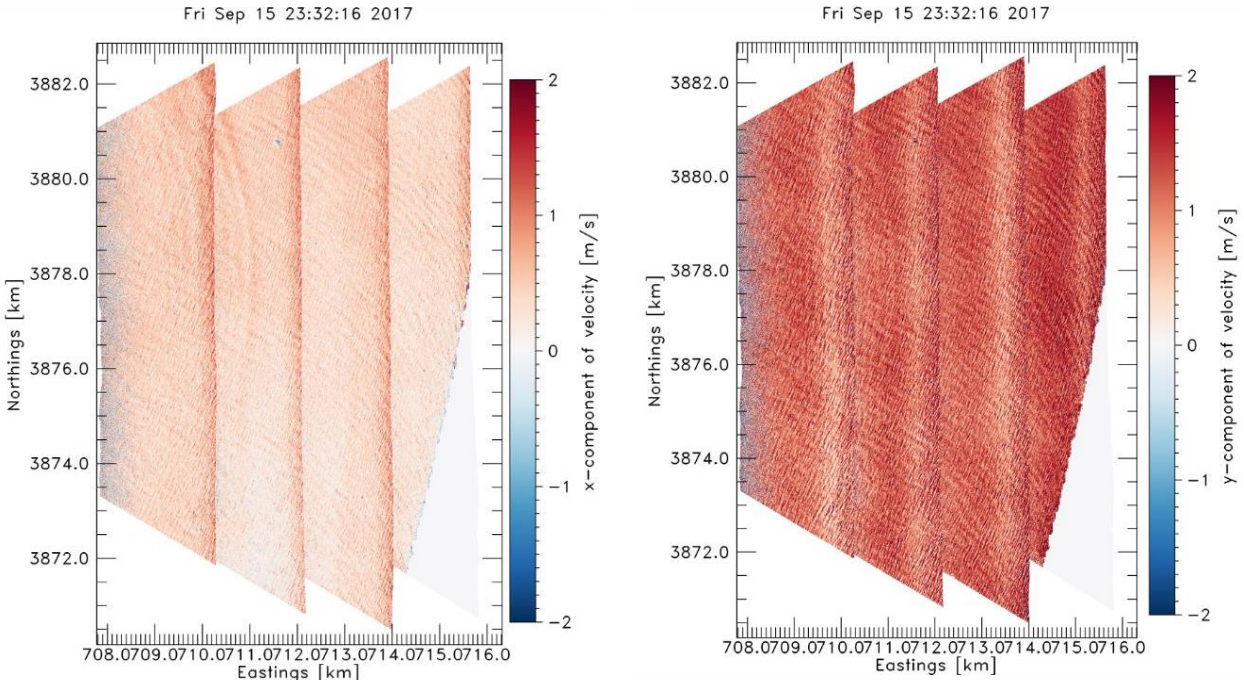

Figure 3.12. x- (left panel) and y- (right panel) components of surface current measured by ATI-SAR over Point Sal, CA during southbound flights for September 15 2017 23:32:16 GMT.

Figure 3.5 –Figure 3.8 corresponds to northbound flights and Figure 3.9 – Figure 3.12 corresponds to southbound flights. The time at the top of each velocity map shows the time of flight experiment to collect the corresponding data by ATI-SAR. These times are in GMT.

In order to present retrieved surface current components at different weather conditions (specifically different wind condition), Figure 3.13 – Figure 3.18 show the x- and y-components of surface current measured by ATI-SAR from the data collected during the flight experiment on September 16 2017 over Point Sal, CA. As presented in Table 2.3, average wind speed value during active flight hours on September 16 (4.4 m/s) is almost half of the average wind speed during September 15 (8 m/s) flight experiment. Figure 3.13 - Figure 3.15 corresponds to the northbound flights and Figure 3.16 – Figure 3.18 corresponds to the southbound flights.

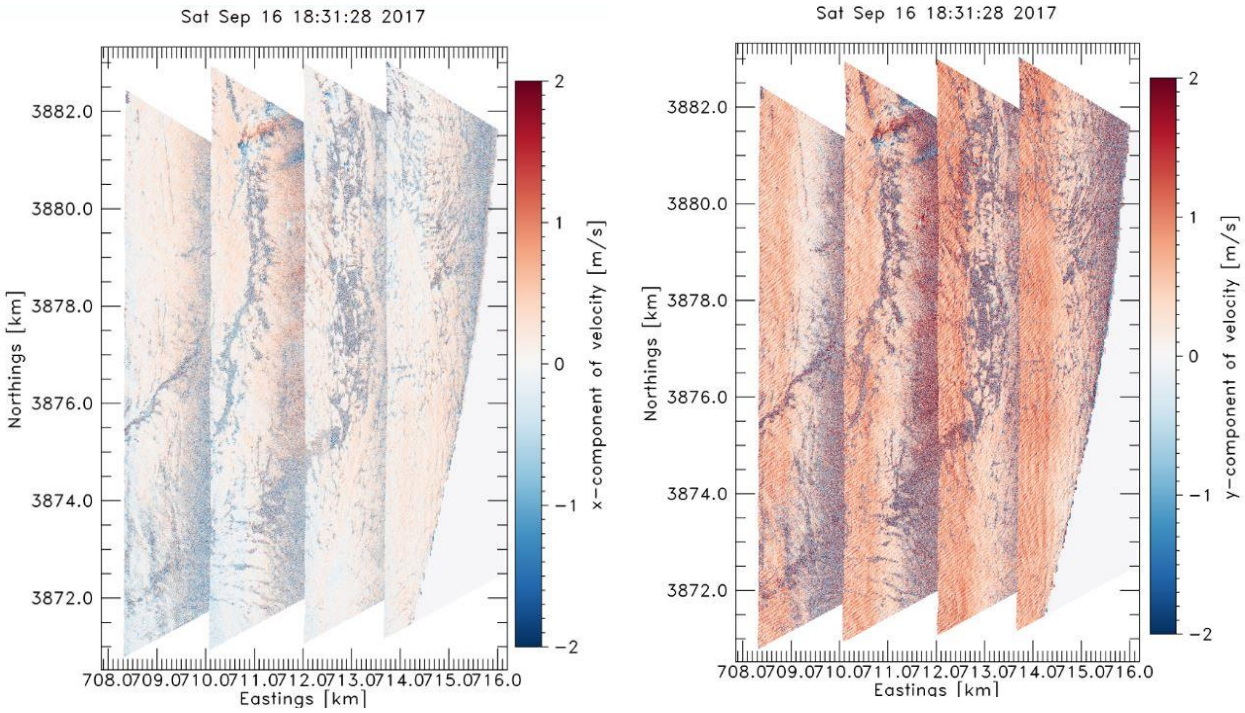

Figure 3.13. x- (left panel) and y- (right panel) components of surface current measured by ATI-SAR over Point Sal, CA during northbound flights for September 16 2017 18:31:28 GMT.

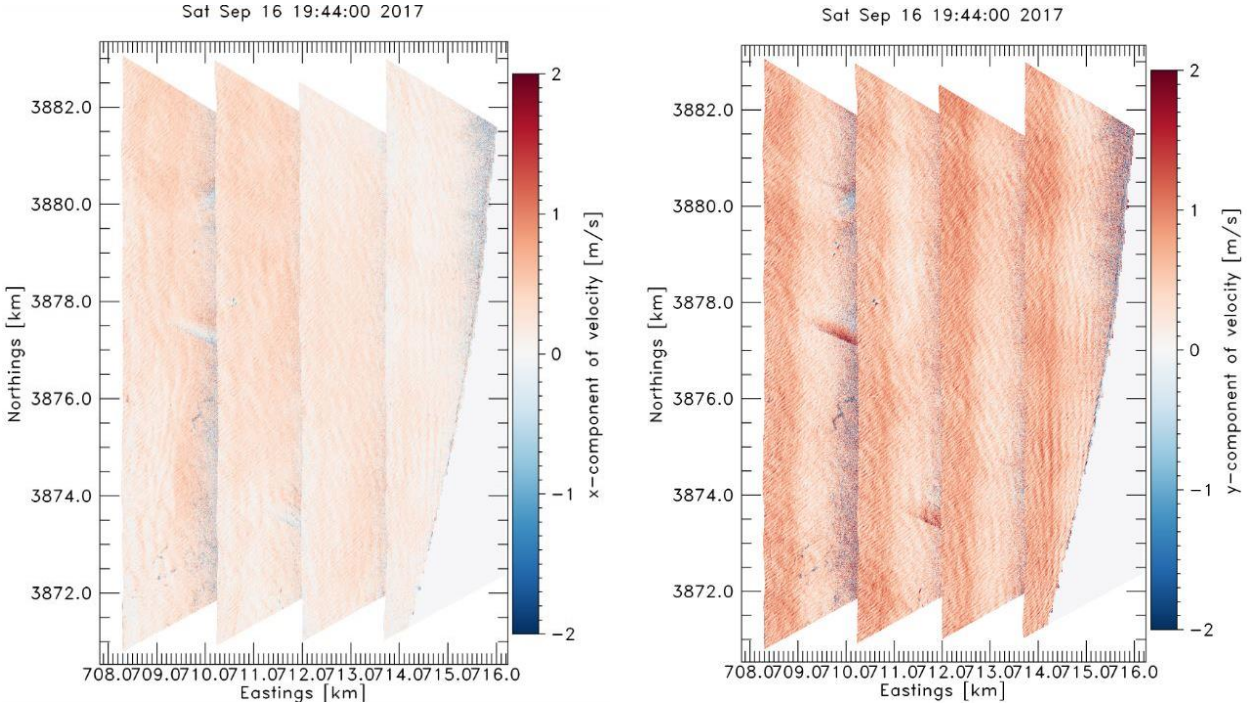

Figure 3.14. x- (left panel) and y- (right panel) components of surface current measured by ATI-SAR over Point Sal, CA during northbound flights for September 16 2017 19:44:00 GMT.

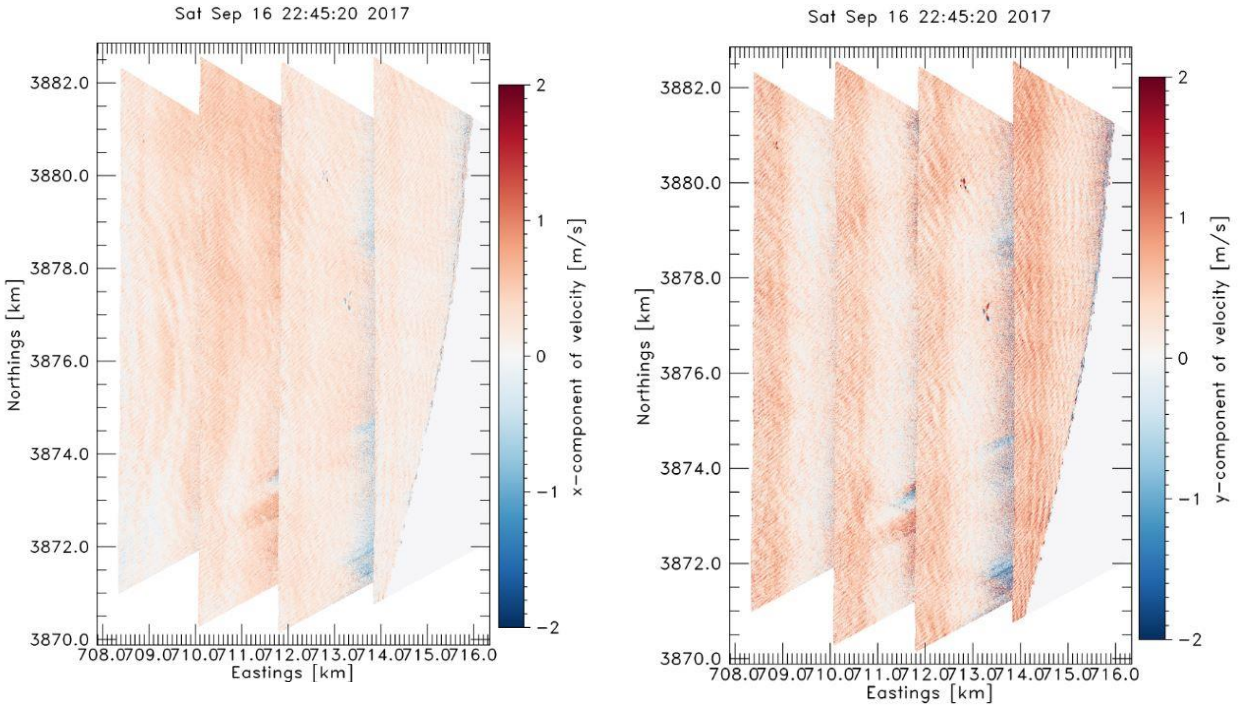

Figure 3.15. x- (left panel) and y- (right panel) components of surface current measured by ATI-SAR over Point Sal, CA during northbound flights for September 16 2017 22:45:20 GMT.

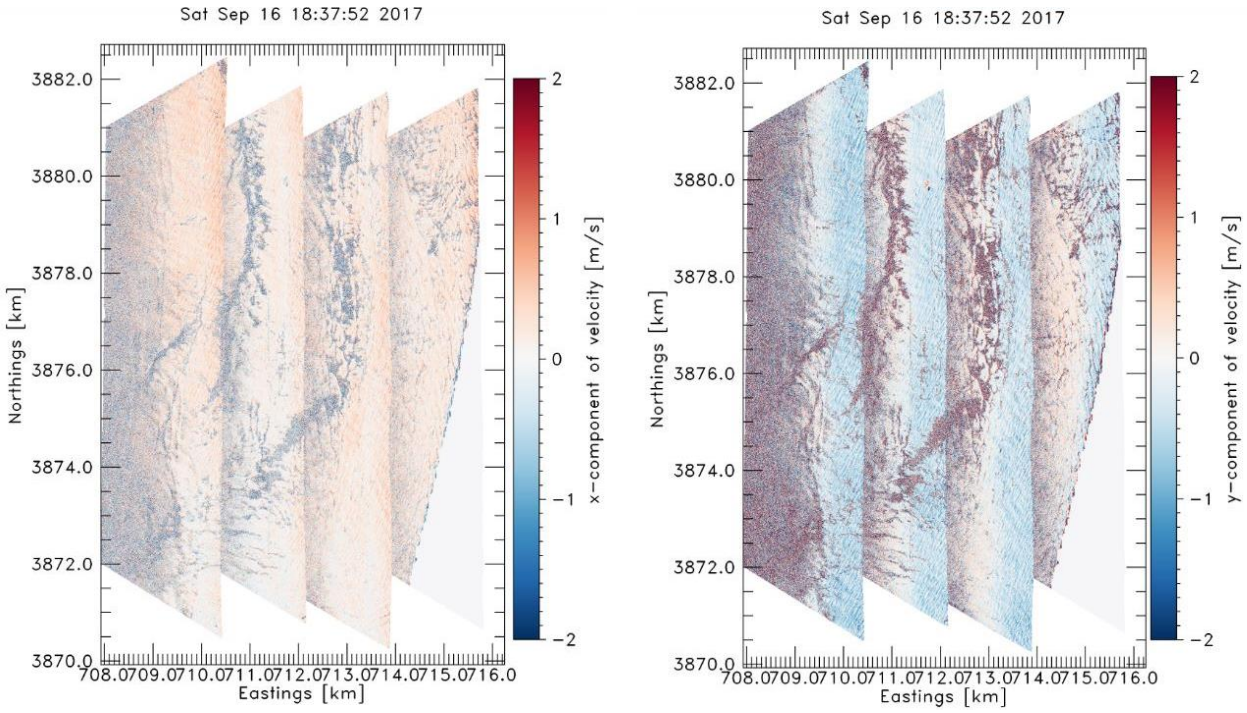

Figure 3.16. x- (left panel) and y- (right panel) components of surface current measured by ATI-SAR over Point Sal, CA during southbound flights for September 16 2017 18:37:52 GMT.

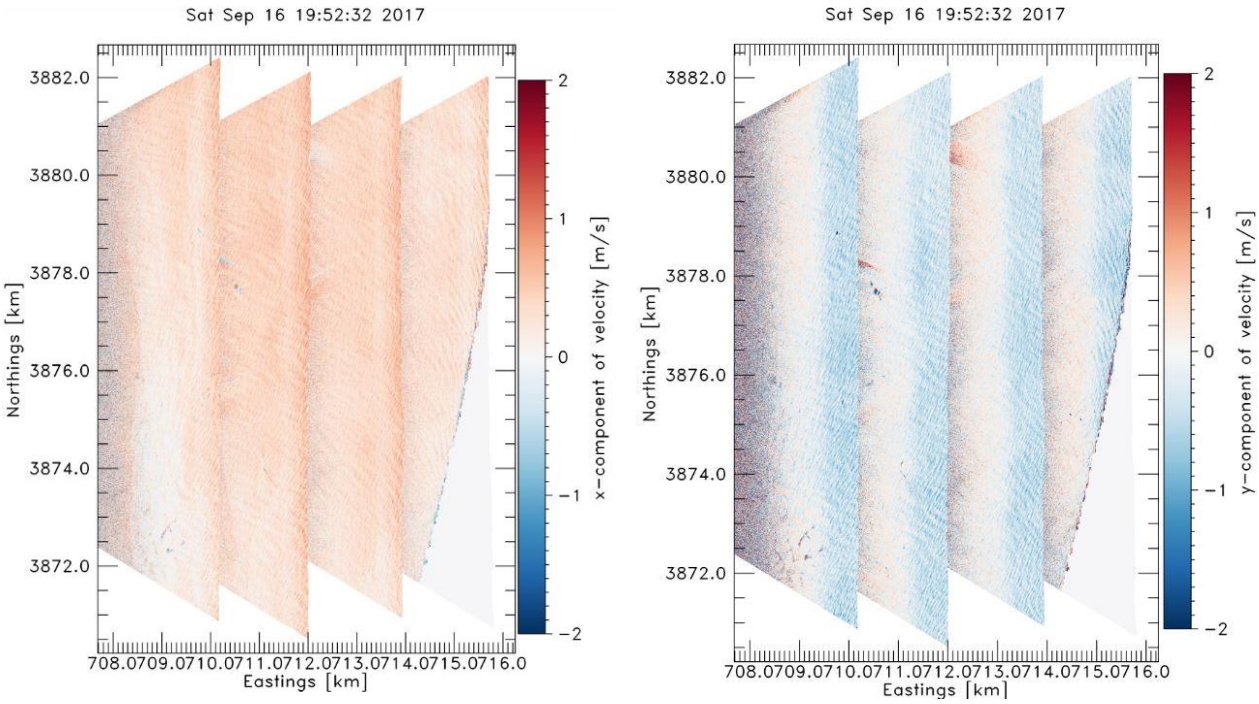

Figure 3.17. x- (left panel) and y- (right panel) components of surface current measured by ATI-SAR over Point Sal, CA during southbound flights for September 16 2017 19:52:32 GMT.

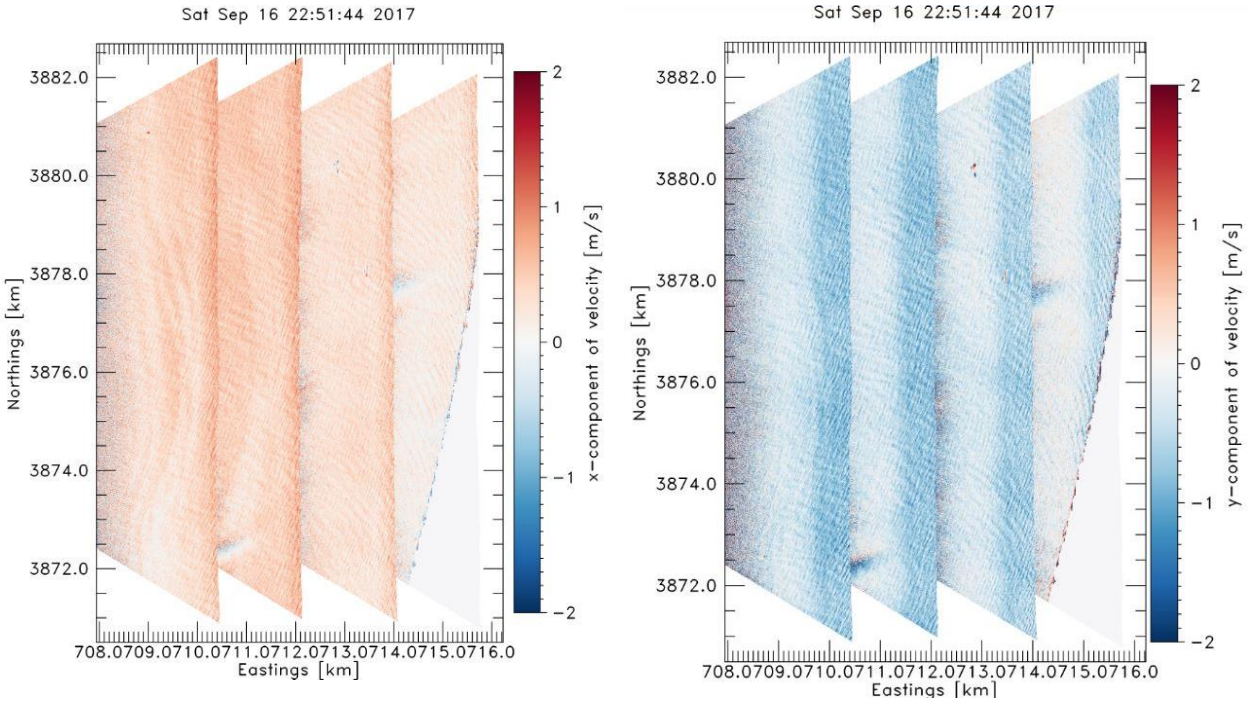

Figure 3.18. x- (left panel) and y- (right panel) components of surface current measured by ATI-SAR over Point Sal, CA during southbound flights for September 16 2017 22:51:44 GMT.

One can see that in Figure 3.13 and Figure 3.16, there are some dissonances in the retrieved surface current components. It could be because of low signal to noise ratio as a result of very low wind speed during the first hour of flight experiment on September 16th flight. Another possible reason for the mottling observed in Figure 3.13 and Figure 3.16 is accumulation of surfactants. Visual imageries during the time period for ATI-SAR data collection corresponds to Figure 3.13 and Figure 3.16 show a strong phytoplankton bloom that has large surface expression.

During the flight experiment over Point Sal, CA consecutive northbound and southbound flights occurred during one-hour time window. So it is expected to see almost the same retrieved x- and y-components of surface current from the ATI-SAR data collected during consecutive northbound and southbound flights. However, it can be observed that there are differences between the surface current components retrieved during consecutive northbound and southbound flights.

The x- and y-components of surface current are calculated form the Doppler measurements by ATI-SAR using the algorithm presented earlier this chapter. The differences are observed in the retrieved surface current components in consecutive flight tracks, which are less than an hour apart.

As discussed at the beginning of this chapter, the ATI-SAR surface current retrieval algorithm used to create surface current components' maps (Figure 3.5 - Figure 3.18) does not include removal of the contribution of the orbital velocity of the gravity waves (V_o) from the Doppler velocity ($V_{Doppler}$) measurements by the ATI-SAR. These observed differences are due to this deficiency in the retrieval algorithm. In order to resolve this issue, in chapter 5, I introduce a modification to the ATI-SAR surface current retrieval algorithm. This modification suggests

using a scattering model (M4S, which will be introduced in chapter 4) and incorporating its outputs to the retrieval algorithm in order to remove V_o as well as V_b and V_d from the measured Doppler velocity. This will result in improvement to the surface current geophysical model function.

Chapter 4. M4S MODEL AND ITS INTEGRATION TO THE SURFACE CURRENT GMF

Remote sensing techniques rely on Geophysical Model Functions (GMF) to map radar Doppler measurements to ocean surface current values. As mentioned earlier in Chapter 1, there is deficiency in ocean surface current's GMF and this research proposes a method to improve it.

To implement improvement to the surface current GMF, I use a physics-based surface scattering model (named M4S) developed by Dr. Roland Romeiser [5][6][28]. M4S is used to reproduce Doppler measurements of radar scatter from water surface, which I compared to the ATI-SAR measurements in order to validate the existing model. Afterwards, in chapter 5 I run the model and incorporate the model's outputs to the surface current GMF in order to improve the retrieval algorithm for ATI-SAR surface current measurements.

Eventually in chapter 6 modification to M4S model is proposed and M4S is run with the modification. The model's outputs after applying the modification are inserted to the surface current geophysical retrieval algorithm and the results are presented.

4.1 INTRODUCTION TO M4S MODEL

M4S is a tool for numerical simulations of microwave radar imaging of surface current features and of wind features near ocean surface. M4S has been developed for the purpose of testing and validating existing and new theories of various aspects of radar imaging mechanism. The model outputs are utilized to explain and interpret observed radar signatures and make predictions about radar signatures of hypothesized current and wind phenomena or signatures of known phenomena to be imaged by existing or hypothesized radar configurations [31].

The development of the model started in 1991, when a simple one-dimensional version of the equations of weak hydrodynamic interaction theory [32] was implemented in combination with a simple composite surface scattering model [33][34]. Then, in 1994 and 1995, the capability to compute Doppler spectra and ATI-SAR phase differences was added to the model.

This Doppler model was developed based on an extension of the composite surface scattering model concept, which derives all relevant parameters such as mean Doppler offset and Doppler bandwidth from a given surface wave spectrum and given radar parameters [28]. The version which used in this research is M4S 3.2.0 and it represents the state of the art as of Spring 2008.

4.1.1 *M4S inputs requirements and initialization*

The M4S model is initialized with input current and wind speed data. These are the two mandatory input fields to the model. There are other optional inputs such as bathymetry and surface elevation. For all the simulations performed in this research, only the two mandatory inputs of surface current and wind are used to run M4S model.

In order to run the model, the current and wind fields should be gridded first. The grids must be rectangular with constant spacing in each direction but not necessarily the same spacing in both directions. The grid spacing (Δx or Δy) must be between 0.01 m and 1000 m and the ratio between grid spacing in x and y direction must be between 0.1 and 10. The input fields should also have x and y position of the grid points in meters with the convention of the lowest value indicating the lower left corner of the rectangular grid. Figure 4.1 shows a simplified illustration for M4S inputs gridding order convention. The rectangular grid has "*r*" rows and "*c*" columns. The numbers in green represent the ordering and the numbers in black inside the brackets

represent the location of the grids in meters in *x* and *y* direction. Both input current and wind fields should be gridded with the exact same spacing.

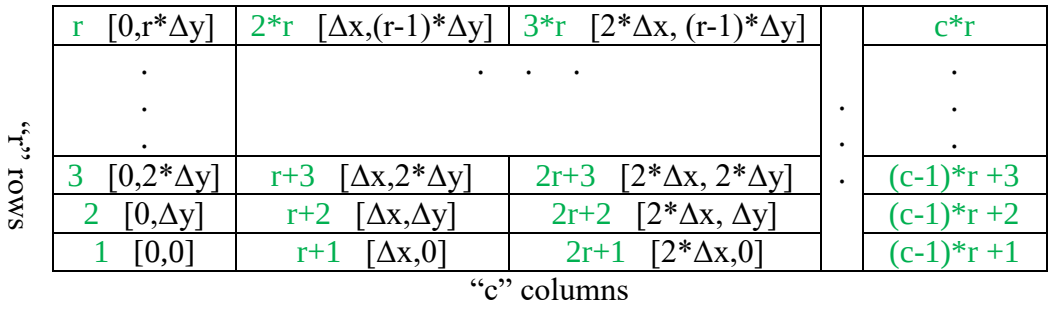

Figure 4.1. Illustration of grid spacing for input current and wind fields to M4S model.

M4S has a capability to be run in different modes such as ATI-SAR mode or Doppler mode. Based on the mode, M4S can generate various types of outputs. When running the model to compute radar signatures there are a few parameters should be specified. Radar frequency, polarization, incidence angle, look direction, platform altitude, platform velocity, platform heading and along-track or cross-track baseline are among required parameters to specify when running M4S. Figure 4.2 illustrates the required input data to run M4S model and a few examples of parameters that M4S can produce.

In this research, the input current and wind filed required to run M4S model over MCR is provided by Center for Coastal Margin Observation and Prediction (CMOP). These data are generated using a Semi-implicit Eulerian-Lagrangian Finite Element (SELFE) model for cross scale ocean circulation [35]. Also the required current and wind fields to run the model over Point Sal, CA is extracted from Regional Ocean Modeling System (ROMS) data. Georgia Tech University and the Scripps Institute of Oceanography developed a nested numerical model, which produces current and wind fields for the area including Point Sal, CA [36].

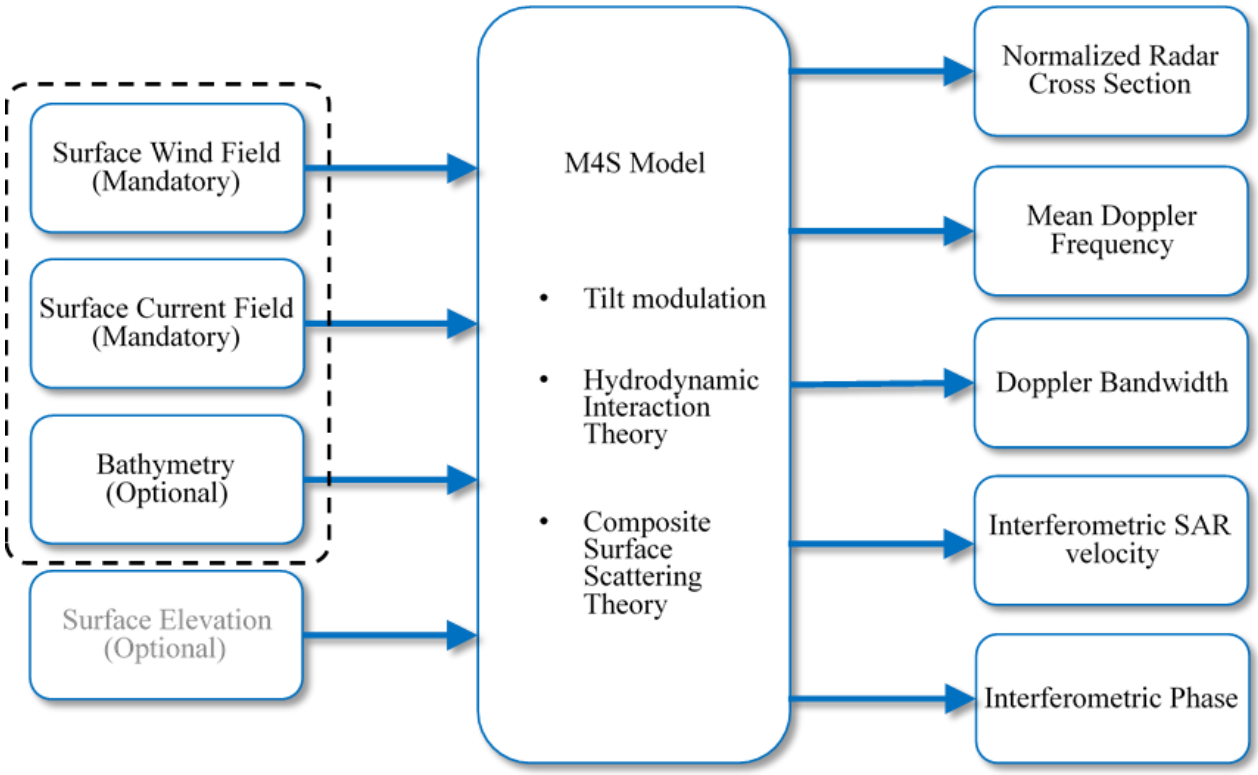

Figure 4.2. Schematic M4S model with input and output parameters.

4.2 M4S MODEL RESULTS AT C-BAND OVER MCR

M4S can be run with the specific radar and geometry specifications for each scenario and the model's outputs are generated at each frequency exclusively. In order to run M4S over Columbia River mouth the model was initiated with input current and wind fields provided by CMOP. Figure 4.3 and Figure 4.4 show x- and y-components of CMOP current and wind fields over Columbia River mouth, respectively.

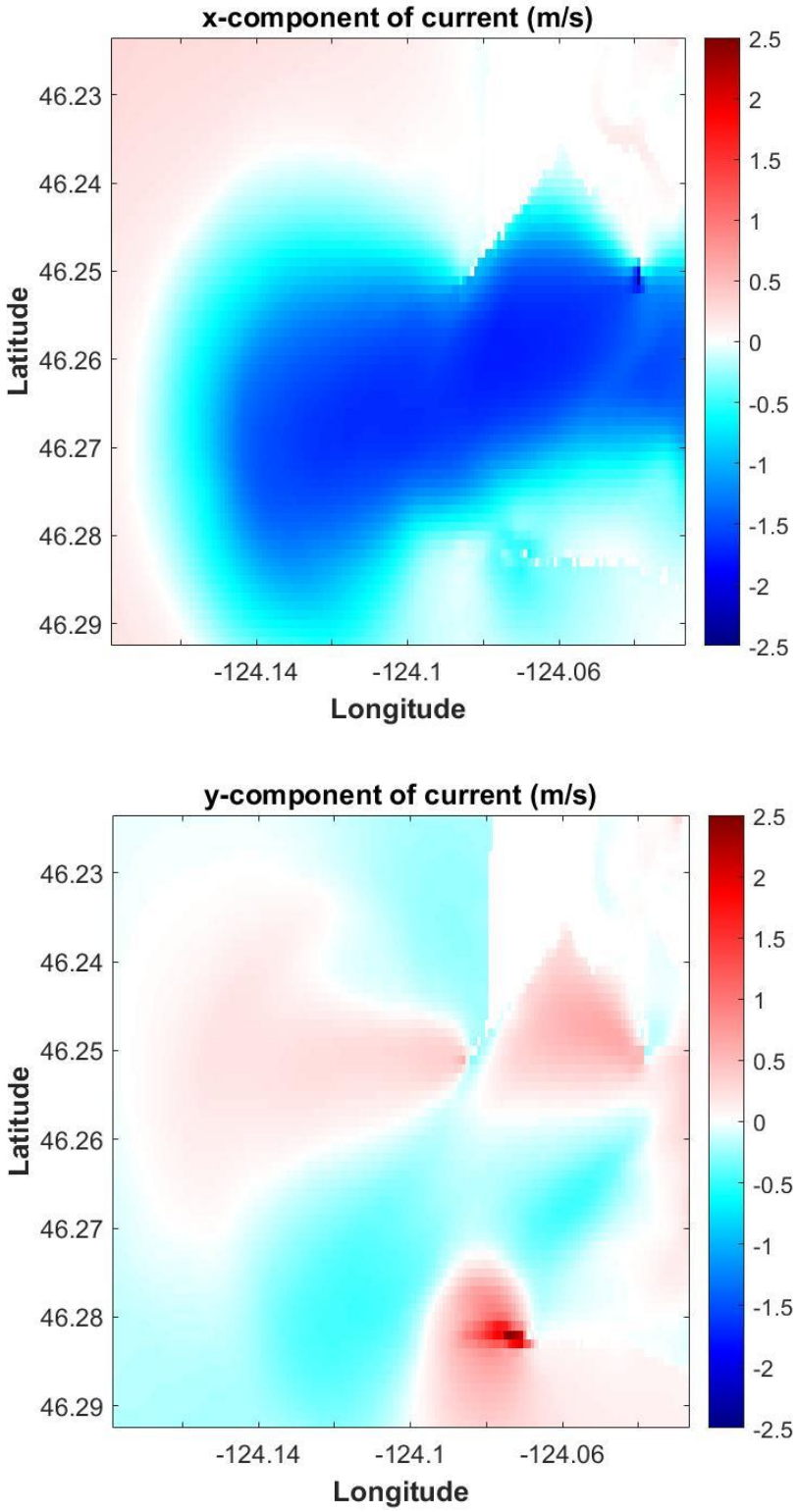

Figure 4.3. x (east)- and y (north)-components of CMOP surface current field input to M4S over Columbia River mouth.

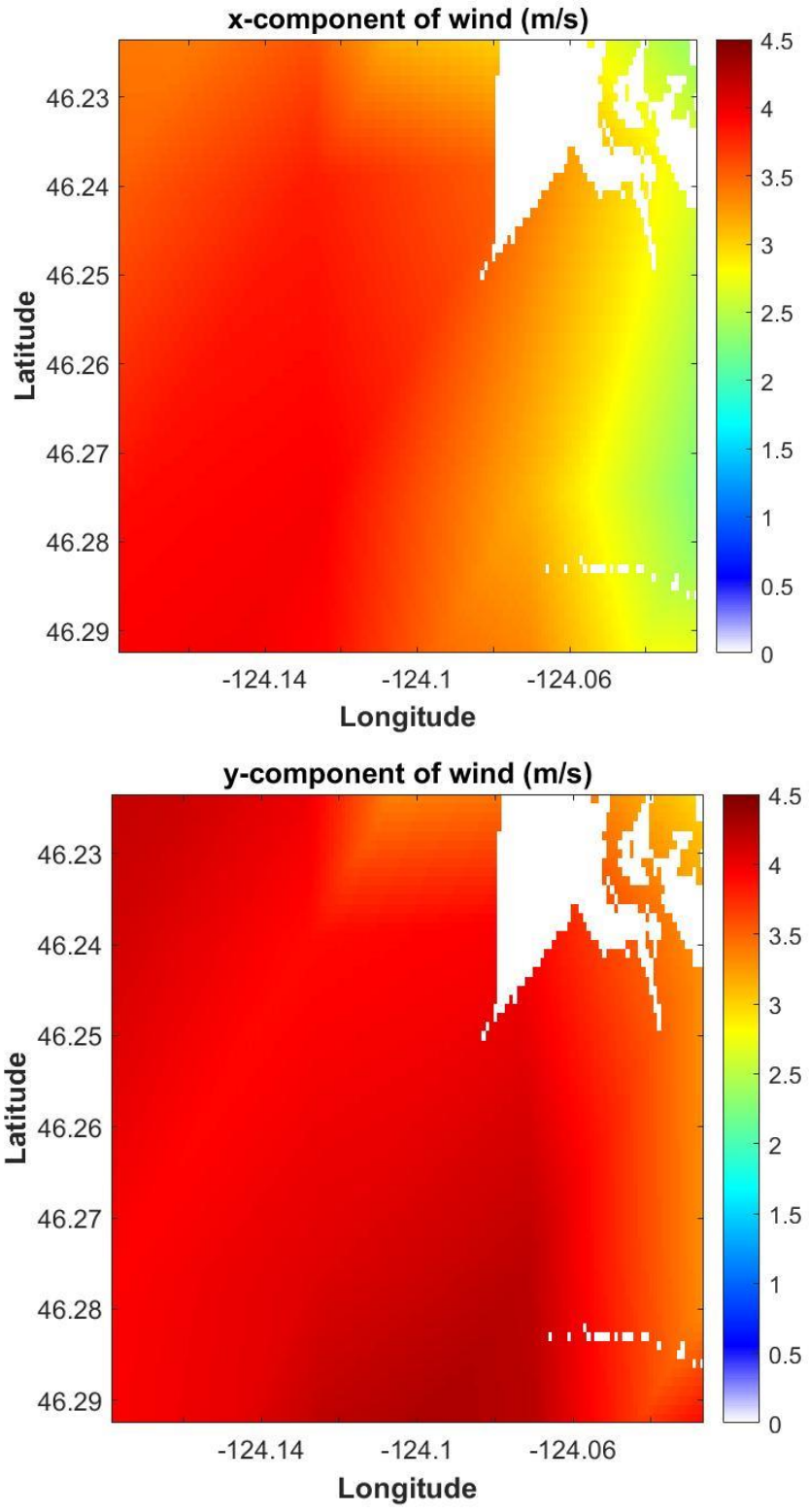

Figure 4.4. x (east)- and y (north)-components of CMOP wind field input to M4S over Columbia River mouth.

The grid spacing in the x and y directions are approximately 77 m and 111 m, respectively. The radar geometry and flight specifications are set similar to the flight experiment performed to collect the data to generate surface velocity maps retrieved by the APL ATI-SAR presented in Figure 3.2 and Figure 3.3.

The model is run and Figure 4.5 shows M4S computed InSAR velocity at C-band over MCR for forward-looking direction (top panel) and aft-looking direction (bottom panel). Black solid lines show the aircraft heading direction and the dashed lines show the ATI-SAR look directions. The color shows M4S computed radial InSAR velocity in m/s, which varies over a range of ±2 m/s. As depicted in Figure 4.5 forward-looking radial velocities have negative values (blue color) and aft-looking radial velocities have positive values (red color) over MCR similar to radial velocities retrieved by ATI-SAR presented in Figure 3.2.

4.2.1 *Comparison between measurements and M4S outputs over MCR*

Radial velocity measurements by ATI-SAR at C-band over MCR were presented in Figure 3.2 and Figure 3.3. M4S model was also initiated with CMOP surface current and wind fields and was run at corresponding frequencies and geometry specifications. To initiate M4S simulations I set look directions the same as the ATI-SAR look directions in Figure 3.2 and Figure 3.3. Platform and geometry specifications are also chosen based on the ATI-SAR flight experiments.

The model's outputs are also presented in Figure 4.5. Radial velocity measurements at C-band by the APL ATI-SAR and M4S output InSAR radial velocity show similar features over MCR. To make a closer comparison between the measured radial velocity at C-band by the ATI-SAR with M4S computed InSAR velocity, scatterplots of those velocities are presented in Figure 4.6.

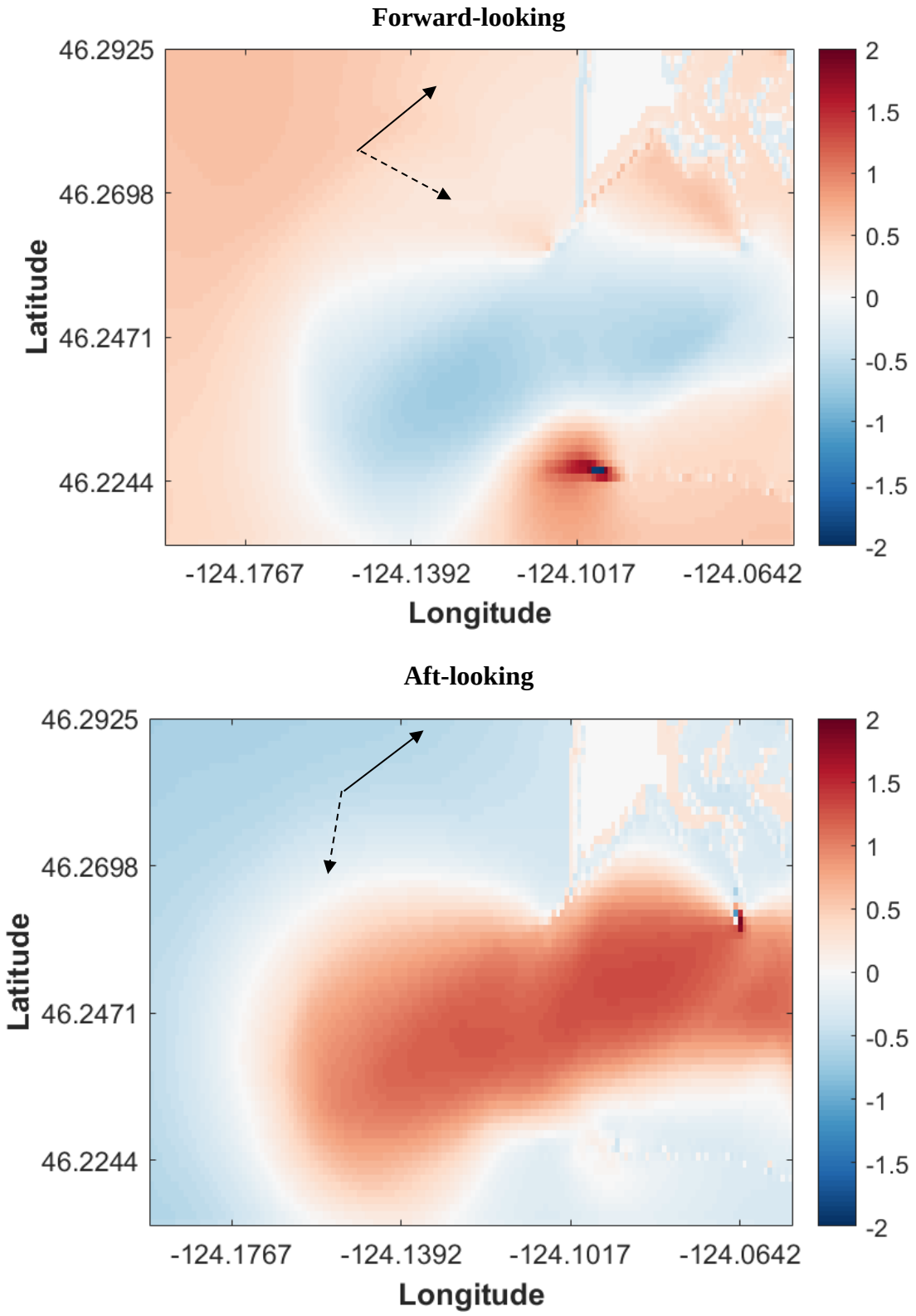

Figure 4.5. M4S computed InSAR velocity [m/s] over Columbia River Mouth for forward-looking (top panel) and aft-looking (bottom panel) directions. They correspond to the measurements presented in Figure 3.2 and Figure 3.3.

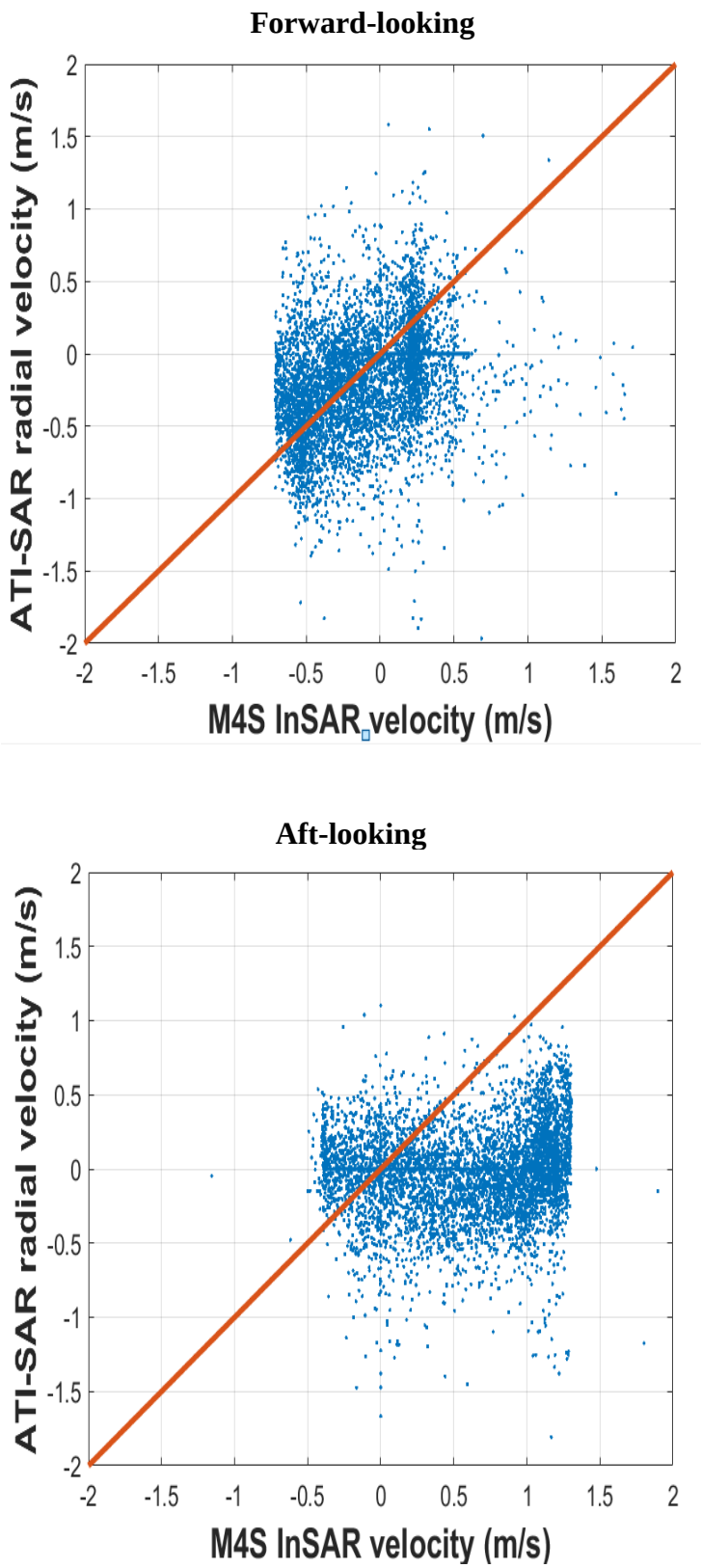

Figure 4.6. Scatterplots of M4S computed InSAR velocity and ATI-SAR radial velocity measurements at C-band for forward-looking (top pamel) and aft-looking (bottom panel).

It can be observed for forward-looking case (top panel) the points are more clustered around the 45-degree line. Also for radial velocity with higher magnitude (±0.5 m/s) the scatter points are more clustered to a 45-degree line compared to the scatter points at velocities close to zero. This can be either M4S model's error or the instrument's error at very low surface velocity values.

There are several possible reasons to explain the differences observed between ATI-SAR measurements and M4S model output. For instance, there is a requirement to run M4S simulations, which dictates that the radar look direction and the radar platform heading should be perpendicular. However, as described in chapter 2 the APL ATI-SAR system has two squinted radar looks (forward- and aft-looking directions). Therefore, in order to be able to run M4S for corresponding ATI-SAR experiment, I initiate M4S with the actual radar look directions and set the radar platform headings normal to the look directions. This means there are differences between the actual radar platform heading directions and the ones used to initiate M4S model to create the radial InSAR velocities presented in Figure 4.5.

Another possible reason for the differences between the measured radial velocities by APL ATI-SAR at C-band and the M4S results is the difference between the actual wave spectrum present at the scene during the corresponding experiment and the estimated wave spectrum by M4S from input wind field. This will be discussed in more details in subsequent chapters.

4.3 M4S MODEL RESULTS AT C-BAND OVER POINT SAL, CA

In order to run M4S over Point Sal, CA, the model is initiated with input current and wind fields from ROMS data. Figure 4.7 and Figure 4.8 show x- and y-components of ROMS current and wind fields, respectively. The resolution of these ROMS products is 66 m and is for the day of September 15, 2017 during Point Sal, CAL experiment.

To run the model, the radar geometry and flight specifications are set similar to the flight experiment performed to collect the data to generate surface current components retrieved by APL ATI-SAR presented in Figure 3.5 – Figure 3.12.

Figure 4.9 shows M4S computed InSAR velocity over Point Sal, CA. I ran the M4S model for four different configurations based on aircraft headings and the directions in which the radar antennas look at the scene, and computed InSAR velocity output of M4S model for these four different cases are presented in Figure 4.9.

The left column shows the computed velocity for the case in which the aircraft is flying northward and the right column shows the computed InSAR velocity when aircraft is heading southward. The top panels corresponds to the forward-looking cases and the bottom panels correspond to the aft-looking cases. Black straight arrows on top of the velocity maps represent the aircraft flight direction and dashed arrows show the direction in which the ATI-SAR antennas look at the scene.

M4S computed InSAR velocities presented in Figure 4.9 are radial velocities. Therefore, for each case presented in Figure 4.9, positive radial velocities (red colour) is in the same direction as radar look direction (dashed-line arrows) corresponds to that specific case, and negative radial velocities (blue colour) is in the opposite direction of the radar look direction.

In each row of Figure 4.9, the radar look directions for the northbound flight (left column) and the southbound flight (right column) are in opposite directions. So one can conclude that the negative and positive radial velocities presented at each row of Figure 4.9, do not have the same actual physical meaning.

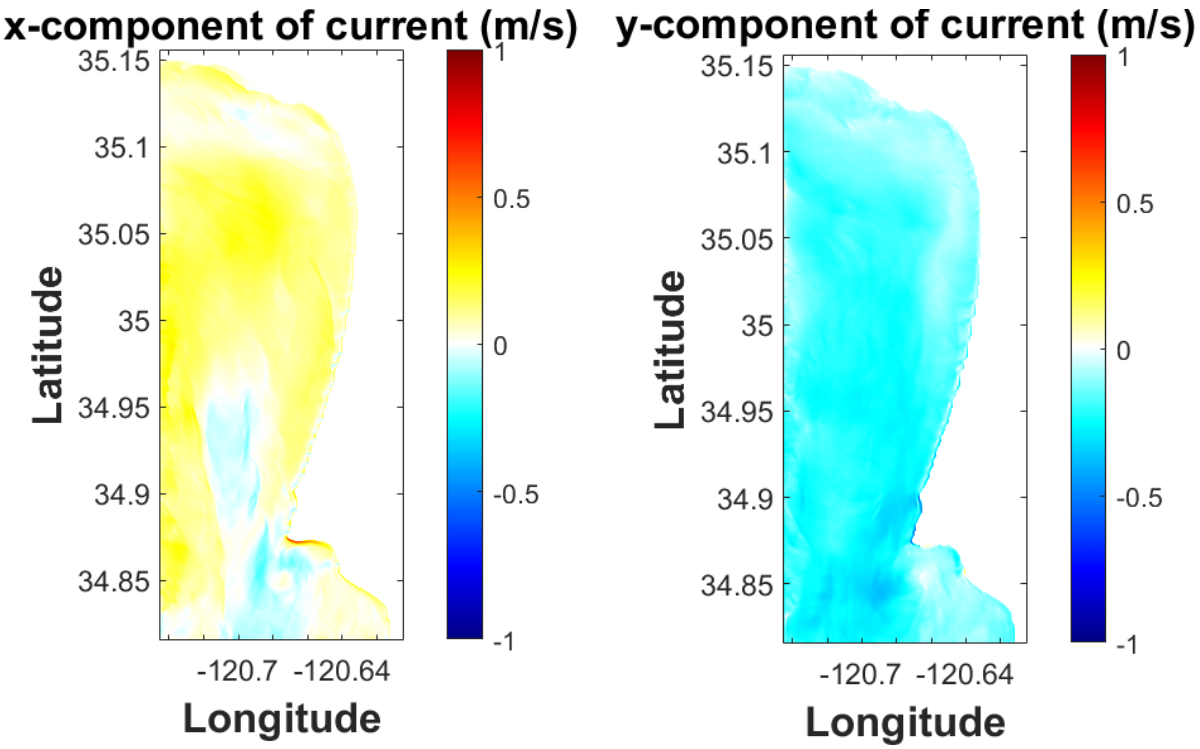

Figure 4.7. x (east) - and y (north)-components of ROMS surface current field input to M4S.

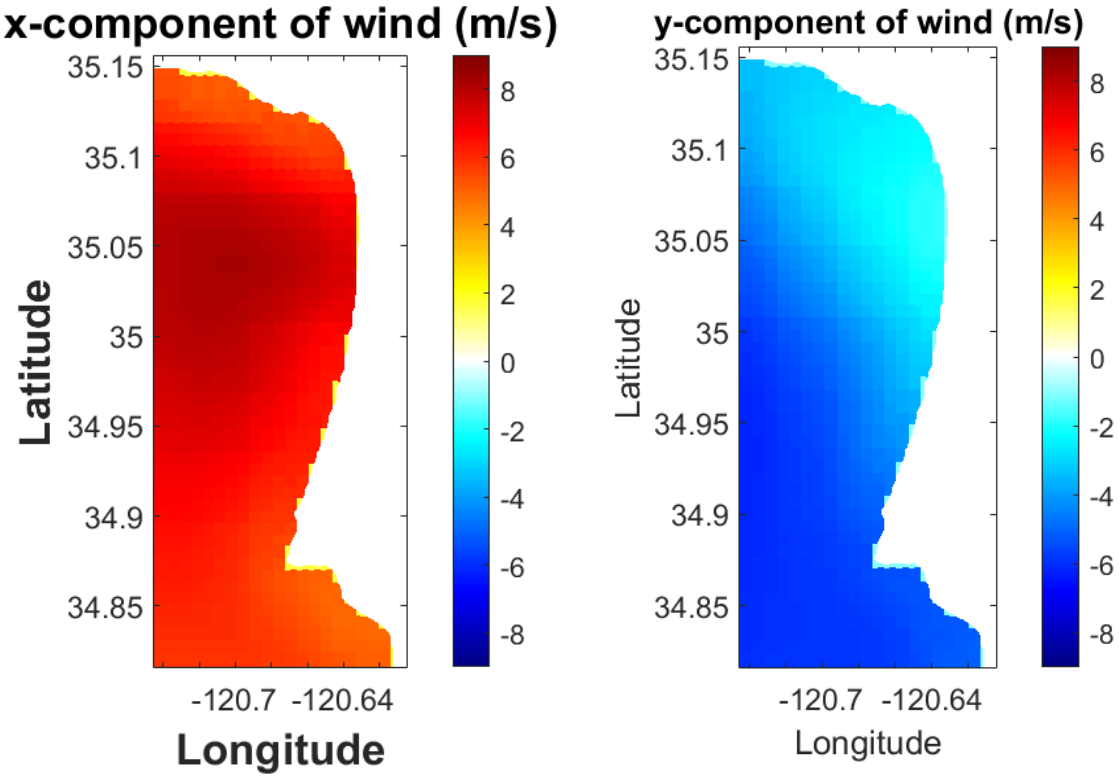

Figure 4.8. x (east)- and y (north)-components of ROMS wind field input to M4S.

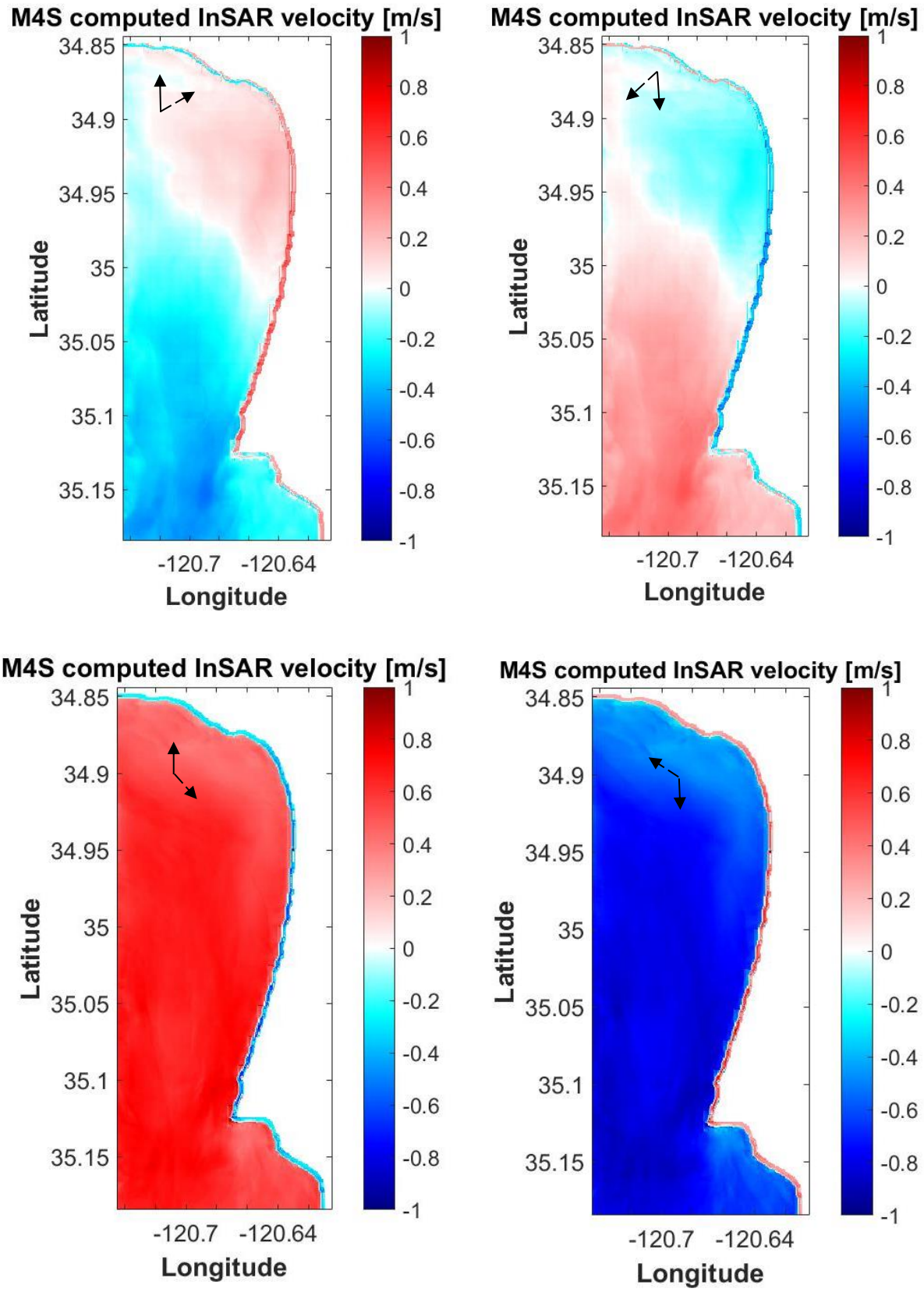

Figure 4.9. M4S computed InSAR velocity [m/s] over Point Sal, CA.

Therefore, in order to overcome the ambiguity I reverse the colour bar for the southbound flight and present the same M4S computed InSAR velocities in Figure 4.10 with the reversed colour bar. It can be seen that regardless of flight heading and radar look direction M4S computed InSAR velocities show similar features over Point Sal, CA.

Computed InSAR velocity presented in upper row of Figure 4.9 and Figure 4.10 (forward-looking cases) has northeast direction in the northern part of the area and southwest direction in the lower altitudes. On the other hand, computed InSAR velocity presented in lower row of Figure 4.9 and Figure 4.10 (aft-looking cases) has southeast direction all over the area.

In the next chapters, I describe how I use M4S output (InSAR radial velocity) and insert it to the ATI-SAR surface current retrieval algorithm in order to improve the surface current geophysical model function. Improvement to M4S model will also be proposed and the ATI-SAR retrieved surface current after applying the modification to M4S model will be presented in chapter 6.

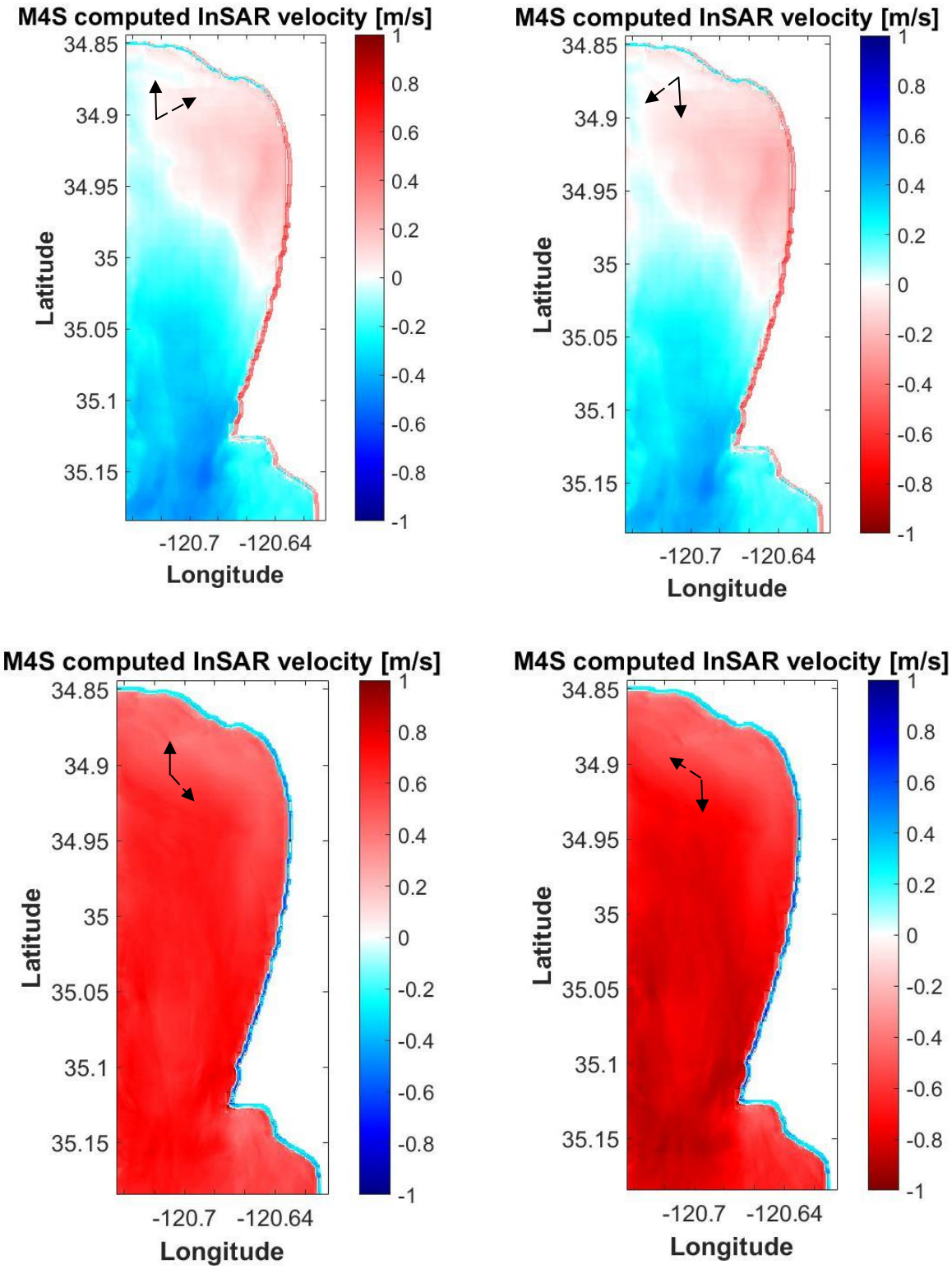

Figure 4.10. M4S computed InSAR velocity [m/s] over Point Sal, CA with reversed colour bar for the southbound flight.

Chapter 5. WAVE-DEPENDENT DIRECTIONAL BIASES IN OCEAN SURFACE CURRENT ESTIMATION

ATI-SAR is a remote sensing technique intended for measuring surface currents. The current vector measurements are biased by the presence of surface winds and waves, so their effects must be accommodated in order to yield accurate currents estimates using ATI-SAR [37]. As presented in chapter 3, there are biases to the retrieved surface current components by APL ATI-SAR and it was shown in [27] that these biases are due to the contribution of the orbital velocity of the gravity waves (V_o) to the measured Doppler velocity ($V_{Doppler}$) by the ATI-SAR (equation (3.3)).

In this chapter, I present wave-dependent directional biases observed in ocean surface currents estimated by APL ATI-SAR. Then, in order to modify the retrieval algorithm and include V_o contribution to Doppler measurements as well as V_b and V_d contribution, I run the M4S model with zero-current input and wind field. I calculate the radial InSAR velocity for different cases corresponds to the ATI-SAR platform heading directions and radar look directions during the field experiment to collect ATI-SAR data.

Afterwards, I subtract the radial InSAR velocity (output of M4S model with zero-current initiation) from the ATI-SAR Doppler velocity. The resulted radial velocity incudes the contribution from surface current, exclusively. The x- and y-components of the surface current are calculated from the forward- and aft-squinted radial velocities.

Biases are still observed in the components of the surface current retrieved by ATI-SAR during successive northbound and southbound flights. I suggest that the error is due to the difference between the wave spectrum of the actual waves present in the field during the

experiment and those computed from the local wind fields by M4S [28]. I will apply wave spectrum modification to M4S model and results will be presented in chapter 6.

5.1 M4S COMPUTED INSAR VELOCITY WITH ZERO-CURRENT INPUT

In order to accommodate wind and wave effects upon the surface current retrieval algorithm I run M4S model and insert the model outputs to the retrieval algorithm. To present the wave-dependent directional biases, I initiate M4S model with zero-current field (for the whole area north of Point Sal, CA) and ROMS wind field in order to calculate radial InSAR velocity. The grid spacing in the x and y directions are approximately 66 m and 80 m, respectively. I run the M4S model for four different configurations based on aircraft headings and the directions in which the radar antennas look at the scene. Figure 5.1 shows the computed InSAR velocity output of M4S model for the four different cases of aircraft heading and radar look direction.

The left column shows the computed radial velocity for the case the aircraft is flying towards north and the right column shows the computed InSAR velocity when aircraft is heading towards south. The top panels correspond to forward-looking cases and the bottom panels correspond to aft-looking cases. Black straight arrows on top of the velocity maps represent the aircraft flight direction and dashed arrows show the direction in which the ATI-SAR antennas look at the scene.

Similar to the nonzero-current M4S simulation results (presented in Figure 4.9 and Figure 4.10) in order to have easier visual comparison between the computed InSAR radial velocities over Point Sal, CA during northbound and southbound flights the color bar should be reversed for southbound flights. I regenerate M4S InSAR radial velocity maps (for zero-current input case) with the reversed color bar for the southbound flight and the results are presented in Figure 5.2.

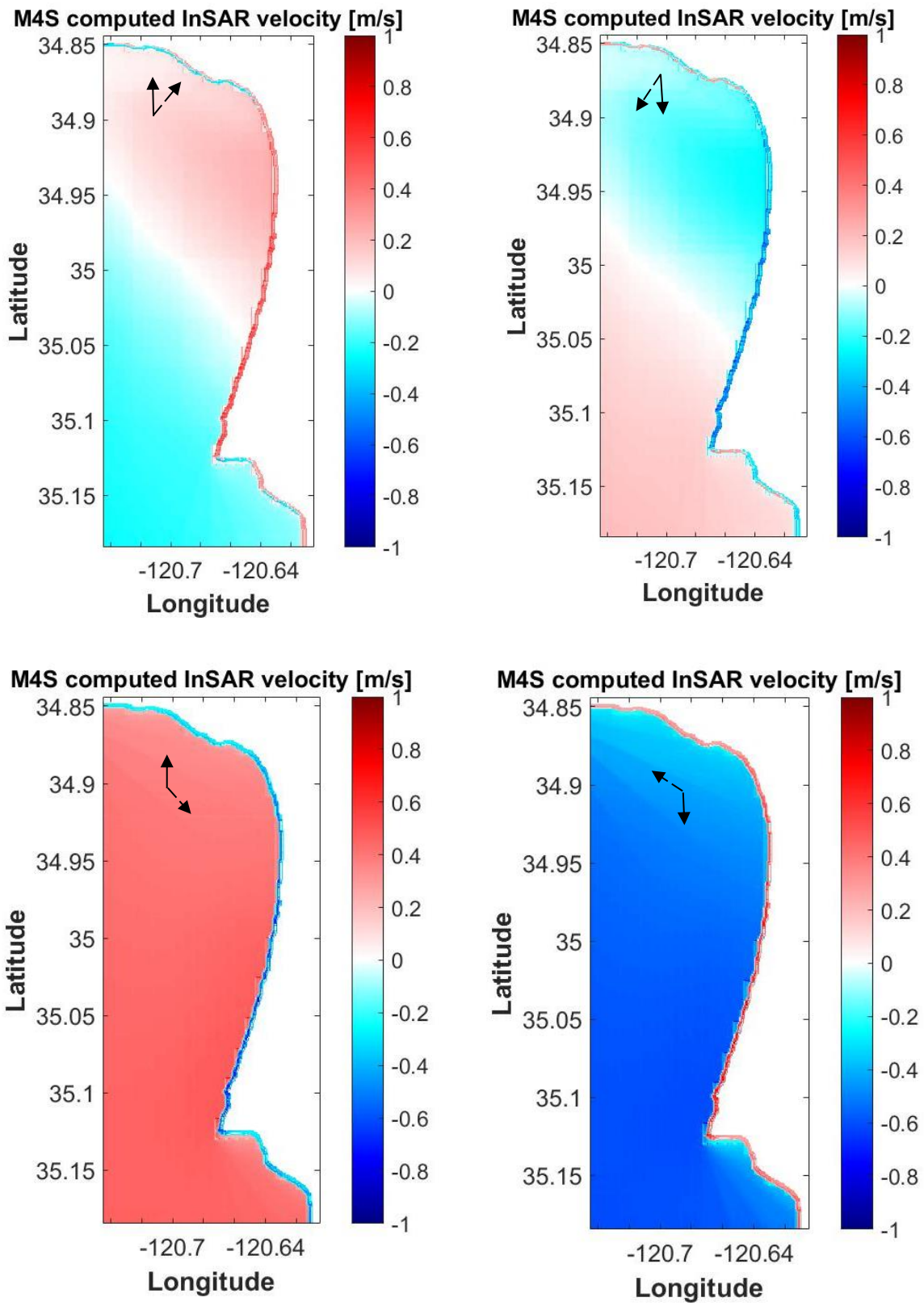

Figure 5.1. M4S computed InSAR velocity [m/s] over Point Sal, CA with zero-current input field.

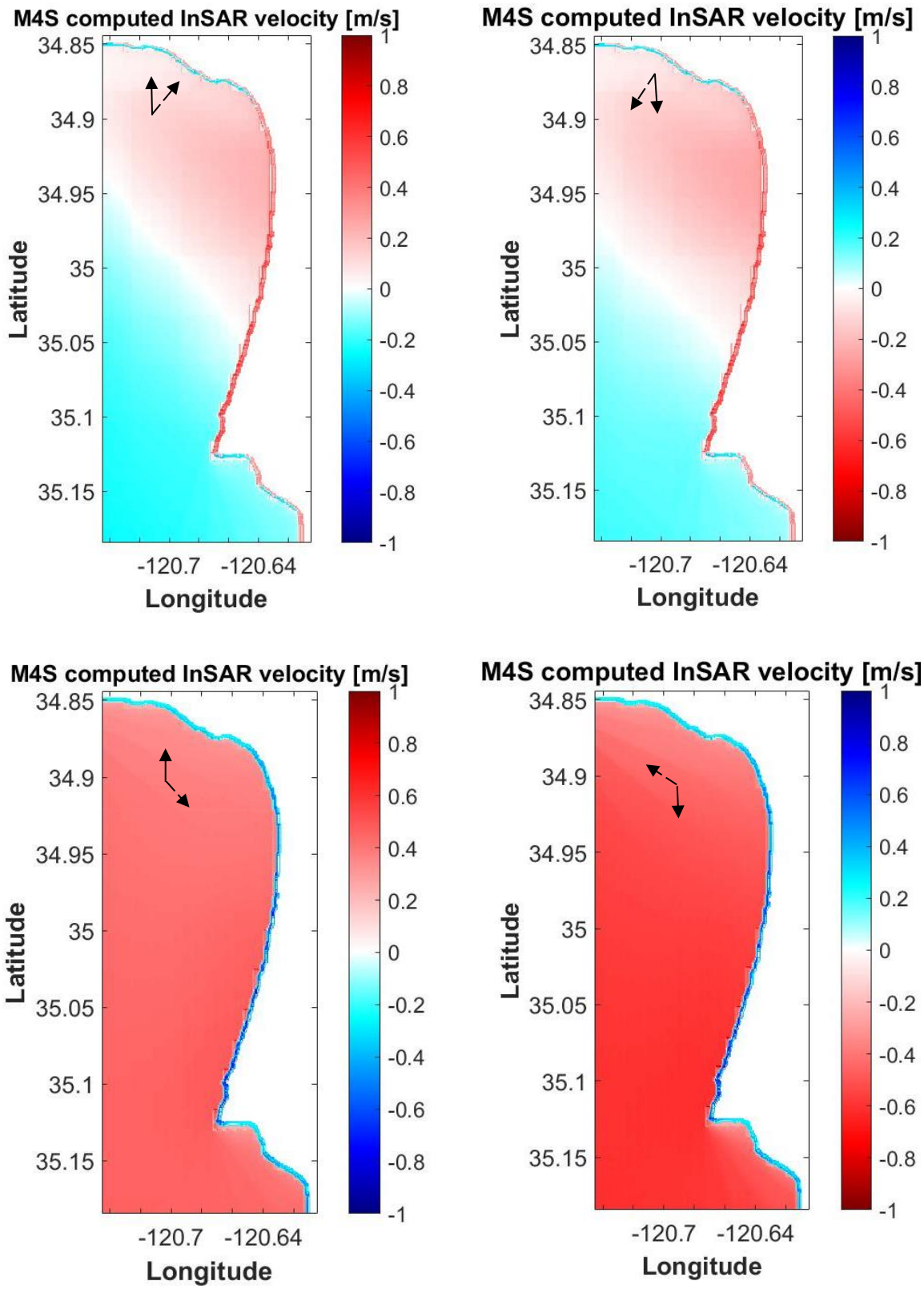

Figure 5.2. M4S computed InSAR velocity [m/s] over Point Sal, CA with zero-current input field and reversed colour bar for the southbound flight.

Next, the radial velocity calculated by the M4S model (with zero-current input) is subtracted from the measured ATI-SAR Doppler velocity such that the resulting ATI-SAR radial velocity is representative of the surface current, exclusively.

Now the resulting ATI-SAR radial velocity does not include any other contributions (V_b, V_d and V_o) presented in equation (3.3) but the contribution from surface currents. After applying this modification to the surface current retrieval algorithm, the x- (east) and y- (north) components of surface current are computed from the forward- and aft-looking radial velocities and the results are presented in Figure 5.3 and Figure 5.4, respectively. To be able to present the velocity components over larger area I merge measurements for four successive flight tracks together. The left panel corresponds to data collected when aircraft was flying northbound and looking eastward and the right panel corresponds to the case aircraft was flying southbound and looking westward.

All the ATI-SAR data used to create surface current components maps presented in Figure 5.3 and Figure 5.4 was collected within a period of one hour. Therefore, one expects the calculated surface current components to be roughly equal. However, it can be seen in Figure 5.3 and Figure 5.4 that the velocity components calculated from data collected during southbound flight (right panels) are biased towards positive values compared with the measured velocity components during northbound flights (left panels).

Figure 5.5 and Figure 5.6 show the histograms of differences between the retrieved surface current components from data collected during northbound flights and southbound flights for x- and y- components, respectively. As presented for both surface components there are differences between the ATI-SAR retrieved surface current with larger differences in the y-component.

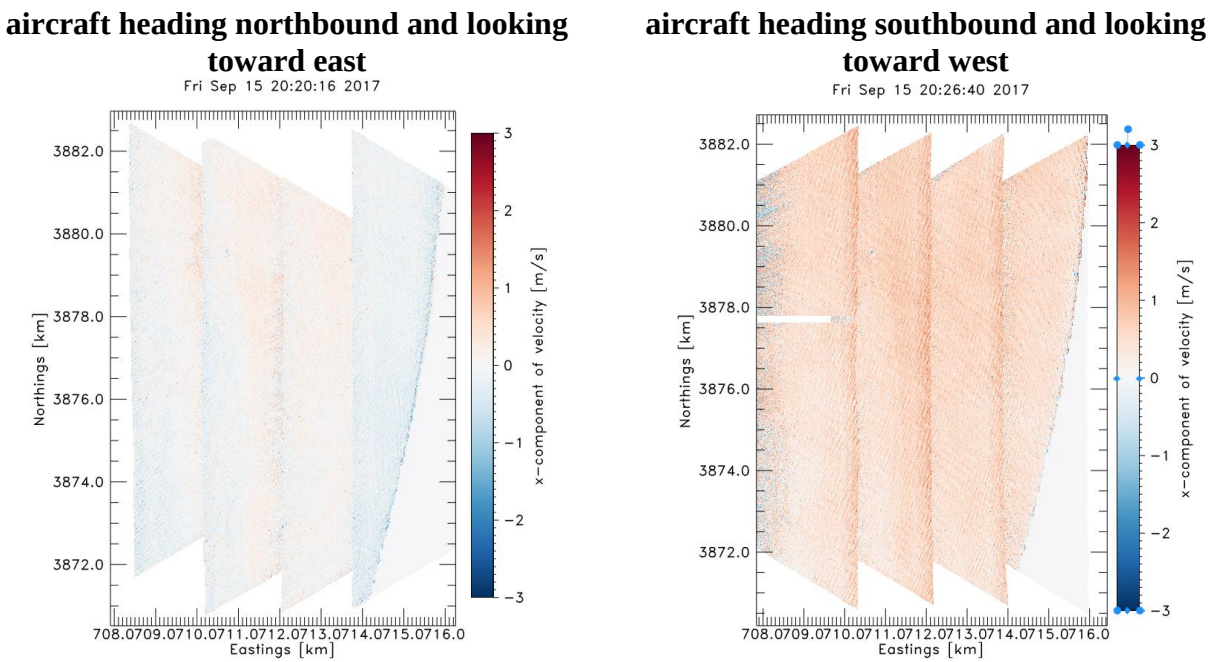

Figure 5.3. x-components of surface current computed from ATI-SAR measurements after subtracting M4S computed InSAR velocities (with zero-current input) from ATI-SAR radial velocities.

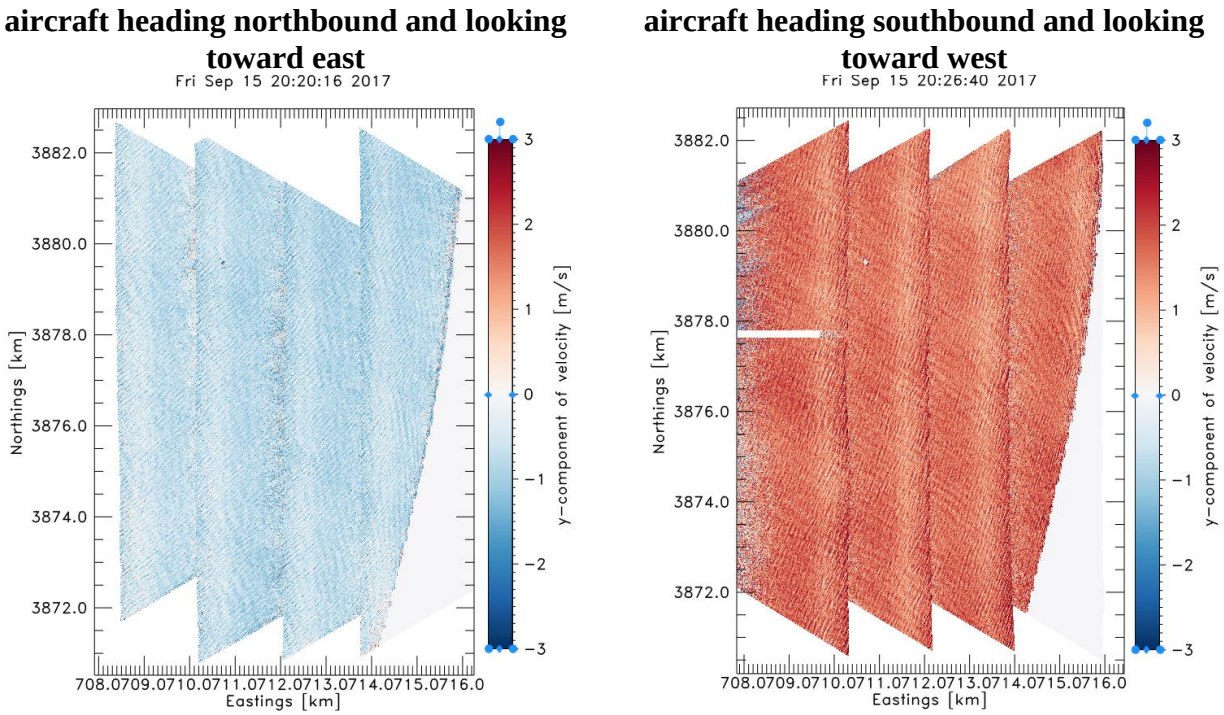

Figure 5.4. y-components of surface current computed from ATI-SAR measurements after subtracting M4S computed InSAR velocities (with zero-current input) from ATI-SAR radial velocities.

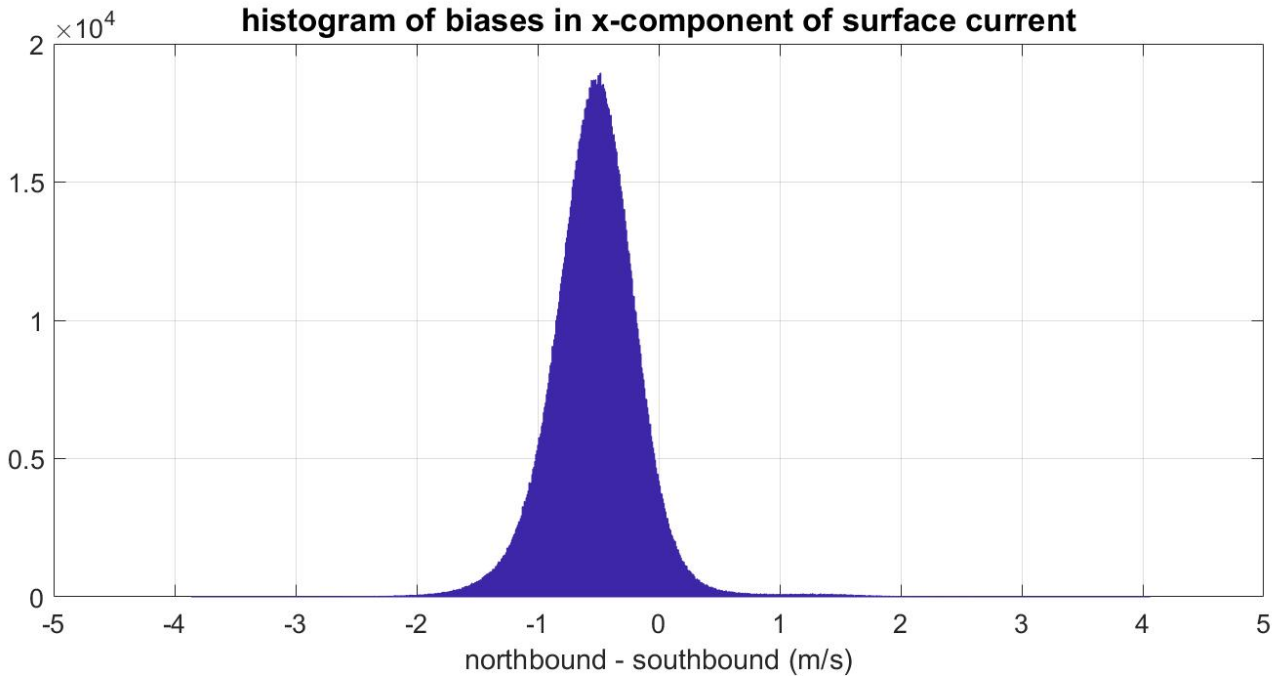

Figure 5.5. Histogram of biases in x-component of retrieved surface current during northbound and southbound flights.

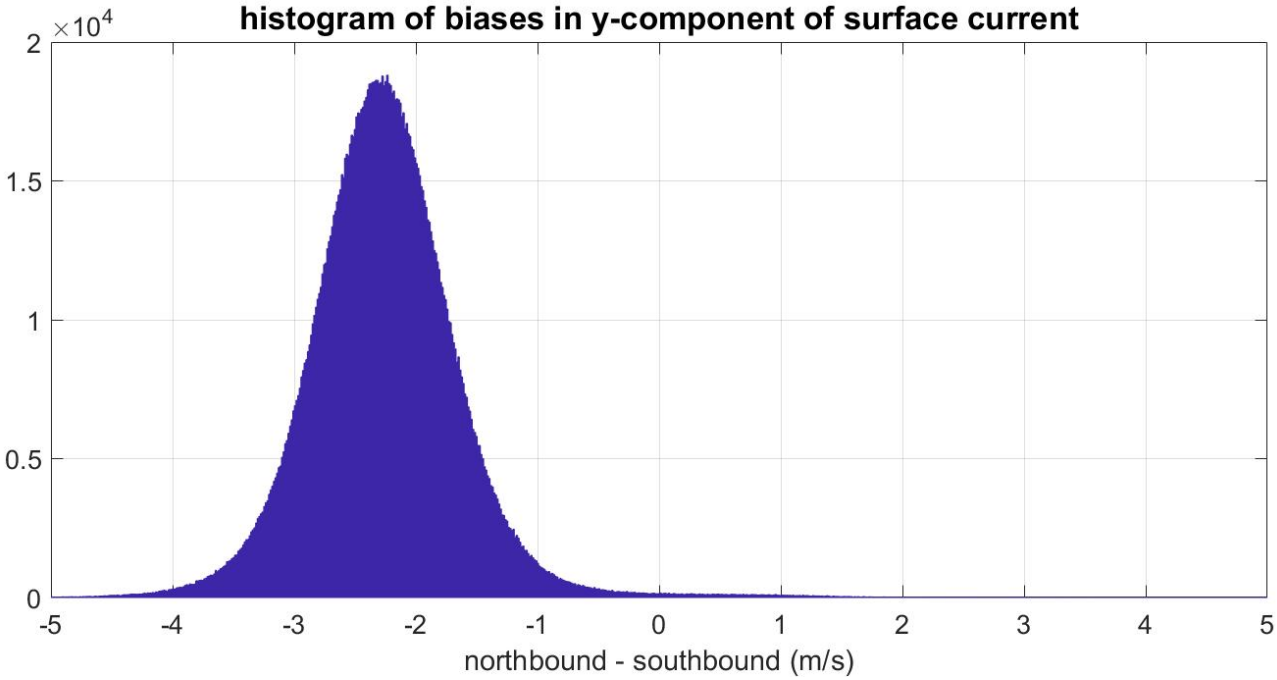

Figure 5.6. Histogram of biases in y-component of retrieved surface current during northbound and southbound flights.

I suggest this bias is due to the mismatch between the estimated wave spectra from M4S model and the actual waves present at the experiment site during the time of data collection.

M4S uses a wave spectrum model, which does not capture the real wave spectrum present at the area under the study (Point Sal, CA). Instead, in the first step of running M4S model the input current and wind fields of a given scenario are converted into a wave spectrum. This wave spectrum is then used in the scattering module of M4S. Therefore, there is a difference between the estimated wave spectrum by M4S and the actual wave spectrum present at the scene during the experiment.

In next section, I present one sample wave spectrum estimated by M4S model, and show how it differs from the actual wave spectrum present at the scene during the experiment and captured by an *in-situ* sensor.

5.2 DIFFERENCE BETWEEN ESTIMATED WAVE SPECTRUM BY M4S MODEL AND ACTUAL WAVE SPECTRUM

The wave spectrum estimated by M4S does not represent the actual wave conditions during the measurements. For instance, it does not have the ocean swell component and only has the wind wave component. During the Point Sal, CA data collection campaigns, several other instruments were present onsite and made simultaneous measurements over the same area of study. These included a set of APL-UW moorings deployed in water and making *in-situ* wave measurements. Figure 5.7 represent the location of five APL-UW moorings over Point Sal area.

As presented in Figure 5.7 the APL mooring #1 is the closest one to the location of APL ATI-SAR data collection north of Point Sal during the September 15 flight experiment. I use the

data collected by APL mooring #1 to calculate the actual wave spectrum present at the scene during the experiment.

Figure 5.7. Locations of APL-UW mooring in Point Sal area.

Figure 5.8 shows M4S model estimated wave spectra in the direction of 300 degrees, which is the direction in which the maximum wave energy comes from (northwest). As depicted, this wave spectrum has only wind wave component at frequency of 0.15 Hz and it does not include lower frequency (less than 0.1 Hz) components.

Figure 5.9 shows an actual wave spectrum from an *in-situ* APL-UW mooring #1 measurements. As depicted, it has both ocean swell and wind wave components at 0.07 Hz and 0.13 Hz, respectively. It also has lower frequency components compared with the spectra estimated by M4S model (presented in Figure 5.8). There are also differences between the actual wave spectra measured by APL-UW mooring and the one estimated from M4S model at higher frequencies (> 0.2 Hz).

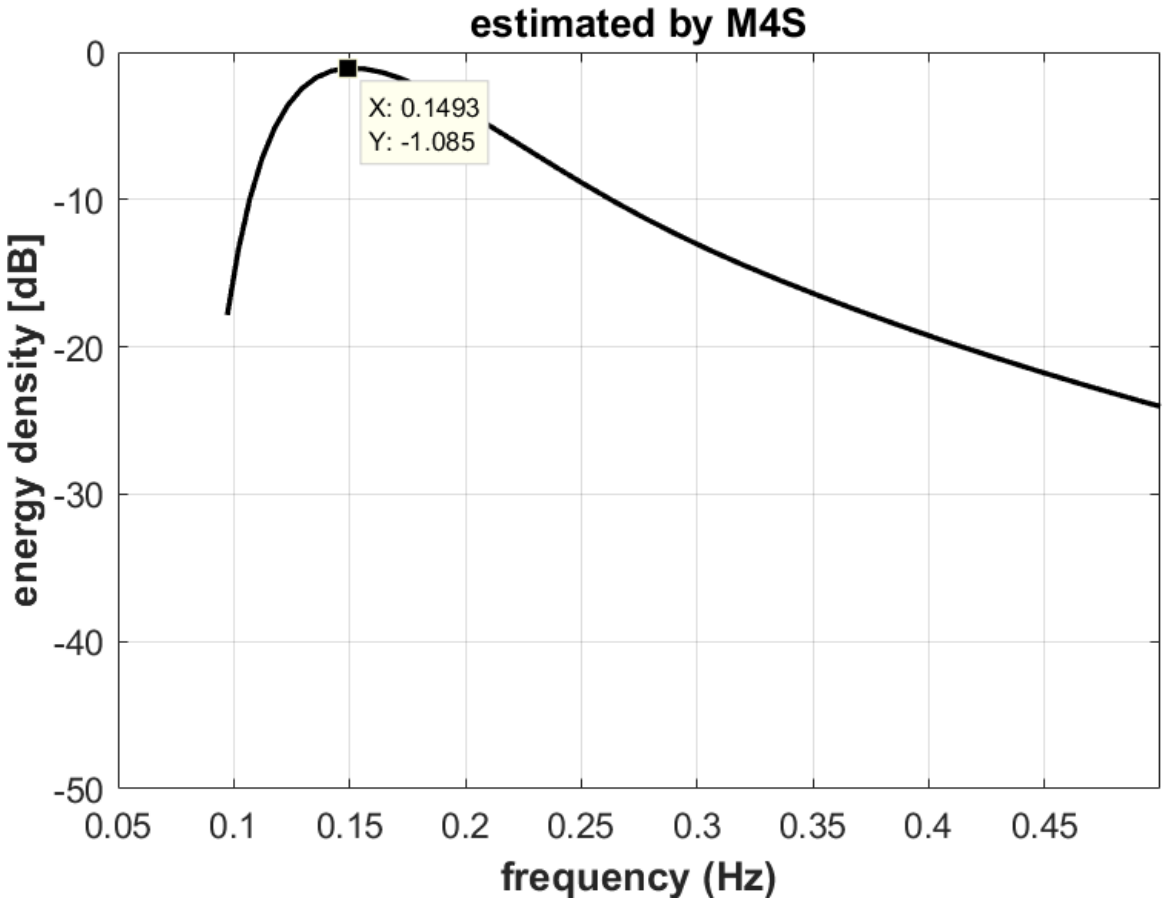

Figure 5.8. Estimated wave spectrum by M4S model.

In order to further investigate the wave-dependant biases in surface current components estimated by ATI-SAR, I propose to incorporate the actual local wave spectra from the *in-situ*

mooring to M4S model. Then, I force M4S model to use the actual wave spectrum for all the calculations in the radar scattering module of the model (for example in order to calculate radial InSAR velocities).

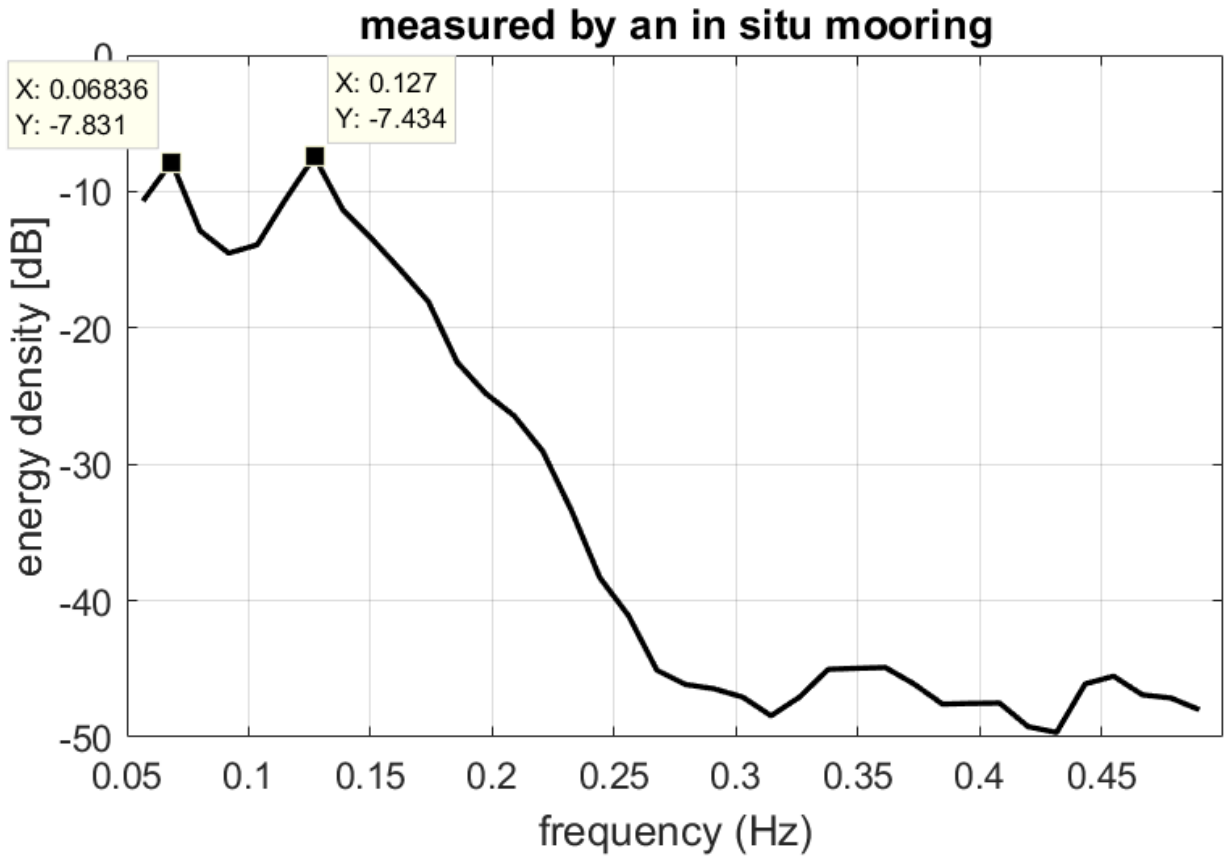

Figure 5.9. Measured wave spectrum by APL-UW mooring.

After applying this modification to the model, M4S model's radial InSAR velocities (with zero-current input) must be calculated. Then, the radial InSAR velocities should be subtracted from the ATI-SAR measured Doppler velocity in order to calculate the redial velocities for both forward- and aft-squinted radars. The resulting ATI-SAR radial velocities should only be representative of surface current.

The x- and y-components of surface current will be calculated afterwards to see how the biases will change. Results will be presented in chapter 6 to show how this wave spectrum modification to M4S model results in improvement in surface current geophysical model function.

Chapter 6. RESULTS AND ANALYSIS

As mentioned in chapter 4, M4S model is initialized with input current and wind speed data. The main advantage of M4S physics-based model is that it does not rely on the empirical data and can be run for simulations at any frequency and polarization, yet it also has weaknesses. For instance, M4S uses a wave spectrum model, which does not capture the actual wave spectrum present. In the first step of running M4S model the input current and wind fields of a given scenario are converted into a wave spectrum. This wave spectrum is then used in the scattering module of M4S.

In order to investigate the biases in ATI-SAR surface current components, I proposed in chapter 5 to update M4S to use a combination of the actual long wave spectrum from an independent source such as *in-situ* moorings, and a modeled shortwave spectrum. I hypothesize that with this update, the ATI-SAR retrieval algorithm should improve and the biases in the surface current components will decrease.

To improve the M4S model I propose to force the model to use the actual wave spectrum instead of having the model to estimate it from input surface current and wind fields. Then I will run the model with the improvement and see how the outputs of the model change. This will help improve the surface current geophysical model functions, which maps the Doppler measurements to ocean surface current measurements.

6.1 ACTUAL WAVE SPECTRUM MEASURED BY IN-SITU APL MOORING INPUT TO M4S

There are different sources for capturing the actual wave spectrum and insert it to M4S model. The first way is to use *in-situ* moorings and measure the actual wave spectrum from them. Based

on Figure 5.7 APL's mooring #1 is the closest mooring to the area under this study north of Point Sal, CA. Therefore, I used the wave spectrum measured by this mooring during the field experiment on September 15 2017 over Point Sal, CA. The long wavelength (lower wavenumber) part of the wave spectrum estimated by M4S from input current and wind fields will be substituted by the actual wave spectrum measured by APL mooring.

Figure 6.1 shows the actual wave spectrum measured by APL mooring in red curve and the estimated wave spectrum by M4S model at one specific direction in blue curve for lower wavenumber part of the spectrum. One can see there are significant differences in wave spectrums in the lower wavenumber part of the spectrum. I substitute the long wavelength (lower wavenumber) part of the spectrum by the mooring measurements. The short wavelength part (larger wavenumber) is kept from the M4S estimated wave spectrum. APL mooring is only capable to measure wave spectrum for lower wavenumber part of the spectrum.

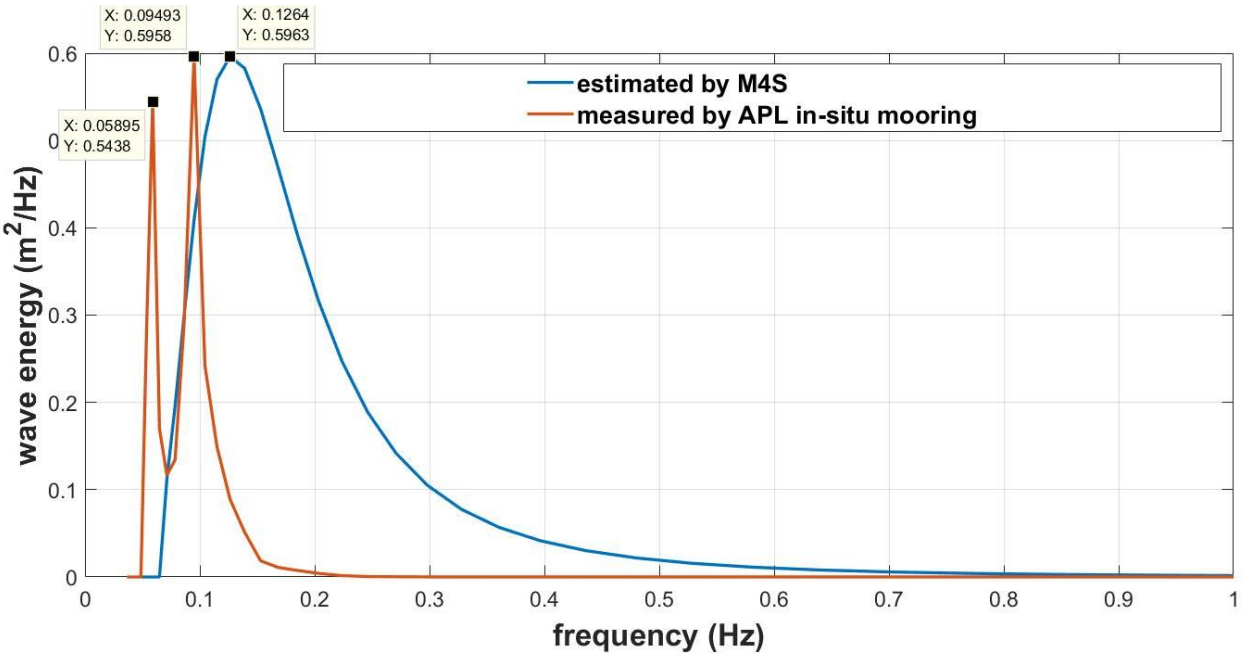

Figure 6.1. M4S estimated wave spectrum and actual wave spectrum measured by APL mooring.

6.2 BIASES IN SURFACE CURRENT COMPONENTS AFTER APPLYING WAVE SPECTRUM MODIFICATION TO M4S MODEL

Figure 6.2 and Figure 6.3 show x- and y-components of ATI-SAR retrieved surface current after applying the wave spectrum modification to M4S model. Left panels present surface velocity components retrieved using the data collected during northbound flights and right panels present the surface velocity components using the data collected during southbound flights.

Although there is still a difference between the surface velocity components retrieved in northbound and southbound flights, the visual comparison between Figure 6.2 and Figure 5.3 and also Figure 6.3 and Figure 5.4 show reduction in biases in retrieved surface velocity components after applying wave spectrum modification to M4S model. The reduction in biases for x-component of surface velocity is more easily observed than the one in y-component. There are still large biases in the y-component of surface velocity during northbound and southbound flights. As it can be seen in Figure 6.3, the y-component of surface velocity retrieved during southbound flights is biased towards positive values compare with the retrieved y-component surface velocity during northbound flights.

Figure 6.4 and Figure 6.5 show the histograms of the difference between the surface velocity components retrieved during northbound and southbound flights and after applying the wave spectrum modification to M4S model for x- and y-component, respectively.

A comparison between Figure 6.4 and Figure 5.5 confirms that the mean value of the difference between the northbound and southbound x-component of surface current is reduced after applying the wave spectra modification to M4S model.

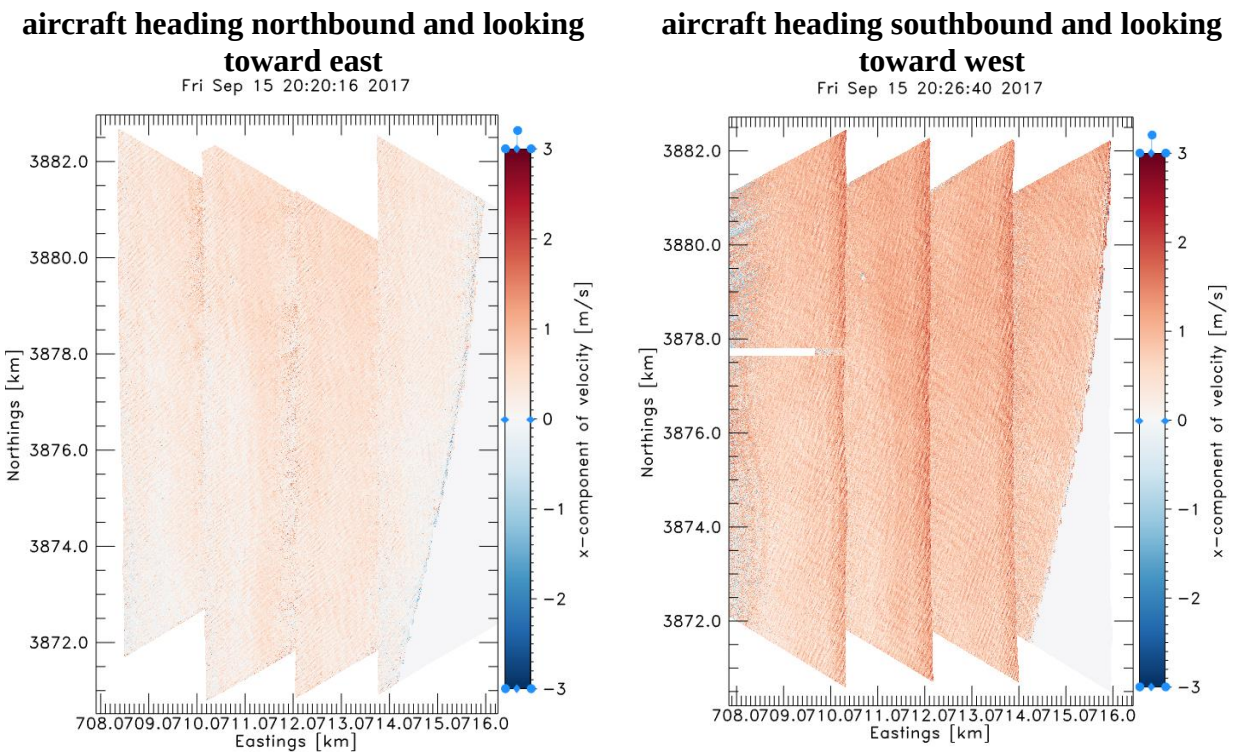

Figure 6.2. x-components of surface current computed from ATI-SAR measurements after subtracting M4S computed InSAR velocities from ATI-SAR radial velocities.

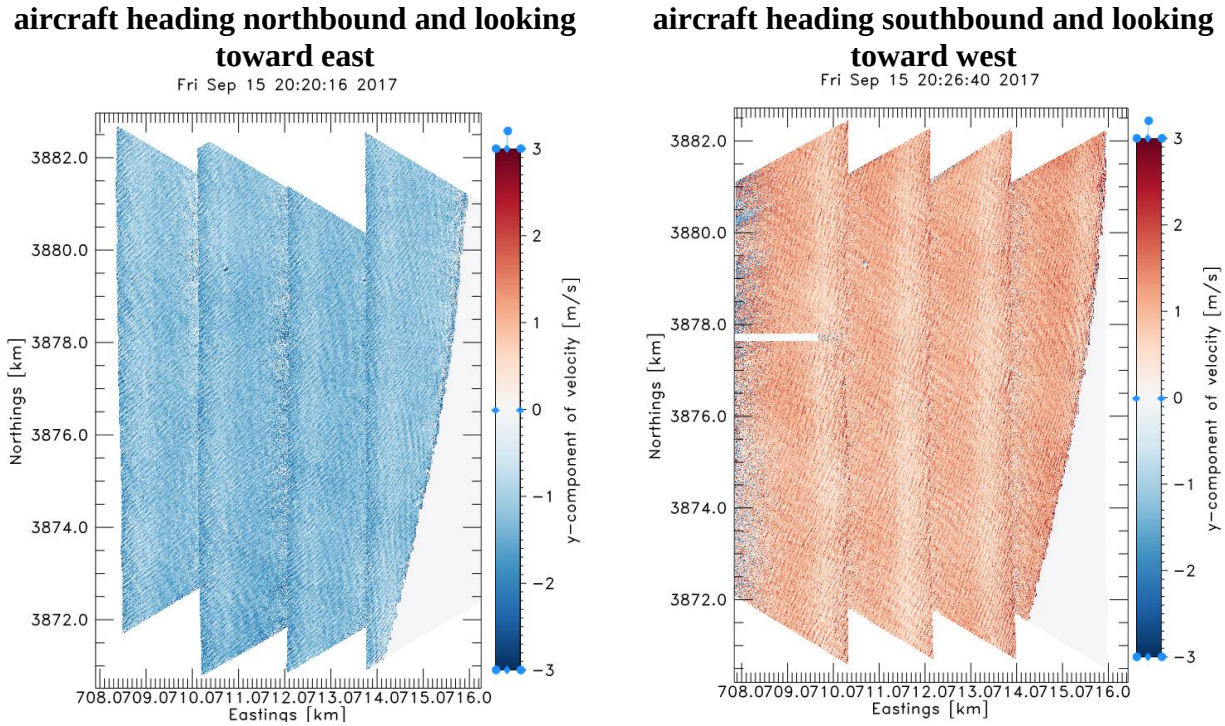

Figure 6.3. y-components of surface current computed from ATI-SAR measurements after subtracting M4S computed InSAR velocities from ATI-SAR radial velocities.

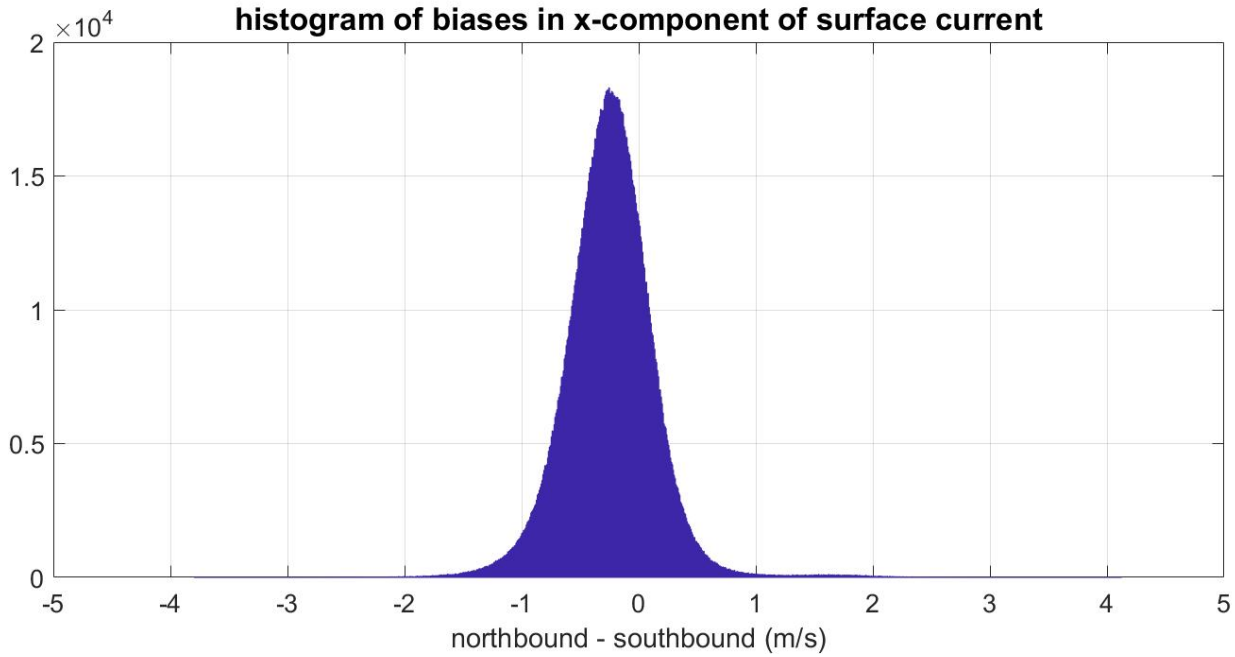

Figure 6.4. Histogram of biases in x-component of retrieved surface current during northbound and southbound flights.

A similar comparison between Figure 6.5 and Figure 5.6 for the differences in y-component of the retrieved surface velocity during northbound and southbound flights show that the bias remains even upon applying the wave spectra modification to M4S model. However, its mean value in Figure 6.5 is reduced in comparison with that presented in Figure 5.6. The reduction in bias is not as significant as the one for the x-component of the surface velocity, however.

In order to apply the wave spectrum modification to the M4S model, I used the actual wave spectrum measured by APL mooring #1, which was present at the scene during the corresponding ATI-SAR flight experiment. This mooring was the closest mooring to the area under the study but it was not in the exact location of the ATI-SAR data collection. Therefore, there might still be differences between the actual wave spectrum present at the experiment site during ATI-SAR data collection and the one captured by the APL mooring #1 and inserted to M4S model in order to improve it. This is one of the reasons of why differences still present

between the surface velocity components retrieved during northbound and southbound flights even applying wave spectrum modification to M4S model.

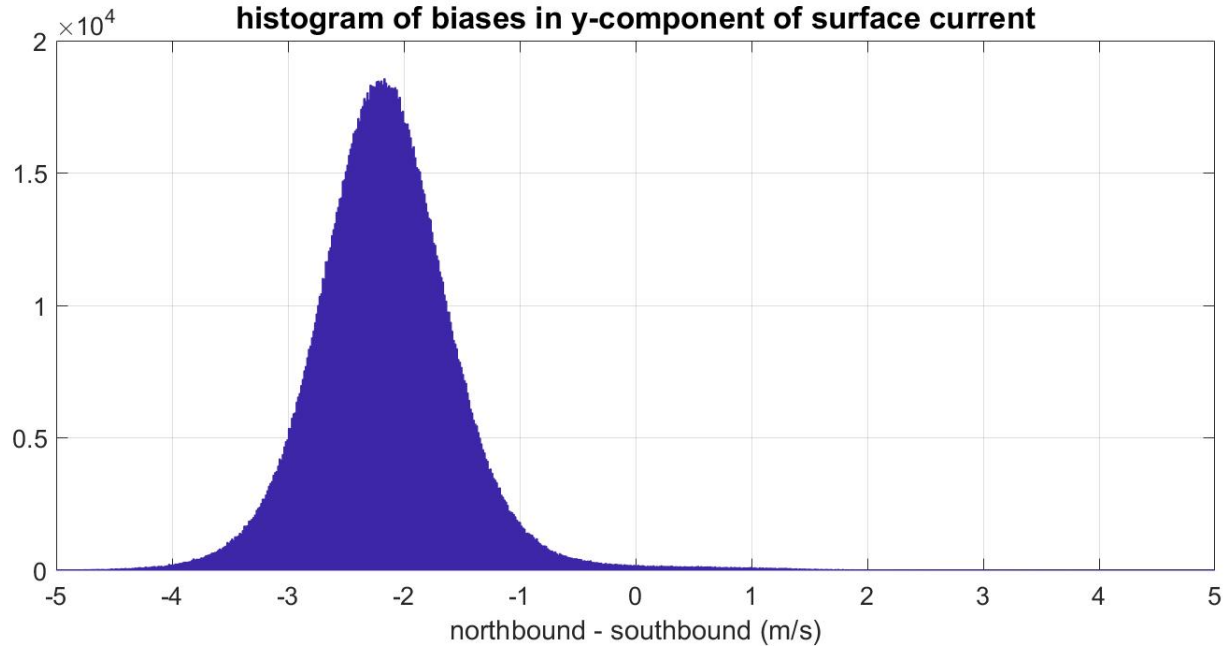

Figure 6.5. Histogram of biases in y-component of retrieved surface current during northbound and southbound flights after applying modification to M4S model.

Another deficiency in the actual wave spectrum inserted into the M4S model in order to improve it, is that the moorings make the wave energy measurements only for lower wavenumber (larger wavelength) part of the spectrum but not for the large wavenumber (lower wavelength) part of the spectrum, which is where Bragg scatter occurs. I kept the wave spectrum information for the larger wavenumber part of the spectrum from what M4S estimates from the input wind fields. This is another possible source for the differences between the actual wave spectrum present at the scene during the experiment and the one input to M4S model in order to improve it. Therefore, it can be another reason to explain why the biases between the ATI-SAR

retrieved surface current components still exists even after applying the wave spectrum modification to M4S model.

In order to compensate for these imperfections of the wave spectrum recorded by *in-situ* APL moorings, I propose to estimate wave spectrum from the data ATI-SAR capture. The next section describes how to estimate wave spectrum from the data collected by APL ATI-SAR. This makes the ATI-SAR surface current retrieval algorithm independent of any secondary instrument measurements such as *in-situ* moorings.

6.3 WAVE SPECTRUM CALCULATION USING ATI-SAR DATA

Besides using the data recorded by *in-situ* moorings in order to have actual wave spectrum information (described in previous section), the second way of achieving the actual wave spectrum is to estimate the wave spectrum from ATI-SAR measurements and then require the M4S model to use this wave spectrum instead of the estimated wave spectrum. This makes the whole process independent of any other sources (such as *in-situ* moorings) and relies only on ATI-SAR measurements.

In this section, I present the method I use to calculate the wave spectrum using ATI-SAR data over Columbia River mouth. Afterwards, this method can be utilized to calculate wave spectrum and force M4S model to use this actual wave spectrum instead of estimated wave spectrum in order to improve the model.

6.3.1 *Ocean surface waves*

Waves on the surface of the ocean have period of 3-25 seconds and are mainly caused by winds. The restoring force for these waves is gravity and hence they are named gravity waves. In this sub section, I describe ocean surface waves' characteristics briefly.

Ocean gravity waves are well-described by linear ocean wave theory. The wave period (T) is the time interval between the passage of two successive wave crests or troughs at a given point, and the wavelength (L) is the horizontal distance between two identical points on two successive wave crests/troughs. Angular frequency ($\omega = 2\pi/T$) and wave number ($k = 2\pi/L$) are computed from wave period and wavelength, respectively. The dispersion relationship relates wave period and wave number through equation (6.14):

$$\omega^2 = gk \tanh(kd) \tag{6.14}$$

Where, g is gravitational acceleration, and d is the water depth.

The most elementary wave theory is the linear wave theory. This theory gives a reasonable approximation of wave characteristics for a wide range of wave parameters. Based on the linear wave theory, the wave phase velocity (C) is related to wavelength *(L)* and water depth *(d)* by equation (6.15).

$$\mathrm{C} = \sqrt{\frac{gL}{2\pi} \tanh\left(\frac{2\pi d}{L}\right)} \tag{6.15}$$

The dispersion relation indicates that waves with different periods travel at different speeds. Gravity waves are typically classified into three regimes, defined by the ratio of the water depth to wavelength (Table 6.6). In deep and shallow water cases, the ratio of water depth to wavelength allows the dispersion relationship to be replaced with an approximate equation.

Table 6.6. Ocean waves classification.

Classification	d/L	Dispersion Relation
Deep Water	$1/2$ to ∞	$\omega^2 \approx gk$
Intermediate Water	$1/20$ to $1/2$	$\omega^2 = gk \tanh(kd)$
Shallow Water	0 to $1/20$	$\omega^2 \approx gk^2 d$

In shallow and intermediate depths (compare with deep water), waves refract (change direction), shoal, and break, resulting in a loss of energy. Both of these processes cause a change in the wave energy spectrum.

6.3.2 *Wave spectrum retrieval algorithm*

This section describes the algorithm I use to extract wave information from ATI-SAR data. The algorithm was introduced in [9], and is based on linear approximation to the non-linear integral transform relating ocean wave spectra to the ATI-SAR image spectra that was derived by Bao et al [38]. The approximation is given by equation (6.16).

$$\mathrm{P}_{\phi}(k) = [H(k)]^2 \, E(k) \tag{6.16}$$

Here, k denotes the 2-D ocean wave number, and $P_{\phi}(k)$ and $E(k)$ denote the 2-D ATI-SAR phase image spectra and the ocean wave spectrum, respectively. $H(k)$ represents the linear approximation of the ocean wave ATI-SAR phase modulation transfer function.

As a first step, I calculate the interferometric phase from the two sets of single look complex data (each related to one radar frequency channel of the ATI-SAR receivers). To calculate the 2-D phase image spectrum $P_{\phi}(k)$, I take the squared absolute value of the 2-D Fourier transform of the interferometric phase as given in equation (6.17).

$$\mathrm{P}_{\phi}(k) = |FT_{2-D}(Interferometric\ phase|^2 \tag{6.17}$$

6.3.2.1 Ocean wave ATI-SAR phase modulation transfer function

Equation (6.16) relates ocean wave spectra to the ATI-SAR phase image spectra. In this equation, $H(k)$ is given by equation (6.18) [9].

$$\mathrm{H(k)} = \left(\frac{k_i B}{V_{AC}}\right) \omega G(\theta, \phi) \left[1 - 3\frac{k_x^2 R^2}{V_{AC}^2} f^u(0)\right]^2 \tag{6.18}$$

Here, k_i is the radar electromagnetic incident wave number, B is the interferometric baseline between two antennas, and V_{AC} is the platform velocity, which are nominally 0.39 m and 45 m/s for the APL-UW ATI-SAR system, respectively.

A geometric function $G(\theta, \phi)$, which depends on the incidence angle θ and the wave propagation direction with respect to the radar azimuth direction ϕ, is given by equation (6.19).

$$\mathrm{G}(\theta, \phi) = \sqrt{\sin^2(\theta)\sin^2(\phi) + \cos^2(\theta)} \tag{6.19}$$

The term f^u in equation (6.18) denotes the auto-covariance function of the radial orbital velocity of the long ocean waves [38].

H(k) is an approximation, and represents a filter that transforms the ocean wave spectrum to the measured interferometric phase spectrum. The filter accounts for the motion of the waves during the time taken to acquire the SAR image. In this research, I invert the transformation simply by using equation (6.20) in order to calculate the wave spectrum *E(k)*.

$$\mathrm{E(k)} = \frac{P_{\phi}(k)}{[H(k)]^2} \tag{6.20}$$

One should note that equation (6.20) works only when *H(k)* is not zero. Since *H(k)* is an approximation, I substitute zero values of *H(k)* with a very small non-zero numbers in order to prevent zeros in the denominator.

To be able to calculate *E(k)* from this algorithm, some ancillary data is also required. Significant wave height and the direction from which the waves at the dominant period are coming are two examples of secondary parameters. For the area of Columbia River mouth, these parameters can be attained from the historical archived *in-situ* measurements provided by the National Data Buoys Center website (NDBC) [39]. Figure 6.6 shows NDBC buoys location on the map.

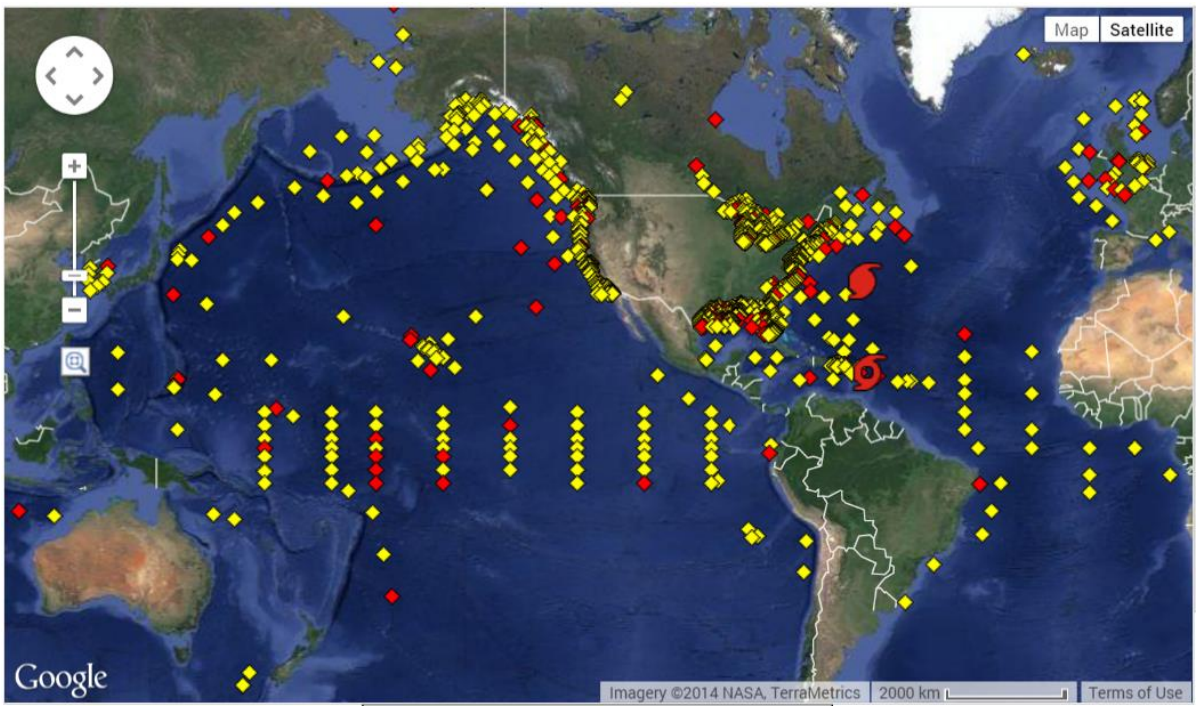

Figure 6.6. NDBC's stations: yellow squares and orange squares show the stations with recent data and stations with historical data, respectively [39].

6.3.2.2 NDBC data

Buoy station number 46243 is the closest one to the experiment site and is used to retrieve the required ancillary data for this research over the mouth of Columbia River. The position of this station is presented in Figure 6.7.

Historical data for this station is available since 2009 and it is possible to extract the necessary information from the data recorded at this station in order to run the retrieval algorithm for wave spectrum calculations.

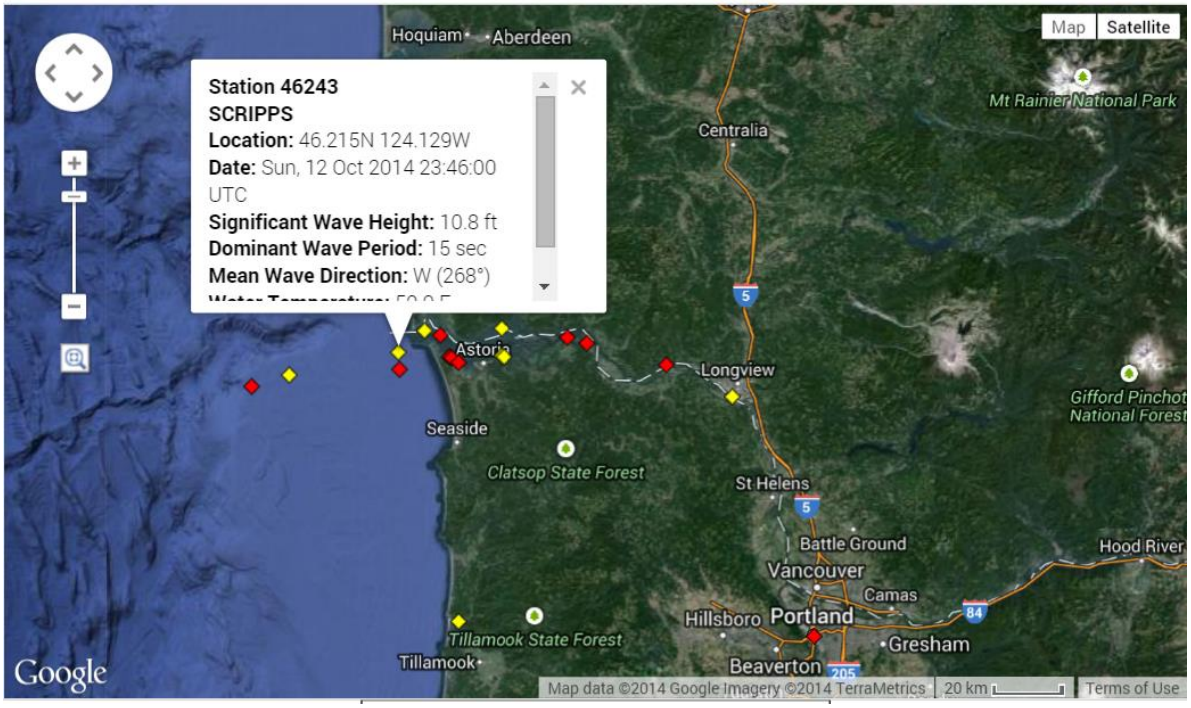

Figure 6.7. The closest NDBC station to the mouth of Columbia River [32].

6.3.3 *Calculated wave spectrum from ATI-SAR data*

I use the wave spectrum retrieval algorithm presented in section 6.3.2.1 and calculate wave spectrum for different cases. First, I introduce the ATI-SAR data set, which I used for wave spectrum calculation over MCR.

6.3.3.1 Data set

DARLA (Data Assimilation and Remote Sensing for Littoral Application) was a collaborative project funded by ONR (Office of Naval Research). APL-UW was one of the collaborators of this project [40]. The Navy needs to know how fast the water is moving, for instance, to deploy ships on a beach or to steer a ship to an inlet.

At the mouth of Columbia River between Washington and Oregon, strong river currents meet Pacific Ocean swells and wind driven waves and makes *in-situ* measurements very difficult. Therefore, remote sensing methods are valuable. I used ATI-SAR data captured by APL-UW C-band ATI-SAR system over Columbia River inlet during the 3 days (4^{th}, 6^{th} and 8^{th} June 2013) of the flight experiments. Then I employed the wave spectrum calculation algorithm described in section 6.3.2.1 to estimate wave spectrum from ATI-SAR data.

In order to validate this method, wave direction and wave period values at the mouth of Columbia River are calculated from the wave spectrum and the results are validated against the data from NDBC archive data.

6.3.3.2 Wave spectrum calculations

As described in chapter 2 the interferometric phase is calculated from ATI-SAR date. In order to mitigate the noise level of the interferometric phase, one step of 4-cell averaging is applied and one example of the resulting averaged-interferometric phase is shown in Figure 6.8.

Figure 6.8. Interferometric phase after 4-cell averaging.

In order to be able to resolve the larger ocean waves (with large values of wave period *T*, which results in smaller wavenumber *k*) I choose a number to flag the *H* function for the smaller values of ocean wave number *k*. For this study, I simply flag the *H* function for ocean wave numbers less than 0.03 [41]. This number is an empirical choice and can be modified when running the algorithm for more cases and determine more reliable threshold value based on investigating more cases. Also, in order to be able to resolve the waves from ocean wave spectra, I have to apply a smoothing function to the calculated ocean wave spectra.

Figure 6.9 – Figure 6.14 show the interferometric phase in left panel and wave spectrum in the right panel for 6 different cases. To create each image the data collected by one ATI-SAR (either forward-looking or aft-looking radar) is used. It took couple of minutes to collect the

corresponding data. Each image spans 750 meters by 750 meters. This image size is chosen in order to minimize the change in wave field due to the variation in bathymetry. However, the images are limited to only a few wave periods, limiting the wavenumber resolution of the wave spectra at long wavelengths.

In the first case presented in Figure 6.9, wave refraction is visible in the interferometric phase image (left panel). This causes the energy in the derived wave spectrum to be spread out in wavenumber space, resulting in a broader peak in the wave spectrum. Because I derive the wave spectrum from a snapshot image, I cannot resolve the direction of the waves. However, I know that the waves travel in the onshore direction, so the wave direction ambiguity can easily be resolved.

Figure 6.10 shows interferometric phase over small area where the wave direction does not vary too much. Thus, the resulted wave spectrum presented in the right panel shows narrower peaks in the wave spectrum.

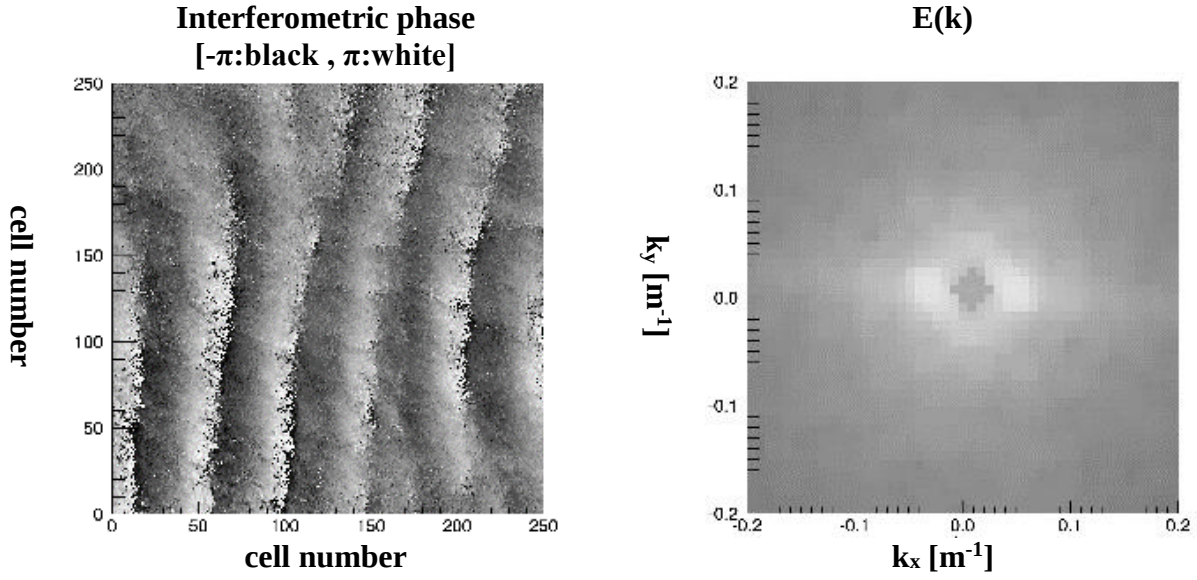

Figure 6.9. Interferogram and wave spectra for June 08 2013, 10:42:52 [41].

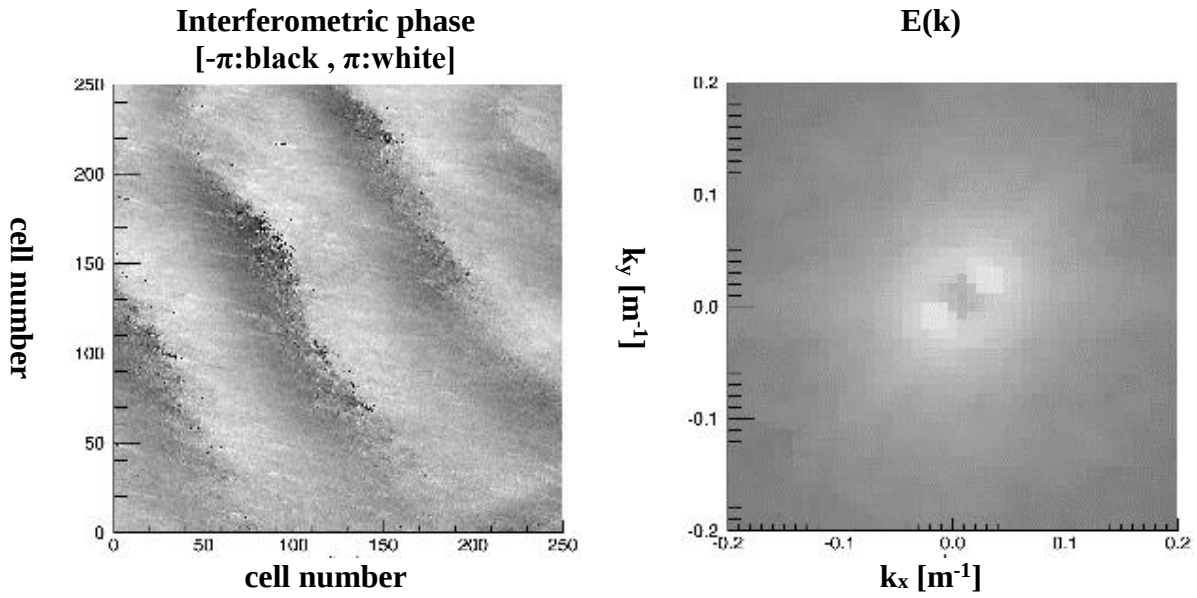

Figure 6.10. Interferogram and wave spectra for June 08 2013, 12:15:51 [41].

Figure 6.11 and Figure 6.12 present other cases with less wave energy as it can be seen in the left panels. Therefore, in compare with Figure 6.10, waves are detected less clearly.

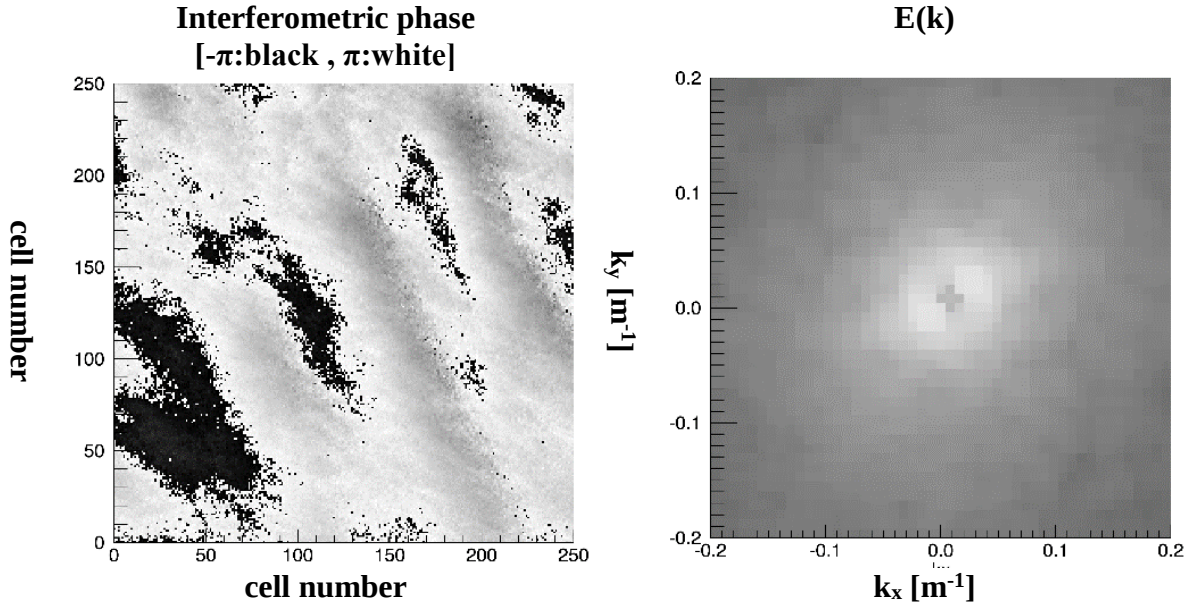

Figure 6.11. Interferogram and wave spectra for June 08 2013, 14:59:16 [41].

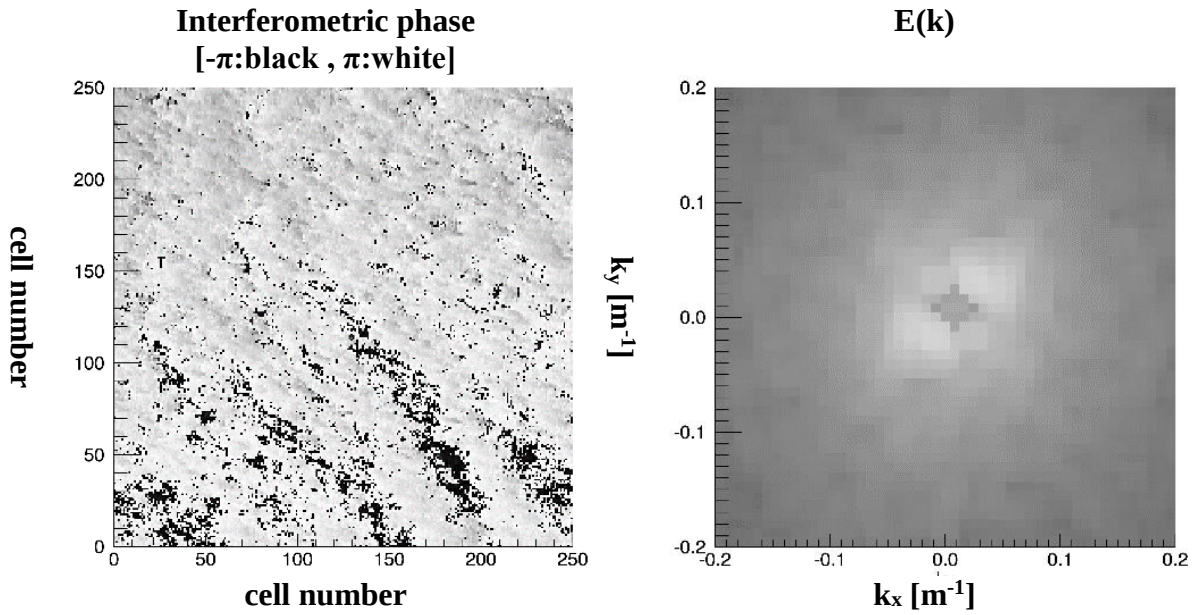

Figure 6.12. Interferogram and wave spectra for June 06 2013, 17:32:14 [41].

Figure 6.13 represents the interferometric phase and wave spectrum for a case with variable wave direction. Thus, two vague bright areas are spotted in the wave spectrum.

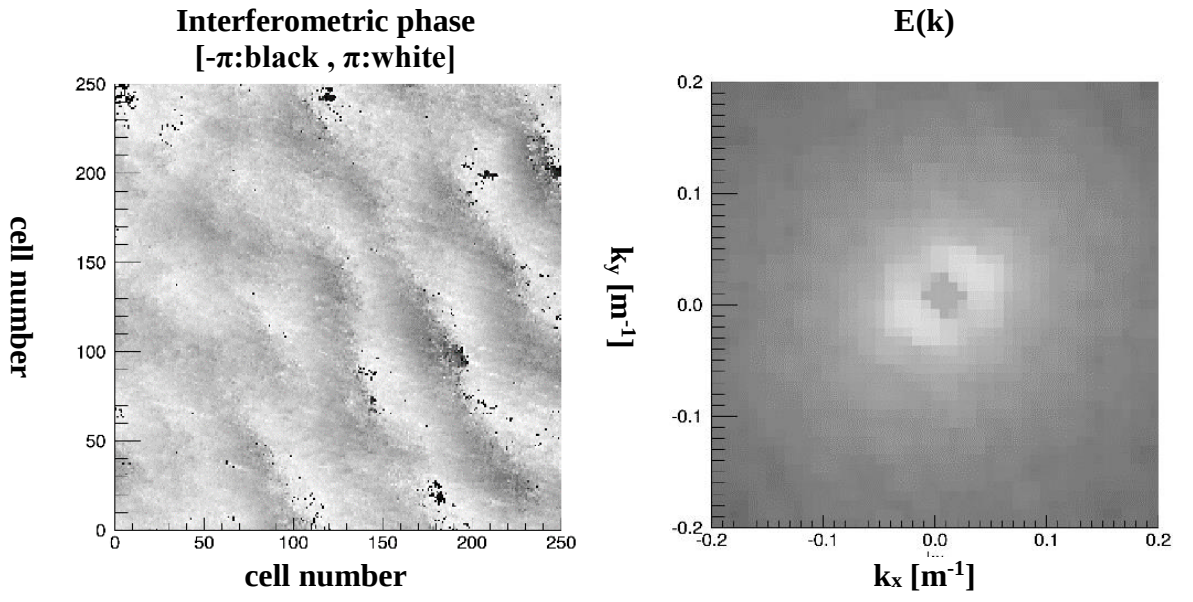

Figure 6.13. Interferogram and wave spectra for June 08 2013, 16:35:21 [41].

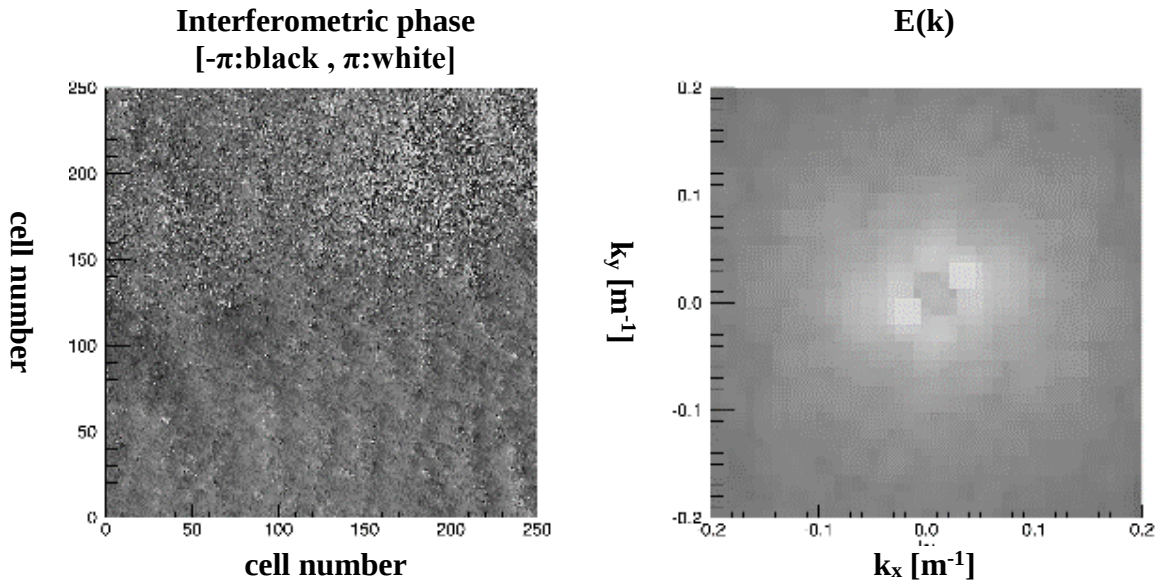

Figure 6.14. Interferogram and wave spectra for June 06 2013, 15:06:04 [41].

Although Figure 6.14 shows a noisy interferometric phase case, it is still possible to detect the wave energy from the wave spectrum. This is because this case contains much shorter waves and consequently few more complete wave periods in one small box.

6.3.4 *Validation*

To validate the results, I use the wave information from the National Data Buoy Center historical database as reference values and compare the ATI-SAR results with them. The Table 6.7 and Table 6.8 shows these values for wave direction and wave period calculation, respectively.

Table 6.7. Wave direction values measured by ATI-SAR and from NDBC database.

	Case #1	Case #2	Case #3	Case #4	Case #5	Case #6	Case #7
wave direction by ATI-SAR [degrees]	275	234	237	237	237	218	301
wave direction from NDBC [degrees]	251	231	258	261	299	269	294
Difference [degrees]	24	3	21	24	62	51	7

Table 6.8. Wave period values measured by ATI-SAR and from NDBC database.

	Case #1	Case #2	Case #3	Case #4	Case #5	Case #6	Case #7
wave period by ATI-SAR [sec]	5.81	7.49	14.52	14.52	7.49	8.73	7.49
wave period from NDBC [sec]	16.67	16.67	13.32	15.38	6.25	9.88	7.14
Difference [sec]	10.86	9.18	1.20	0.86	1.24	1.15	0.35

In order to have closer look and compare the ATI-SAR wave parameters (wave direction and wave period) measurements with the reference values from NDBC records in a quantitative base, I present scatterplots for wave direction and wave period in Figure 6.15 and Figure 6.16, respectively.

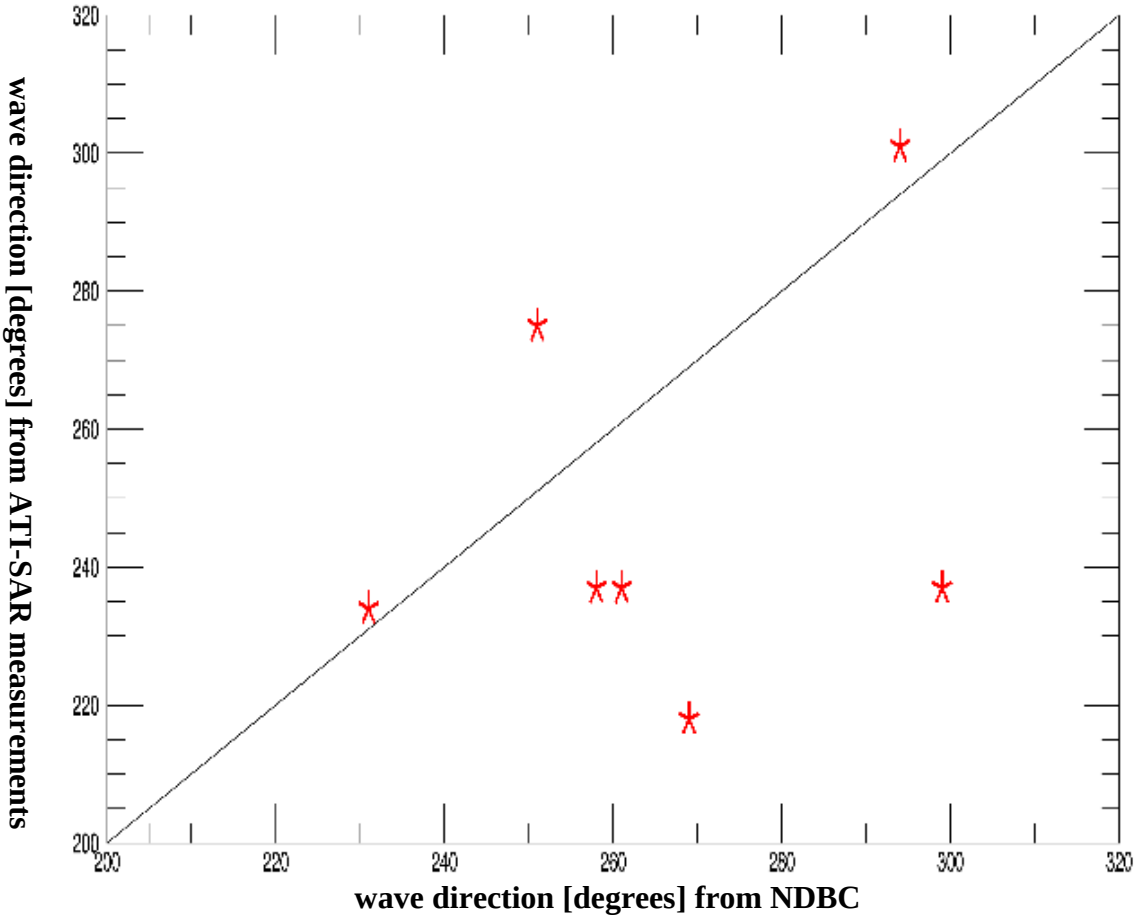

Figure 6.15. Comparison of ATI-SAR wave direction measurements with NDBC.

As it can be seen from the scatterplots, for most cases there is a good agreement between the wave information retrieved form the APL ATI-SAR data and NDBC data. However, there are cases with poor agreement. There are several possible reasons for that. For instance, the chosen NDBC station is not exactly in the same area where APL ATI-SAR platform flew during the experiment. It is only the closest station to the area and so, this could cause some differences between the ATI-SAR measurements and the data provided by the NDBC station.

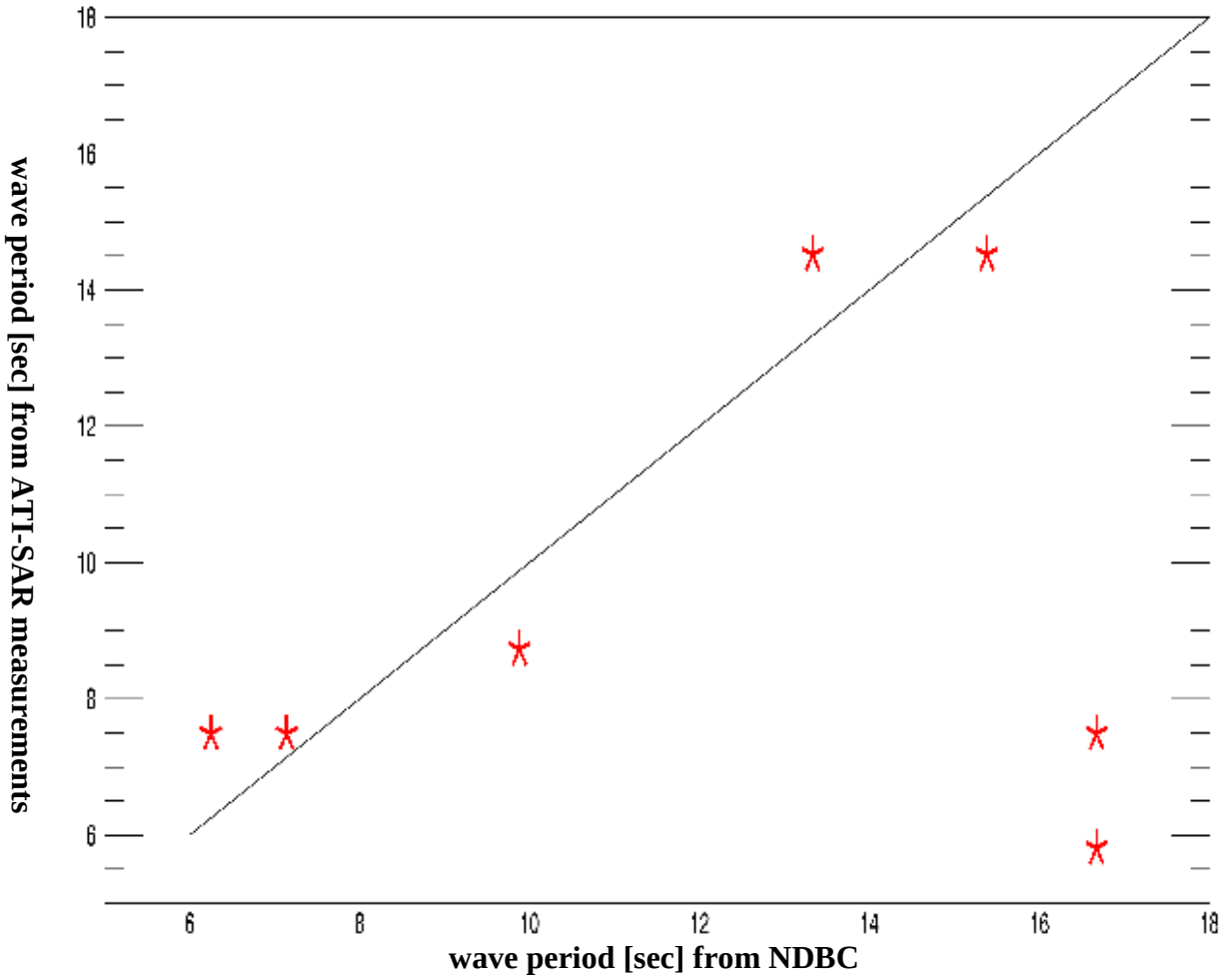

Figure 6.16. Comparison of ATI-SAR wave period measurements with NDBC.

Besides that, and more importantly the MCR is a very challenging environment since its bathymetry is varying dramatically. Therefore, waves shoal and break in this area and their direction change even over a small area.

6.4 FUTURE WORKS

For future studies, I propose to use ATI-SAR data to calculate actual wave spectrum using the algorithm presented in previous section. Then the calculated wave spectrum from ATI-SAR data should be inserted to M4S model (similar to the procedure in sections 6.1) in order to improve M4S model. Hence, the surface current geophysical retrieval algorithm improvement will be independent of any other sources such as *in-situ* mooring data.

After applying modification to M4S model, the radial InSAR velocities calculated by M4S (initiated with zero-current input) should be subtracted from the Doppler velocity measured by ATI-SAR. Afterwards, surface current components are retrieved from the Doppler measurements using the modified geophysical model function.

Yet the wave spectrum retrieval algorithm needs more studies and further investigation to be tuned for using in such dramatic bathymetry similar to the one in the Mouth of Columbia River.

6.5 CONCLUSION

The data collected by the APL C-band dual-beam ATI-SAR were used to generate surface current maps. In order to generate the surface current maps the algorithm described in chapter 3 was used and the results were presented. Differences were observed in the retrieved surface current components during successive northbound and southbound flights and M4S model (introduced in chapter 4) was used to investigate the biases.

In chapter 5, M4S model was initiated with the corresponding radar parameters similar to the ones in the field experiment to collect ATI-SAR data and zero-current input to the model. The radial InSAR velocity output of M4S model was inserted to the surface current retrieval

algorithm and the retrieved surface current components were presented for consecutive northbound and southbound flight tracks after applying this modification to the algorithm.

Biases in the surface current components retrieved during successive northbound and southbound flights were observed even after using M4S InSAR radial velocities outputs in the surface current retrieval algorithm. I suggested that the error is due to the significant differences between the actual wave spectrum and the estimated wave spectrum by M4S from input winds. M4S estimates the wave spectrum from the input wind field to the model and does not use the actual wave spectrum present at the scene.

In the beginning of chapter 6, in order to improve the geophysical model function for surface current, wave spectrum modification was applied to M4S model. To attain the actual wave spectrum, the measurements by APL *in-situ* mooring was used. The modified version of M4S was run and the InSAR radial velocities outpour of M4S was inserted to the surface current retrieval algorithm. The retrieved surface current components were presented and the biases were explored.

After applying the wave spectrum modification to M4S model, reduction in the biases in surface current components retrieved during successive northbound and southbound flights were observed. The reduction in biases in the x-component of surface current was more significant than the one observed in the y-component of surface current.

Suggestions were made for possible reasons for the remaining biases observed in the surface current components. Furthermore, a method was introduced to calculate the wave spectrum form ATI-SAR data and insert it to M4S model in order to apply the wave spectrum modification for future studies.

The idea of improving M4S model by forcing it to use the actual wave spectrum in order to modify the surface current retrieval algorithm used for ATI-SAR data is new and was presented for the first time in this thesis. Preliminary results were presented, which shows improvement to the surface current geophysical model function. However, more work is needed to be done in order to be able to run M4S with the actual fully-directional wave spectrum, which includes wave energy information for the full range of wavelengths of the spectrum.

The method presented in section 6.3 can be used to calculate the actual wave spectrum form the data collected by the APL ATI-SAR. Future work should be focused to use this method to generate the actual wave spectrum from ATI-SAR data and force M4S model to use the calculated wave spectrum from ATI-SAR data. The radial InSAR velocities output of M4S should be inserted to the surface current retrieval algorithm and the surface current components should be calculated, afterwards. More reduction to the differences between the retrieved surface current components during northbound and southbound flights are expected.

BIBLIOGRAPHY

[1] Lagerloef, G.S.E., R. Lukas, F. Bonjean, J.T. Gunn, G.T. Mitchum, M. Bourassa, A.J. Busalacchi, "El Nino Tropical Pacific Ocean surface current and temperature evolution in 2002 and outlook for early 2003", Geophysical Research Letter, Vol. 30, No. 10, 1514, 2003.

[2] Lagerloef, G.S.E., G.Mitchum, R.Lukas and P.Niiler, "Tropical Pacific near-surface currents estimated from altimeter, wind and drifter data", Journal of Geophysical Research, 104, pp. 23,313-23,326, 1999.

[3] E. Rodriguez et al., " Air-Sea Exchange Drivers of Climate Variability, Ocean Circulation, and Weather: A case for Coincident Observations of Ocean Surface Winds and Currents", community NRC RFI2 response to Decadal Survey for Earth Science and Applications from Space.

[4] R. Romeiser, H. Runge, S. Suchandt, R. Kahle, C. Rossi and P. S. Bell, "Quality Assessment of Surface Current Fields From TerraSAR-X and TanDEM-X Along-Track Interferometry and Doppler Centroid Analysis," in IEEE Transactions on Geoscience and Remote Sensing, vol. 52, no. 5, pp. 2759-2772, May 2014.

[5] R. Romeiser, W. Alpers, V. Wismann, “An improved composite surface model for the radar backscattering cross section of the ocean surface: 1. Theory of the model and optimization/validation by scatterometer data”, Journal of Geophysical Research, vol. 102, pp. 25237-25250, 1997.

[6] R. Romeiser, W. Alpers, V. Wismann, “An improved composite surface model for the radar backscattering cross section of the ocean surface: 2. Model response to surface roughness variations and the radar imaging of underwater bottom of topography”, Journal of Geophysical Research, vol. 102, pp. 25251-25267, 1997.

[7] Merrill I. Skolnik, “RADAR handbook”, Mc Graw Hill, Third edition, 2008.

[8] R.M. Golstein and H. A. Zebker, “Interferometric radar measurements of ocean surface currents,” Nature, vol.328, pp. 707-709, 1987.

[9] D. Kim, W. M. Moon, D. Moller, and D. A. Imel, "Measurements of ocean surface waves and currents using L- and C-band along-track interferometric SAR," IEEE Trans. Geosci. Remote Sensing, vol.41, pp.2821–2832, 2003, doi: 10.1109/TGRS.2003.817210.

[10] M. A. Sletten, "An analysis of gradient-induced distortion in ATI-SAR imagery of surface currents," in *IEEE Transactions on Geoscience and Remote Sensing*, vol. 44, no. 7, pp. 1995-2002, July 2006.

[11] M. Edwards, D. Madsen, C. Stringham, A. Margulis, B. Wicks and D. G. Long, "microASAR: A Small, Robust LFM-CW SAR for Operation on UAVs and Small Aircraft," IGARSS 2008 - 2008 IEEE International Geoscience and Remote Sensing Symposium, Boston, MA, 2008, pp. V - 514-V - 517.

[12] G. Farquharson, "An FMCW Along Track Interferometry Synthetic Aperture Radar", Internal APL-UW report, 2013, Seattle.

[13] G. Farquharson, H. Deng, Y. Goncharenko and J. Mower, "Measurements of the Nearshore Ocean with FMCW ATI SAR", 10th European Conference on Synthetic Aperture Radar, Berlin, Germany, 2014, pp. 1-4, 2014.

[14] G. Farquharson, H. Deng, Y. Goncharenko and J. Mower, "Dual-beam ATI SAR measurements of surface currents in the nearshore ocean", IEEE Geoscience and Remote Sensing Symposium, Quebec City, QC, 2014, pp. 2661-2664, 2014.

[15] C. Stringham, D. G. Long, "GPU processing for UAS-based LFM-CW stripmap SAR", Photogrammetric Eng. and Remote Sens, vol. 80, no. 12, pp. 1107-1115, Dec. 2014.

[16] M. Balaban et al., "Study of the ATI SAR target signature for non-linear airborne tracks," 2017 IEEE First Ukraine Conference on Electrical and Computer Engineering (UKRCON), Kiev, 2017, pp. 63-66.

[17] http://www.stccmop.org/datamart/observation_network

[18] Rodriguez, E.; Wineteer, A.; Perkovic-Martin, D.; Gál, T.; Stiles, B.; Niamsuwan, N.; Rodriguez Monje, R., "Estimating Ocean Vector Winds and Currents Using a Ka-Band Pencil-Beam Doppler Scatterometer.", Remote Sens. 2018, 10, 576.

[19] S. Aslebagh, G. Farquharson, E. Rodriguez and D. Perkovic-Martin, "Nearshore ocean surface current estimation comparison in C-band and KA-band," 2017 IEEE International Geoscience and Remote Sensing Symposium (IGARSS), Fort Worth, TX, 2017, pp. 410-413.

[20] Fedderson F., et al., "Inner Shelf Dynamics Science and Experiment Plan", Technical Report, APL-UW, 1602, October 2016.

[21] https://scripps.ucsd.edu/projects/innershelf/metwavecirculation-forecasts/

[22] S. Aslebagh, G. Farquharson, J. D. Sahr and R. Romeiser, "Wave-dependent directional biases in airborne ocean surface current estimation", 2018 IEEE International Geoscience and Remote Sensing Symposium (IGARSS), Valencia, Spain, 2018.

[23] H. Deng, G. Farquharson, J. Sahr, Y. Goncharenko and J. Mower, "Phase Calibration of an Along-Track Interferometric FMCW SAR," in IEEE Transactions on Geoscience and Remote Sensing, vol. 56, no. 8, pp. 4876-4886, Aug. 2018.

[24] G. Farquharson, S. Aslebagh and J. Mower, "Calibration of a miniaturized FMCW ATI-SAR for normalized radar cross section measurement," 2015 IEEE International Geoscience and Remote Sensing Symposium (IGARSS), Milan, 2015, pp. 1280-1283.

[25] H. Deng and G. Farquharson, "A robust phase calibration algorithm for a dual-channel along-track interferometric FMCW SAR," 2014 IEEE Geoscience and Remote Sensing Symposium, Quebec City, QC, 2014, pp. 25-28.

[26] D. Moller, S. J. Frasier, D. L. Porter, R. E. McIntosh, “Radar-derived interferometric surface currents and their relationship to subsurface current structure”, Journal of Geophysical Research, Volume 103, Pages 12839-12852, 1998.

[27] H. Deng, G. Farquharson, J. Thomson, S. Moghimi and T. Ozkan-Haller, "An analysis of error in surface current mapping by an along-track interferometric FMCW SAR," 2016 IEEE International Geoscience and Remote Sensing Symposium (IGARSS), Beijing, 2016, pp. 3215-3218.

[28] R. Romeiser and D. R. Thompson, "Numerical study on the along-track interferometric radar imaging mechanism of oceanic surface currents," in IEEE Transactions on Geoscience and Remote Sensing, vol. 38, no. 1, pp. 446-458, Jan 2000.

[29] European Space Agency, Earth online, Radar course (https://earth.esa.int)

[30] Lange, P., & Hiifnerfuss, H., “Drift response of monomolecular slicks to wave and wind action”, Journal of Physical Oceanography, 8(1), 142-150, 1978.

[31] R. Romeiser, “M4S 3.2.1 User’s Manual”, February 2008.

[32] Romeiser, R., Eine verbesserte Theorie zur Modulation der Radar-Rückstreuung von der Meeresoberfläche auf der Basis eines Drei-Skalen-Modells, Dissertation, 118 pp., Fachbereich 15 (Geowissenschaften), Universität Hamburg, Hamburg, Germany, 1993.

[33] Romeiser, R., A. Schmidt, and W. Alpers, A three-scale composite surface model for the ocean wave–radar modulation transfer function, J. Geophys. Res., 99, 9785-9801, 1994.

[34] Schmidt, A., V. Wismann, R. Romeiser, and W. Alpers, Simultaneous measurements of the ocean wave–radar modulation transfer function at L, C, and X bands from the research platform Nordsee, J. Geophys. Res., 100, 8815-8827, 1995.

[35] Zhang, Y., and A. M. Baptista , SELFE: "A semi-implicit Eulerian-Lagrangian finite-element model for cross-scale ocean circulation", Ocean Modell., 21(3–4), 71–96, 2008.

[36] https://www.myroms.org/

[37] G. Farquharson, S. Aslebagh and R. Romeiser, "Estimating Nearshore Ocean Currents from Airborne ATI-SAR," Proceedings of EUSAR 2016: 11th European Conference on Synthetic Aperture Radar, Hamburg, Germany, 2016, pp. 1-5.

[38] Mingquan Bao, W. Alpers, and C. Bruning, "A new nonlinear integral transform relating ocean wave spectra to phase image spectra of an along-track interferometric synthetic aperture radar," IEEE Trans. Geosci. Remote Sensing, vol.37, pp.461–466, 1999, doi: 10.1109/36.739088.

[39] https://www.ndbc.noaa.gov/

[40] http://www.apl.washington.edu/project/project.php?id=darla

[41] S. Aslebagh and G. Farquharson, "Wave period and direction estimation in shallow water using airborne along-track interferometric synthetic aperture radar," 2015 IEEE International Geoscience and Remote Sensing Symposium (IGARSS), Milan, 2015, pp. 3626-3629.

VITA

Shadi Aslebagh received her B.S. degree form Khaje-Nasir University of Technology, Tehran, Iran in 2005 and M.S. degree from University of Central Florida, Orlando, USA in 2013, both in electrical engineering. She completed her PhD at the department of electrical and computer engineering at University of Washington, Seattle, USA in 2018. Her research interests are in the field of active and passive airborne and spaceborne microwave remote sensing. It includes geophysical retrieval algorithm of ocean surface current measurement using along-track interferometry synthetic aperture radar data and remote sensing based measurement of ocean waves.